Propagation Dynamics and High Harmonic Generation Using High Contrast Ultrashort Laser Pulses

Inaugural-Dissertation

zur Erlangung des Doktorgrades
der Mathematisch-Naturwissenschaftlichen Fakultät der
Heinrich-Heine-Universität Düsseldorf

vorgelegt von:

Anna Lena Giesecke geb. Lindemann

aus Hannover

Düsseldorf, Januar 2013

Aus dem Institut für Laser- und Plasmaphysik
der Heinrich-Heine-Universität Düsseldorf

Gedruckt mit der Genehmigung der
Mathematisch-Naturwissenschaftlichen Fakultät der
Heinrich-Heine-Universität Düsseldorf

Referent: Prof. Dr. Oswald Willi
Korreferent: Prof. Dr. Alexander Pukhov

Tag der mündlichen Prüfung: 19. April 2013

Abstract

The investigation of laser plasma processes utilising high contrast laser pulses is of great interest for many applications including the search for novel X-ray sources that are ideally suited to study inner-atomic structural dynamics. In this thesis, the interaction of ultrashort laser pulses with both, solid and gaseous targets using high contrast laser systems is investigated in two different intensity regimes. Firstly, gaseous targets were irradiated by a 10 fs laser pulse focused to an intensity of 6×10^{16} W/cm^2 to study the nonlinear interaction during the laser pulse propagation. Secondly, solid targets with periodically modulated surfaces were used to generate high harmonic radiation apart from the specular direction of the laser by using the 27 fs laser pulse of the ARCTURUS laser at a focal spot intensity of 2×10^{20} W/cm^2. In order to provide a high temporal laser contrast, a plasma mirror system was built and implemented into the ARCTURUS laser system in the course of these experiments. The characterisation of this device shows a temporal contrast of 10^{-11} and a high energy throughput (80 %).

The first experiment gives insights into the influence of the gas pressure on the spectral phase of the laser pulse. Studying the laser pulse propagation through different noble gases (helium, neon and argon) is relevant for the generation of high harmonics from gaseous targets which can be used as a source for applications applying ultrahigh time resolution. The high temporal contrast of the FEMTOPOWER compact PRO laser system allows to analyse the interaction processes without strong preplasma effects. This is especially important for investigating the impact of the ionisation process through optical field ionisation. It was found that rising the gas pressure leads to a change of the second-order dispersion coefficient from negative to positive values for helium gas. The interplay of ionisation and Kerr-effect is discussed by means of numerical simulations.

The second experiment demonstrates the first evidence of high harmonic emission from periodically modulated targets. The intense pulse of the ARCTURUS laser was focused onto the grating targets close to normal incidence (5°). Harmonic radiation was detected along the target surface, largely separated from the specular direction of the laser, which enables various applications to benefit from this new generation method due to the possibility to omit strong filters. The generation process was studied over a broad wavelength range (from second order up to 45$^{\text{th}}$ order). Moreover, the influences of different parameters on the high harmonic emission such as grating periodicity, preplasma, incidence angle etc. were investigated by means of 2D PIC simulations. Based on the results of experiment and simulations, a very good understanding of the interplay of the different parameters that influence the generation of high harmonics from grating targets was obtained. The results show that the spectral properties of the grating harmonics can be controlled by changing the grating parameters.

Zusammenfassung

Die Untersuchung der Laser-Plasma-Wechselwirkung mithilfe von Laserpulsen mit hohem Kontrast ist von großem Interesse für viele Anwendungen wie beispielsweise die Suche nach neuartigen Röntgenstrahlungsquellen, die sich bestens für die Erforschung von inneratomaren Strukturveränderungen eignen. In dieser Arbeit wurde mithilfe von Lasersystemen mit hohem zeitlichen Kontrast die Wechselwirkung von ultrakurzen Laserpulsen mit sowohl Festkörpern als auch gasförmigen Targetmaterialien in zwei verschiedenen Intensitätsregimen untersucht. Zunächst wurde eine Untersuchung der nichtlinearen Wechselwirkungen während der Laserpulspropagation eines 10 fs-Laserpulses bei einer fokussierten Intensität von $6\times10^{16}\,\mathrm{W/cm^2}$ in gasförmigen Targets durchgeführt. Darüber hinaus wurden Festkörpertargets mit periodisch modulierten Oberflächen für die Erzeugung Hoher Harmonischer Strahlung genutzt, die unabhängig von der spekularen Richtung des Lasers gemessen wurde. Hierzu wurden die 27 fs-Laserpulse des ARCTURUS-Lasers mit einer Intensität von $2\times10^{20}\,\mathrm{W/cm^2}$ fokussiert. Um einen hohen zeitlichen Laserkontrast zu gewährleisten, wurde im Rahmen dieser Arbeit ein Plasmaspiegelsystem gebaut und in das ARCUTURUS-Lasersystem implementiert. Die Charakterisierung dieses Geräts ergab einen zeitlichen Kontrast von 10^{-11} und einen hohen Energiedurchsatz von 80 %.

Das erste Experiment ermöglicht Einblicke in den Einfluss des Gasdrucks auf die spektrale Phase des Laserpulses. Die Untersuchung der Laserpulspropagation durch verschiedene Edelgase (Helium, Neon und Argon) ist von Relevanz für die Erzeugung von Hoher Harmonischer Strahlung in gasförmigen Targets, die für Anwendungen mit ultrahoher Zeitauflösung genutzt werden kann. Der hohe zeitliche Kontrast des FEMTOPOWER compact PRO Lasersystems ermöglicht die Untersuchung des Wechselwirkungsprozesses ohne starke Vorplasma-Effekte. Dies ist für die Betrachtung der Einflüsse des Ionisationsprozesses durch optische Feldionisation von besonderer Bedeutung. Die Ergebnisse zeigen, dass die Erhöhung des Helium-Gasdrucks zu einer Änderung des Dispersionskoeffizienten zweiter Ordnung von negativen hin zu positiven Werten führt. Das Wechselspiel von Ionisation und Kerr-Effekt wird mithilfe von numerischen Simulationen diskutiert.

Das zweite Experiment demonstriert den ersten Beleg für die Abstrahlung von Hohen Harmonischen von Targets mit periodisch modulierten Oberflächen. Der intensive Laserpuls des ARCTURUS-Lasers wurde nahe des lotrechten Einfalls (5°) auf die Gittertargets fokussiert. Harmonische Strahlung konnte entlang der Oberfläche des Targets detektiert werden. Damit befindet sich die Strahlung weit entfernt von der spekularen Richtung des Lasers, was aufgrund der Möglichkeit, auf starke Filter zu verzichten, verschiedensten Anwendungen erlaubt, von dieser neuen Erzeugungsmethode zu profitieren. Der Erzeugungsprozess wurde über einen breiten Wellenlängenbereich untersucht (zweite Ordnung bis zur 45. Ordnung). Des Weiteren fand eine Analyse der Einflüsse verschiedener Parameter wie

beispielsweise Gitterperiodizität, Vorplasma, Einfallswinkel etc. auf den Erzeugungsprozess der Hohen Harmonischen Strahlung mithilfe von 2D PIC-Simulationen statt. Auf Basis der Resultate von Experiment und Simulation, konnte ein sehr gutes Verständnis des Zusammenspiels der verschiedenen Parameter, welche die Harmonischen-Erzeugung von Gittertargets beeinflussen, gewonnen werden. Die Ergebnisse zeigen, dass die spektralen Eigenschaften der Hohen Harmonischen durch die Änderung der Gitterparameter kontrolliert werden können.

Contents

1 Introduction

The recently developed ultrashort high power laser systems allow the investigation of intense few-cycle laser pulses interacting with different types of targets (gaseous, solid). Hereby, the interaction of high-intensity laser pulses with matter provides the possibility of new radiation sources that enable interesting wavelength ranges, pulse durations etc. The study of the dynamics of chemical reactions is feasible by means of ultrafast spectroscopy using short pulse lasers with pulse durations of a few femtoseconds. In order to investigate the inner-atomic electron dynamics, even shorter light pulses are needed [1, 2]. These time scales of several attoseconds ($1\,\mathrm{as} = 10^{-18}\mathrm{s}$) can be obtained by frequency up-conversion of high-intensity laser pulses to the XUV range. Pioneering experiments achieving X-ray pulses from gaseous targets which allow pump-probe experiments with attosecond time resolution, were published post-millennial in 2001 [3, 4, 5].

The understanding of the propagation dynamics of ultrashort laser pulses interacting with gaseous targets is important to describe the changes of the laser pulse during the high harmonic generation process. Since the generation process of high harmonics from gaseous targets is strongly linked to the ionisation process, with thresholds around intensities of 10^{14}–$10^{16}\,\mathrm{W/cm^2}$ for the commonly used noble gases, the photon flux is limited and an increase of the laser intensity does not necessarily result in a higher intensity of the generated X-rays.

Many applications, e. g. X-ray imaging [6, 7], need coherent short pulse radiation, which can be produced by frequency up-conversion of intense laser pulses. The high harmonic generation from solid surfaces offers an opportunity to enter the XUV wavelength regime with high photon flux which was previously only accessible from large facilities like synchrotrons or free-electron lasers. As a different approach to obtain coherent radiation in the XUV range, Bulanov et al. [8] described the generation of high harmonics from relativistically oscillating solid surfaces theoretically in 1994. The first experimental findings of this harmonic radiation were reported in 1996 by Norrey et al. [9] at the Rutherford Appleton Laboratory in the United Kingdom. Solid targets were irradiated by the intense VULCAN laser (pulse duration 2.5 ps) at an intensity of $10^{19}\,\mathrm{W/cm^2}$. Recently, experimental and numerical results indicated that the temporal contrast of the laser pulse plays a crucial

role in the generation process of high harmonics from solid surfaces [10].

The properties of the emitted harmonic radiation from flat targets were studied in detail by means of particle-in-cell (PIC) simulations [11]. Optimum plasma scale length and laser incidence angle for the generation of high harmonics were identified. Nevertheless, the isolation of single attosecond pulses is still a challenging task. Several rather complex techniques were proposed during the last few years [12, 13, 14]. Regardless of the generation mechanism, high harmonic radiation was only emitted in the specular direction of the driving laser so far, hence lower orders of the harmonics needed to be suppressed by filters. Recent theoretical works indicated that grating targets can be employed in order to selectively enhance certain high harmonic orders [15, 16]. In this thesis, a new method of harmonic generation apart from the specular direction of the laser using grating targets is experimentally demonstrated. 2D PIC simulations support the experimental findings and reveal that the spectral distribution can be controlled by the grating parameters.

The temporal contrast of a high contrast laser system is one of the key elements for the feasibility of experiments with thin or structured target materials. Recent improvements of the target fabrication techniques allow to manufacture foils with a thickness of only several atomic layers [17, 18]. Negative consequences of the strong amplification process in high power laser systems are amplified spontaneous emission and prepulses with a significant amount of energy. These issues can lead to an early ionisation or even destruction of the target prior to the arrival of the high intensity main pulse. Hence, the interaction of the main pulse with target takes place when it is already covered by an expanding preplasma, and steep density gradients at the vacuum/target interface cannot be accomplished. Applications like the Thomson scattering [19] and especially the relativistically flying mirror [20, 21] are only possible after the enhancement of the temporal laser contrast by the means of different techniques as for example plasma mirrors. In particular, experiments with targets of a few nanometer thickness, i. e. the **R**adiation **P**ressure **A**cceleration (RPA) of protons, require the highest possible temporal contrast additionally to the high intensity of the laser pulse [22, 23, 24]. A plasma mirror system uses the fact that overdense plasma acts as an efficient reflector. The laser pulse is focused onto a glass target so that prepulses and the pedestal are still transmitted. However, the steep rising edge of the main pulse ignites an overdense plasma from which only the main pulse is reflected. Since the glass target is damaged after each laser shot, a quick translation and replacement has to be guaranteed in order to limit the required effort for conducting high contrast experiments with a high repetition rate. The usage of a plasma mirror system in high power laser systems delivering ultrashort laser pulses allows the investigation of possible new sources of XUV radiation.

Overview of the content of this thesis:

This work contains the study of ultrashort laser pulses with matter in two different intensity regimes: The ionisation processes at intensities of $10^{16}\,\mathrm{W/cm^2}$ and the generation of high harmonic radiation in the relativistic regime ($I \sim 10^{20}\,\mathrm{W/cm^2}$). In the experiments, the interaction between high contrast laser pulses and underdense (gaseous) as well as overdense (solid) targets was investigated. The results are supported by numerical simulations.

The thesis is structured as follows: Chapter 2 introduces the important physical processes which are necessary to describe the experiments and the simulations in the subsequent chapters. For this purpose, a brief introduction into laser-plasma physics is given, and the absorption processes as well as the propagation of laser light in underdense plasmas are presented. The chapter concludes with the principle of the generation of radiation with frequencies which are multiples of the laser frequency (high harmonics), from solid targets with periodically modulated surfaces.

An overview of the laser systems that were used to perform the experiments is given in chapter 3. Furthermore, important pulse characteristics of high power laser systems are presented. The contrast enhancement employing a plasma mirror system is introduced as well. Afterwards, the characterisation of the plasma mirror, which was built and implemented into the ARCTURUS laser system, is illustrated together with the corresponding contrast measurements.

Chapter 4 is dedicated to the experimental setups, employed techniques and diagnostic methods such as SPIDER and spectrometers.

The succeeding chapter 5 deals with the measurements of the spectral phase of the laser pulse using the SPIDER technique in the moderate intensity regime ($\sim 10^{16}\,\mathrm{W/cm^2}$). This study is important for the understanding of nonlinear propagation dynamics of laser pulses in underdense targets and thereby the generation of high harmonic radiation by using gaseous targets. Different computational simulations provide a deeper insight into the physical processes and parameter dependencies.

Chapter 6 includes the experiments with structured targets and the emission of high harmonic radiation from grating targets in two different wavelength ranges. The experimental findings are supported and extended by 2D PIC simulations.

The last chapter summarises the results and gives an outlook for future experiments and analyses.

2 Basics of short-pulse laser interaction with plasmas

Many processes are involved in the interaction of high intensity laser pulses with matter. The important mechanisms, which are relevant for the topics discussed further on, are summarised in this chapter. The ionisation of solid and gaseous targets can be triggered by different processes described in the next section. Afterwards, the coupling of the laser to the target material is presented and the relevant absorption processes are addressed. The laser pulse itself changes its properties during the propagation through different media. Self-focusing and pulse compression can appear just to mention a few of the possible processes. Later on, the interaction of laser pulses with solid targets is discussed, which can lead to the generation of radiation with frequencies that are multiples of the laser frequency (high harmonics).

2.1 Ionisation processes

Noble gases can be ionised by laser light due to photo ionisation, if the energy of the photon is sufficient to overcome the binding potential of the electron. For laser intensities of 10^{12}–10^{13} W/cm^2, two additional ionisation mechanisms can occur. Atoms can still become

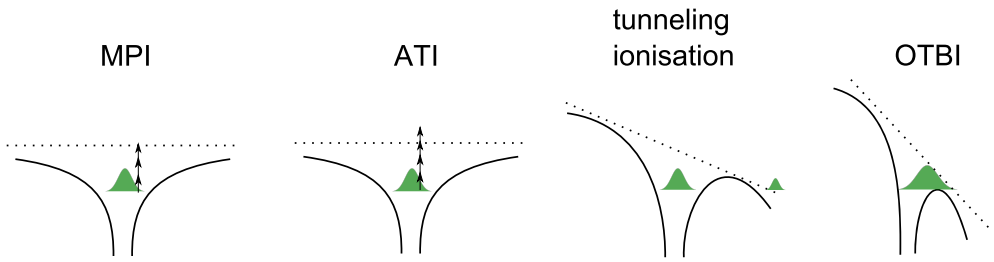

Figure 2.1: Schematic picture of four different ionisation mechanisms; the electron is shown in green as the probability of presence. The dotted line depicts the ionisation barrier. The black curve represents the binding potential of the atom.

ionised, when the energy $\hbar\omega$ of one single photon is not sufficient to overcome the atom's binding potential. If the laser field contains enough photons, one atom can absorb several photons at the same time until the ionisation threshold is reached. This process is called **M**ulti**p**hoton **I**onisation (**MPI**)(see figure 2.1). It was already theoretically predicted as two-photon absorption in 1931 [25] and confirmed experimentally in the sixties [26, 27]. If the energy of these photons is higher than the ionisation threshold, the mechanism is named **A**bove-**T**hreshold **I**onisation (**ATI**) [28].

The ionisation probability is given by the integrated ionisation rate R_I of the n^{th}-ionisation stage:

$$P_{\text{ion}} = \int dt\, R_I(t) \approx \sigma_n \tau \Phi^n \tag{2.1}$$

where τ is the duration of the laser pulse, Φ^n the photon flux and σ_n the cross section of the interaction.

Higher laser light intensities (10^{14}–10^{15} W/cm^2) deform the electric binding potential $V(x)$ of the atom severely, with the result that the electrons have a significant probability to tunnel and leave the atom's potential. Using the Keldysh parameter [29], it is possible to distinguish which of these processes dominates [30]:

$$\gamma_{\text{K}} = \omega_L \sqrt{\frac{2E_{\text{ion}}}{I_{\text{L}}}} \sim \sqrt{\frac{E_{\text{ion}}}{\Phi_{\text{pond}}}} \tag{2.2}$$

where $\Phi_{\text{pond}} = \frac{e^2 E_L^2}{4m\omega_L^2}$ is the ponderomotive potential and E_{ion} the ionisation potential.

If $\gamma_{\text{K}} > 1$, multiphoton ionisation is the dominating process and if $\gamma_{\text{K}} < 1$, it is tunneling ionisation, respectively.

For even higher intensities, the electric potential of the atom is strongly deformed, because the electric field of the laser becomes comparable to the atomic potential. Thus, the electron is not bound to the atom anymore. This process is called **B**arrier **S**uppression **I**onisation (**BSI**) [31, 32] or **O**ver-**T**he-**B**arrier **I**onisation (**OTBI**). The Coulomb potential of the atom is modified by the electric field of the laser [33]:

$$V(x) = -\frac{Ze^2}{x} - eE_{\text{laser}}x \tag{2.3}$$

The critical field strength is accomplished when:

$$E_{\text{laser}} \geq E_{\text{crit}} = \frac{E_{\text{ion}}^2}{4Ze^3} \tag{2.4}$$

For ions with the charge Z, the corresponding appearance intensity I_{app} can be expressed by:

$$I_{\mathrm{app}} = \frac{c}{8\pi}E_{\mathrm{crit}}^2 = \frac{cE_{\mathrm{ion}}^4}{128\pi Z^2 e^6} \sim 4\times 10^9 \left(\frac{E_{\mathrm{ion}}}{eV}\right)^4 Z^{-2}\,\mathrm{W/cm^2}. \tag{2.5}$$

According to this formula, the appearance intensity for the simplest atom, the hydrogen atom with $E_{\mathrm{ion}} = 13.6\,\mathrm{eV}$, is $I_{\mathrm{app}} \sim 1.4\times 10^{14}\,\mathrm{W/cm^2}$.

At even higher intensities ($>10^{15}\,\mathrm{W/cm^2}$) the ionisation rates can be deduced from the **A**mmosov-**D**elone-**K**rainov-theory (**ADK**) [34]. In this model, effects are averaged over one oscillation period and it is only valid for strong laser fields, as multiphoton ionisation is omitted. Measurements with different noble gases and laser intensities conducted by Augst et al. confirmed the theory [35]. According to ADK theory, the ionisation rate can be obtained from [36]:

$$W_{\mathrm{ADK}} = |C_{n^*l^*}|^2 f_{lm} E_{\mathrm{ion}} \sqrt{\frac{6}{\pi}} \left(\frac{2(2E_{\mathrm{ion}})^{3/2}}{E}\right)^{2n^*-|m|-3/2} \exp\left(-\frac{2(2E_{\mathrm{ion}})^{3/2}}{3E}\right) \tag{2.6}$$

where n^* is the effective principal quantum number, l the angular momentum, m the magnetic quantum number; the factors f_{lm} and $|C_{n^*l^*}|^2$ can be found in [37]. The light-induced tunneling of electrons was also observed experimentally [38]. Since the ADK theory does not incorporate multiphoton ionisation, it underestimates the ionisation rate in the intermediate regime. Another model for tunneling ionisation, which was suggested by Perelomov et al., is called the PPT model [39]. In contrast to the ADK theory, this model is also valid for laser intensities below $10^{15}\,\mathrm{W/cm^2}$. The corresponding ionisation rates (including Coulomb correction) are [36]:

$$\begin{aligned} W_{\mathrm{PPT}} = |C_{n^*l^*}|^2 f_{lm} E_{\mathrm{ion}} \sqrt{\frac{6}{\pi}} \left(\frac{2(2E_{\mathrm{ion}})^{3/2}}{E}\right)^{2n^*-|m|-3/2} & (1+\gamma_K^2)^{|m|/2+3/4} \\ & \times A_m(\omega,\gamma_K) \exp\left(-\frac{2(2E_{\mathrm{ion}})^{3/2}}{3E} g(\gamma_K)\right) \end{aligned} \tag{2.7}$$

where

$$g(\gamma_K) = \frac{3}{2\gamma_K}\left[\left(1+\frac{1}{2\gamma_K^2}\right)\sinh^{-1}(\gamma_K) - \frac{\sqrt{1+\gamma_K^2}}{2\gamma_K}\right]. \tag{2.8}$$

The calculation of the coefficient A_m is done in [37]. The PPT model predicts experimental

ionisation rates accurately over a broad intensity regime ($\approx 10^{13}$-10^{15} W/cm^2).

After the target is preheated, ionisation due to the contribution of collisions with free electrons, the so called **E**lectron (impact) **I**onisation (**EI**), becomes more considerable, especially for high density targets. An energetic electron hits and ionises the atom by ejecting bound a electron according to:

$$A + e^- = A^+ + 2e^- \tag{2.9}$$

Currently, in computational simulations, the ADK theory and the PPT model are both used, depending on the input energy of the laser pulse [40, 41].

2.2 Properties of plasmas

A plasma is a mixture of neutral and charged particles. It is described as a many-particle-ensemble, where collective effects dominate the behaviour of the whole system.

The propagation of laser light in a plasma is described by the dispersion relation:

$$\omega^2 = \omega_\mathrm{p}^2 + k^2 c^2 \tag{2.10}$$

where ω is the frequency of the laser, k the wave number. ω_p is known as the plasma frequency:

$$\omega_\mathrm{p} = \sqrt{\frac{e_0^2 n_\mathrm{e}}{\varepsilon_0 m}} \tag{2.11}$$

where n_e is the electron density and $m = \gamma m_\mathrm{e}$ the electron mass. From 2.10, the refractive index can be obtained:

$$n = \sqrt{1 - \frac{\omega_\mathrm{p}^2}{\omega^2}} = \sqrt{1 - \frac{n_\mathrm{e}}{n_\mathrm{crit}}} \tag{2.12}$$

with the critical density $n_\mathrm{crit} = \frac{\varepsilon_0 m \omega^2}{e_0^2}$. The propagation of light through the plasma is only possible if $\omega > \omega_\mathrm{p}$. Otherwise, the plasma is called overdense (see figure 2.2). The reflectivity of a plasma can reach up to 100 % for $\omega = \omega_0$ which can be deduced from the Fresnel equations.

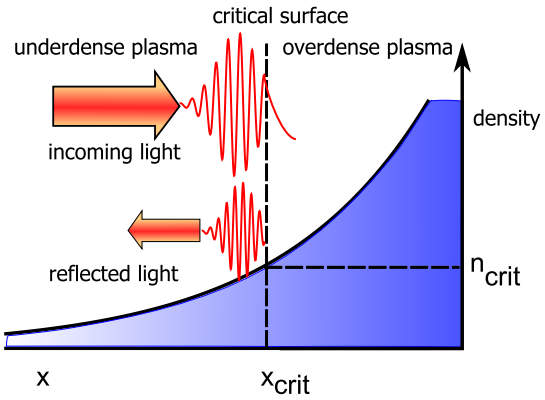

Figure 2.2: The density profile of the spatial expansion of the preformed plasma. The incoming laser light is reflected at the critical density.

If a plasma expands freely, the velocity can be approximated by the ion sound velocity:

$$c_{\mathrm{is}} = \sqrt{\frac{Z^* k_B T_e}{m_i}} \tag{2.13}$$

where k_B is the Boltzmann constant, Z^* the ionisation degree, T_e the electron temperature and m_i the ion mass. The electron density can be approximated by the exponential decay:

$$n_e(z) = n_{\mathrm{ev}} \exp(-z/L) \tag{2.14}$$

where n_{ev} denotes the valence electron density and $L = |\frac{\nabla n_e(z)}{n_{\mathrm{ev}}}|^{-1}$ defines the plasma scale length.

Another important plasma parameter is the Debye length:

$$\lambda_D = \sqrt{\frac{\varepsilon_0 k_{\mathrm{B}} T}{n_0 e^2}} \tag{2.15}$$

This is the distance after which a test particle (i.e. ion) can be regarded as screened from the electric fields of the plasma. The potential of the net charge is reduced by $1/e$ at this length. Outside the Debye sphere of the volume given by λ_D^3, charge separations inside the plasma have no influence on the test particle and the plasma is called quasineutral.

The electric field strength of a laser beam is described as a Gaussian function in transversal direction. Due to this gradient of the electric field, the laser light pushes electrons out of

regions of high intensities. This behaviour is quantified by the term of the ponderomotive force F_p:

$$F_p = -\frac{e^2}{4m_e\omega_L^2 c}\nabla\langle\vec{E}^2\rangle \tag{2.16}$$

where $\langle\vec{E}^2\rangle$ denotes the time average of the electric field.

The refractive index is increased by the decreasing electron density in regions with high intensity. In this zone, due to strong electron oscillations and the correlated relativistic electron mass growth, additional self-focusing occurs. This results in a decreasing plasma frequency and thus an increased refractive index. A detailed explanation of these processes will be given in section 2.4.

By applying lasers with hundreds of terawatts peak intensity like the ARCTURUS laser system in Düsseldorf, the electron dynamics becomes nonlinear and relativistic effects must be taken into account. In order to describe the strength of a laser, the dimensionless laser amplitude a_0 can be expressed by:

$$a_0 = \frac{v_\perp}{c} = \frac{eE_0}{m_e\omega c} \tag{2.17}$$

where $v_\perp$ is the speed of an electron transverse to the k-vector of the laser light. The dimensionless term for a_0 can be understood as a normalised vector potential.

The value of the intensity wavelength product (also called laser irradiance) where relativistic effects need to be considered, is:

$$I\lambda^2 \geq 10^{18}\,\mathrm{W/cm^2\mu m^2} \tag{2.18}$$

This corresponds to a normalised vector potential of $a_0 \geq 1$.

2.3 Heating processes and absorption

A variety of different processes, dependent on the density profile of the target material, the intensity and the angle of incidence of the laser, affect the absorption of laser light in plasmas. Depending on the laser intensity, the absorption processes can be dominated by collisions or by the collective behaviour of the electron population (collisionless). For moderate intensities (up to $\sim 10^{16}\,\mathrm{W/cm^2}$), the absorption is dominated by collisions: Relevant processes are for example inverse bremsstrahlung, the skin effect [42] and the

collective resonance absorption. At relativistic intensities ($\sim 10^{18}\,\mathrm{W/cm^2}$), the collisions lose their influence, and anomal absorption [43] and vacuum heating (also called Brunel absorption)[44] occur.

2.3.1 Collisional absorption

The equation of motion for one electron in the non-relativistic case including collisional damping is the Lorentz equation [33]:

$$m\frac{\partial \vec{v}}{\partial t} = -e\left(\vec{E} + \frac{\vec{v}}{c} \times \vec{B}\right) m\nu_{ei}\vec{v} \tag{2.19}$$

ν_{ei} is the electron-ion collision frequency [45]:

$$\nu_{ei} = \frac{4\sqrt{2\pi}}{3}\frac{n_e Z e^4}{m^2 v_{te}^3}\ln\Lambda \sim 2.91 \times 10^{-6} Z n_e T_e^{-3/2}\ln\Lambda\,\mathrm{s}^{-1} \tag{2.20}$$

where Z is the ionisation state, T_e the electron temperature, v_{te} the thermal electron velocity and $\ln\Lambda$ the Coulomb logarithm which is connected to the Debye length of the plasma $\Lambda = \lambda_D \frac{k_B T_e}{Ze^2}$.

Inverse bremsstrahlung

If a charged particle collides with another particle, it emits bremsstrahlung. The process in which an electron absorbs a photon while colliding with an ion is called **inverse bremsstrahlung** [46]. This mechanism dominates for longer pulses ($\sim$ ps) and intensities $< 10^{13}\,\mathrm{W/cm^2}$ at shorter wavelengths (260 nm) [47]. Inverse bremsstrahlung strongly depends on the electron-ion collision probability, the shape of the density profile and also on the electrical conductivity [48, 49, 50].

Skin effect

In case of a step-like density profile, the electric field of the laser decays exponentially:

$$E(z) = E(0)\exp(-z/l_\mathrm{s}) \tag{2.21}$$

where $l_\mathrm{s} \sim \frac{c}{\omega_\mathrm{p}}$ is the collisionless skin depth [33]. The field is evanescent in the overdense region of the plasma. The reflectivity of the target can be expressed by the Fresnel

equations:

$$R_s = \left| \frac{\sin(\theta - \theta_t)}{\sin(\theta + \theta_t)} \right|^2 \qquad \text{for s-polarised light} \tag{2.22}$$

$$R_p = \left| \frac{\tan(\theta - \theta_t)}{\tan(\theta + \theta_t)} \right|^2 \qquad \text{for p-polarised light} \tag{2.23}$$

where θ is the angle of incidence and $\theta_t = \sin^{-1}\left(\frac{\sin\theta}{n}\right)$ is the angle of the transmitted rays which can be deduced from Snell's law [51].

The absorption coefficient η for the **normal skin effect** is [33]:

$$\eta = 1 - R = \begin{cases} \frac{2\nu_{ei}}{\omega_p}, & \nu_{ei} \ll \omega_0 \\ \frac{2\omega_0}{\omega_p}\sqrt{\nu_{ei}/\omega_0}, & \nu_{ei} > \omega_0 \end{cases} \tag{2.24}$$

The normal skin effect occurs mainly for intensities below $10^{15}\,\mathrm{W/cm^2}$ [52], whereas the **anomalous skin effect** becomes important for the regime $\omega^2 c^2 \ll \omega_p^2 v_e^2$ and laser intensities $> 10^{16}\,\mathrm{W/cm^2}$ [43].

2.3.2 Collisionless absorption

Resonance absorption

The concept of **resonance absorption** was already intensively studied in the seventies of the last century [53, 54]. If a polarised wave hits a plasma which has an increasing density gradient in z-direction, the electrons near the critical density start to oscillate, caused by the electric field component in the direction of the density gradient [45]. The dispersion relation for the electromagnetic wave propagating in the x-y plane is:

$$\omega_L^2 = \omega_p^2 + (k_y^2 + k_z^2)c^2 \tag{2.25}$$

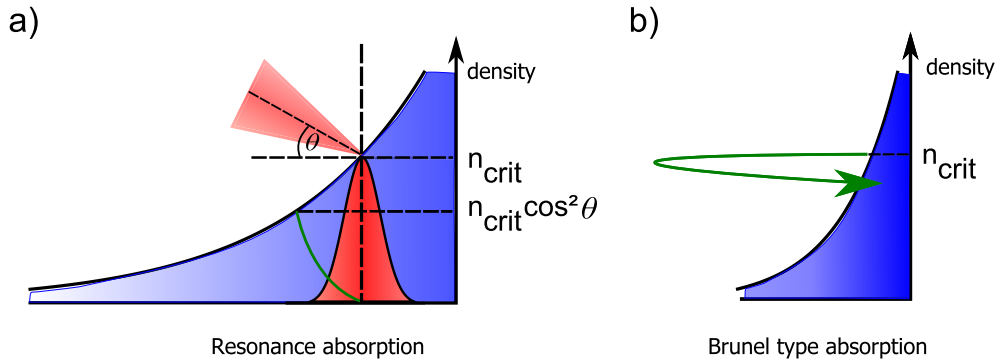

Figure 2.3: The two dominating absorption processes for oblique incidence and p-polarized laser light: The resonance absorption takes place mainly for long scale lengths when the electromagnetic field of the laser can drive plasma oscillations resonantly. At steeper density gradients, the electron oscillation amplitude exceeds the plasma boundary (Brunel type absorption). The movement of the electrons is shown in green.

For a given angle of incidence, $k_y = \frac{\omega_L}{c}\sin(\theta)$ is constant. Consequently, it is reflected at the density [45]:

$$n_{\text{eff}} = n_{\text{crit}}\cos^2(\theta) \tag{2.26}$$

Partially, the electrical field can tunnel up to the critical density and trigger oscillations parallel to the density gradient. A plasma wave (also Langmuir wave) is generated.

Energy is transferred from the laser light to the plasma. The Langmuir wave loses its energy due to Landau damping. Plasma waves cannot be excited at normal incidence. The amplitude of the electron oscillation is [55]:

$$A_{\text{os}} \sim \frac{eE_0}{m_e\omega_0^2} = \frac{v_{\text{os}}}{\omega_0} \tag{2.27}$$

If the intensity of the laser is very high and the amplitude of the plasma wave exceeds the plasma scale length ($\frac{v_{\text{os}}}{\omega_0 L} > 1$), no energy transfer can take place [56].

Brunel absorption/Vacuum heating

The dominating process for p-polarised light and high laser contrast at oblique incidence is called **Brunel absorption**, where resonance absorption loses its influence for steep density gradients and high laser intensities. The mechanism was first described by Brunel [56]. For

small plasma scale lengths, the amplitude of the electron motion exceeds the scale length and the resonance breaks down.

During the first half-period of the light wave, the electrons are accelerated into the vacuum. After the electric field direction has changed, they are driven back into the plasma (see figure 2.3). If they reach the overcritical part of the plasma, they are not affected by the force of the laser light anymore, hence they propagate through the plasma and lose their energy by collisions [57].

For step-like density gradients, the contribution of Brunel type absorption is small because the laser does not penetrate into the overdense part of the plasma [58, 59]. Brunel type absorption is extremely important for the generation of high harmonic radiation from solid surfaces, which will be described in detail in chapter 6.

$\vec{j} \times \vec{B}$ heating

At relativistic laser intensities, another absorption process, the $\vec{j} \times \vec{B}$ **heating**, becomes more important. The driving force of this heating process is the high frequency component of the ponderomotive force of the laser light, which is proportional to the $\vec{j} \times \vec{B}$-term [60]. The energy of the light field can be directly transferred to the electrons. This absorption process works for s- and p-polarised but not for circularly polarised laser light. At normal incidence, it is most effective [61]. The electron density is steepened by the laser pushing electrons inwards. The short pulse interacts directly with the electrons and not with an expanding plasma. The steepening of the density profile impedes the light pulse to enter deeply into the plasma. Electrons which are pulled into the vacuum twice every laser cycle, are affected by the $\vec{v} \times \vec{B}$ force. Linearly polarised light evokes a longitudinal force [33]:

$$f_x = -\frac{m}{4}\frac{\partial v_{os}^2(x)}{\partial x}(1-\cos(2\omega t)) \tag{2.28}$$

where the first term is responsible for pushing the electron inwards and the oscillating term heats them parallel to the density gradient. They obtain kinetic energy $W_{\mathrm{os}} = (\gamma_{\mathrm{os}} - 1)mc^2$ where $\gamma_{\mathrm{os}} = \sqrt{1 + a_0^2/2}$.

2.4 Laser pulse propagation

Light propagation along the z-direction in a homogeneous medium can be described by:

$$E(z,t) = \int d\omega\, \hat{E}(\omega)\exp[i(\omega t k(\omega) z)] = \int d\omega\, \hat{E}(\omega)\exp[i(\omega t \phi(z,\omega))] \tag{2.29}$$

The phase ϕ and the wave number k can be expressed by the expansion of the Taylor series [62]:

$$\phi = \phi_0 + kz = \phi(\omega_0) + \left.\frac{\partial\phi}{\partial\omega}\right|_{\omega_0}(\omega-\omega_o) + \left.\sum_{j=2}^{\infty}\frac{(\omega-\omega_0)^j\partial^j\phi}{j!\partial\omega^j}\right|_{\omega_0} \tag{2.30}$$

$$= \phi_0 + \sum_{j=1}^{\infty} D_j\frac{(\omega-\omega_0)^j}{j!} \tag{2.31}$$

and

$$k(\omega) = k(\omega_0) + \left.\sum_{j=1}^{\infty}\frac{(\omega-\omega_0)^j}{j!}\frac{\partial^j k}{\partial\omega^j}\right|_{\omega_0} \tag{2.32}$$

where ϕ_0 is the absolute phase, which is the position of the carrier wave relative to the envelope of the electric field. From equation 2.31, the dispersion coefficients can be separated:

$$D_1 = \frac{\partial\phi}{\partial\omega} = \frac{\partial k}{\partial\omega}z \tag{2.33}$$

The D_1 coefficient denotes the group delay (**GD**, unit: s). The group delay dispersion (**GDD**), which is also often called group velocity dispersion (unit: s^2), determines the linear chirp of the laser pulse given by:

$$D_2 = \frac{\partial^2\phi}{\partial\omega^2} = z\frac{\lambda^3}{2\pi c^2}\frac{\partial^2 n}{\partial\lambda^2} \tag{2.34}$$

The third-order dispersion D_3 (**TOD**, unit: s^3) is therefore consequently:

$$D_3 = \frac{\partial^3\phi}{\partial\omega^3} = -z\frac{\lambda^4}{4\pi^2c^3}(3\frac{\partial^2 n}{\partial\lambda^2} + \lambda\frac{\partial^3 n}{\partial\lambda^3}). \tag{2.35}$$

2.4.1 Nonlinear polarisation

Nonlinear optical effects which accompany the laser pulse propagation through a medium, result from the interplay of the electric field and the induced polarisation in a medium. The polarisation is defined by the dipole moment per volume unit. In case of a weak electric field, the dependency of polarisation and electric field is linear. If the laser intensity is comparable with the atomic field, nonlinear effects become important. The polarisation can

be expressed by a power series expansion [63]:

$$\vec{P} = \varepsilon_0 \chi^{(1)} \vec{E} + P_{NL} = \varepsilon_0 [\chi^{(1)} \vec{E} + \chi^{(2)} \vec{E}^2 + \chi^{(3)} \vec{E}^3 + ...] \tag{2.36}$$

The polarisation response depends on the structure of the medium. The order of the susceptibility tensor χ plays the crucial role in determining which nonlinear processes can occur. $\chi^{(2)}$ processes are frequency doubling (second harmonic generation, SHG), sum and difference generation, parametric oscillation and the linear electro-optic effect (Pockels effect). Processes which result from the third-order susceptibility, are self-phase modulation, saturable absorption, third harmonic generation, Raman scattering and four-wave mixing. The symmetry of a nonlinear crystal defines how the susceptibility tensor looks. Even orders of the tensor vanish in a medium with inversion symmetry.

2.4.2 Self-phase modulation and self-focusing

The refraction index of a medium depends on the intensity of the laser [65] according to:

$$n(t,\omega) = n_0(\omega) + n_2(\omega) I(t) \tag{2.37}$$

where n_0 is the linear and n_2 the nonlinear (material-dependent) refraction index. The nonlinear part n_2 correlates with the third-order nonlinear susceptibility:

$$n_2 = \frac{3}{4} \frac{\chi^{(3)}}{\varepsilon_0 c n_0^2} \tag{2.38}$$

The n_2 values for three different noble gases can be found in table 2.1 [64].

There are two consequences of the time and intensity dependency of the refractive index, which are **self-phase modulation** and **self-focusing**.

Element	Z=1	Z=2
He	0.52	0.03
Ne	1.31	0.27
Ar	12.68	6.14

Table 2.1: Nonlinear refraction index n_2 for different noble gases (helium, neon and argon) at 800 nm (n_2 in $10^{-8}\mathrm{cm}^2/\mathrm{TW}$) according to [64].

The phase of the laser pulse with the time-dependent refractive index becomes:

$$\Phi(t) = \omega_0 t - kz = \omega_0 t - \frac{\omega_0[n_0 + n_2 I(t)]}{c} z \tag{2.39}$$

The phase shift increases with the propagation length z. Self-phase modulation does not change the envelope of the pulse in time but the distribution of the spectral component under the envelope. New spectral components can be generated at high intensities and over long propagation lengths. The instantaneous frequency ω can be expressed as:

$$\omega(t) = -\frac{\partial \Phi}{\partial t} = \omega_0 - \frac{\omega_0 n_2 z}{c} \frac{\partial I}{\partial t} \tag{2.40}$$

Thus, the frequency of the pulse front $\left(\frac{\partial I}{\partial t} > 0\right)$ is reduced, whereas the frequency of the trailing edge $\left(\frac{\partial I}{\partial t} < 0\right)$ is raised. The spectrum of the laser pulse is symmetrically broadened. Interference leads to an intensity modulation. The change of the instantaneous frequency during one pulse length is shown in figure 2.4.

There are three different kinds of self-focusing (SF) which can occur when a high intensity laser pulse is focused into a gaseous target: 1. self-focusing due to the intensity-dependent refractive index (**optical Kerr-effect**), 2. the ponderomotive SF and 3. the relativistic SF. The intensity-dependent refractive index causes self-focusing of the laser pulse for $n_2 > 0$. The central part of the pulse is influenced by a higher nonlinear refractive index, thus the phase velocity is reduced. Consequently, the wavefronts are curved and the pulse is

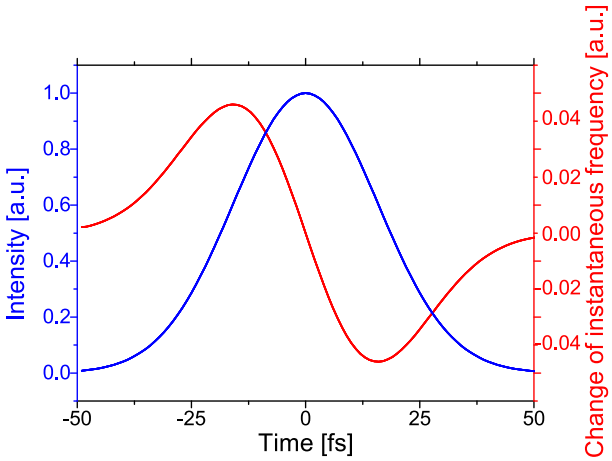

Figure 2.4: Change of instantaneous frequency (red). The intensity of the laser pulse is depicted in blue.

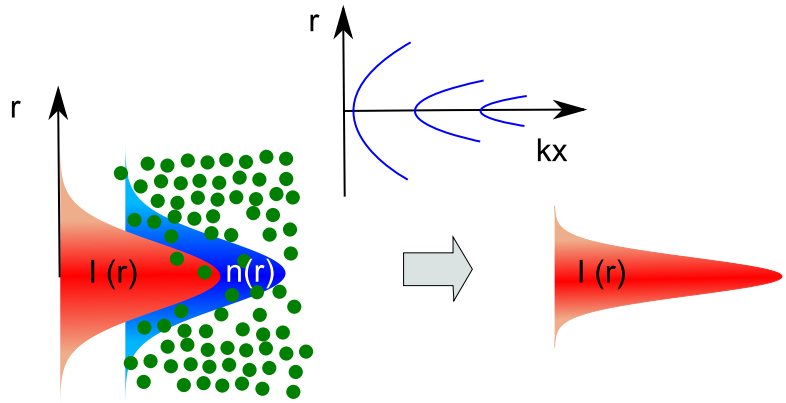

Figure 2.5: The ponderomotive force of the laser pulse changes the refractive index of the plasma. The phase velocity of the central part of the pulse is reduced, thus the wavefronts are curved and the plasma acts like a converging lens.

self-focused (see figure 2.5). The same situation occurs when a high intensity laser pulse propagates through a plasma, since electrons are pushed out of regions with higher intensity due to the ponderomotive force. Thus, the refractive index is higher for the central part of the pulse [66, 67, 68], as the refractive index of a plasma is (also see equation 2.12):

$$n_{\text{plasma}} = \sqrt{1 - \frac{n_e(r)}{n_{\text{crit}}}} \tag{2.41}$$

The characteristic self-focusing length L_{SF} can be denoted as:

$$L_{\text{SF}} = \frac{\lambda_0}{2\pi n_2 \hat{I}} \tag{2.42}$$

where $\hat{I}$ is the peak intensity of the pulse.

At relativistic intensities, n_{plasma} is changed due to the γ-factor of the oscillating electrons [69]:

$$n_{\text{plasma,relat}} = \sqrt{1 - \frac{n_e}{\gamma(r) n_{\text{crit}}}} \tag{2.43}$$

Since the γ-factor has its maximum on the propagation axis, it leads to a focusing effect as well.

2.4.3 Plasma defocusing

The counteracting process to self-focusing is the ionisation-induced defocusing [70, 71, 72, 73]: If the plasma is not completely ionised, the central part of the pulse on the propagation axis ionises more atoms and the electron density increases. This steep electron profile on the axis acts like a diverging lens (see figure 2.6). The starting ionisation impedes reaching the nominal vacuum focus inside the plasma [74]. The phase shift after propagating the length l is:

$$\Delta\phi = \frac{\pi l n_e}{\lambda n_{\text{crit}}} \tag{2.44}$$

If the phase shift becomes $\pi/2$, the beam divergence is doubled. According to this phase shift, a defocusing length can be defined as:

$$l_D = \frac{\lambda n_{\text{crit}}}{2 n_e} \tag{2.45}$$

The plasma-induced defocusing is dominant, if l_D is shorter than the Rayleigh length[1].

The interplay of the counteracting processes self-focusing and plasma defocusing lead to self-guiding of the laser pulse in a confined beam, which can be significantly longer than

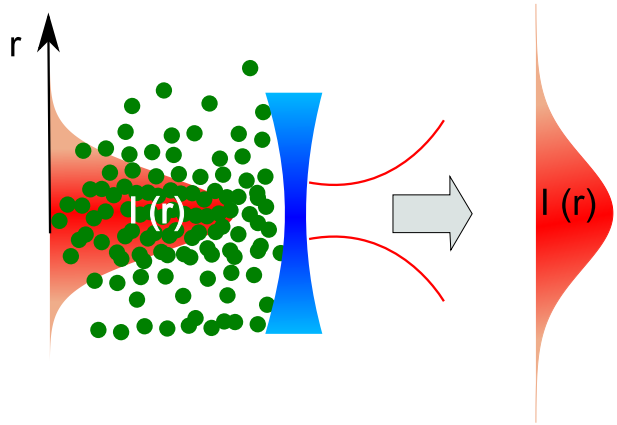

Figure 2.6: Defocusing effect in plasmas: The diffraction on the laser axis is stronger due to a higher ionisation rate. The plasma acts like a diverging lens.

1 Rayleigh length: $z_R = \frac{\pi w_0^2}{\lambda}$.

the Rayleigh length. This behaviour is known as filamentation [75]. The critical power for filamentation is:

$$P_{\text{crit}} = 3.72\frac{\lambda_0^2}{8\pi n_0 n_2} \tag{2.46}$$

2.4.4 Self-steepening

Also the group-velocity of a laser pulse changes due to the intensity dependence of the refractive index. This results in "self-steepening" of the pulse where the wings of lower intensities propagate faster than the pulse peak [76]. The temporal profile becomes asymmetric and higher frequency components are generated. The steepening occurs for the trailing part of the pulse.

2.4.5 Ionisation-induced blue-shift

Due to the rising electron density in gaseous media during the pulse propagation and ionisation, the refractive index of the plasma decreases. The resulting self-phase modulation causes a blue-shift in the spectral domain which is a spectral analogon of the spatial defocusing [77, 78, 79]. The wavelength shift of the incoming laser light with the initial wavelength λ_0 after the propagation length L through a homogeneous plasma, is given by [80]:

$$\Delta\lambda = \frac{\lambda_0 L}{c}\frac{dn}{dt} \tag{2.47}$$

Assuming an underdense plasma and neglecting the collisions, the shift becomes:

$$\Delta\lambda = -\frac{e^2 N_i \lambda_0^3 L}{8\pi^2 \varepsilon_0 m_e c^3}\frac{dZ}{dt} \tag{2.48}$$

where N_i is the ion density and Z is the degree of ionisation, which can be deduced from the ADK rates. The blue-shift becomes stronger for higher laser intensities [78]. For a constant gas pressure, the blue-shift is also stronger for gaseous media with higher atomic numbers such as neon or argon in comparison to helium as a consequence of the lower ionisation potentials of the lower ionisation stages [81] (also see Appendix A).

2.4.6 Pulse compression

In the standard method to shorten the pulse duration of a linearly chirped laser pulse, pairs of diffraction gratings, prisms or chirped mirrors with the exact amount of necessary dispersion are used to flatten the phase of the pulse. In [82], two consecutive argon-filled gas cells were used to broaden the spectrum by self-phase modulation and compressed the laser pulse by the reflection from chirped mirrors afterwards. However, also the interplay of self-focusing, self-phase modulation and negative group delay dispersion can lead to a pulse compression during the propagation through the plasma [83]. This effect can be observed in gas-filled fibres [84, 85] or filaments [82, 86, 87] as well. After the propagation through a medium with positive group velocity dispersion, a double structure was observed in the temporal domain [88].

Spectral broadening is induced by self-phase modulation. In order to shorten the laser pulse after the propagation through the underdense medium, the self-phase modulation must be counteracted by a negative group velocity dispersion of the medium (plasma). The self-guiding effect can act as a spatial filter. Limits of the pulse compression are caused by self-steepening, chromatic dispersion and the appearance of multifilaments [89]. Moreover, also ionisation-induced defocusing can attenuate the self-compression effect.

2.5 High-order harmonic generation

Many applications in chemistry, biology or physics, as for example the imaging of chemical reactions, lattice and molecular dynamics, require soft X-ray sources with high brilliance and femtosecond time resolution [90, 7, 6, 91]. The temporal resolution which can be obtained by using free electron lasers and synchrotrons, is limited by the X-ray pulse duration that typically lies in the range of picoseconds to several femtoseconds [92, 93]. The generation of high harmonics of the laser frequency is one opportunity to obtain radiation in the extreme ultaviolet (XUV) wavelength range with a time resolution of femtoseconds. Nevertheless, the isolation of attosecond pulses[2] is still a challenging task [12, 14, 13].

In contrast to gas harmonics, which are described by the semi-classical three-step models [94, 95], solid target harmonics are created on the overdense part of the plasma. Nonlinear oscillations are excited by intense laser light. These oscillations are in phase with the driving laser pulse, so that the emission is time-limited. Due to periodical repetitions and coherent

2 $1\,\mathrm{as} = 10^{-18}\,\mathrm{s}$.

superposition, radiation with frequencies of multiples of the laser fundamental frequency is generated. In order to create an efficient source of attosecond pulses, it is appreciated to have high photon fluxes and high pulse energy. This cannot be obtained by applying gaseous targets, because their intensity scaling depends on the ionisation of the target, which limits the pulse energy for the driving laser [96]. This drawback of the high harmonic generation in gases can be overcome by using overdense targets. Already in 2004, particle-in-cell simulations predicted zeptosecond[3] pulses at keV photon energies resulting from a reflection of a relativistically oscillating surface [97]. Therefore, high harmonic generation from solid surfaces using high intensity lasers with intensities $\sim 10^{20} - 10^{21}\,\mathrm{W/cm^2}$ is a step forward in the development of high flux attosecond pulses.

There are two different well-established mechanisms of generating high harmonic radiation from solid surfaces, which are described in the following sections. In both cases, the p-polarised laser beam is focused under an oblique angle onto a smooth surface [98, 99, 100]. **C**oherent **S**ynchrotron **E**mission (**CSE**) from electron nanobunches was recently shown to be a third way for the generation of high harmonic radiation from solid targets [101]. High-order harmonics generated by CSE can be obtained in transmission from thin 200 nm foils in the propagation direction of the laser.

2.5.1 Coherent wake emission

Coherent **W**ake **E**mission (**CWE**) harmonics are efficiently generated at intensities below the relativistic regime ($a_0 < 1$) [102]. They are driven by the movement of the electrons which travel across the overdense part of the plasma. The periodical process creates a train of attosecond pulses. For a p-polarised laser beam and the quiver velocity $v_{os}/c \geq 2\pi L/\lambda$, electrons can move into the underdense part of the plasma, driven by vacuum heating [45]. The frequency of the plasma wave, which depends on the local electron density, determines the wavelength of the harmonic. The cut-off frequency ω_{max} is set by the maximum plasma frequency, which again depends on the maximum electron density of the plasma:

$$\omega_{max} = \sqrt{\frac{n_{e,max} e^2}{m_e \varepsilon_0}} \tag{2.49}$$

Therefore, the frequency of the highest harmonic which can be possibly emitted, is restricted by the density of the solid target.

3 $1\,\mathrm{zs} = 10^{-21}\,\mathrm{s}$.

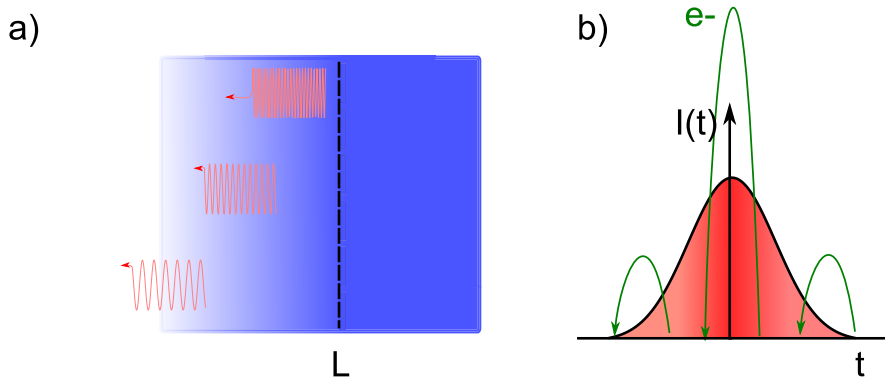

Figure 2.7: a) Higher frequencies are generated deeper inside the plasma. This causes an atto-chirp during the CWE harmonic generation.
b) The harmonic chirp results from the different amounts of time the Brunel electrons (green) travel until they re-enter the plasma, which depends on the instantaneous laser intensity.

The first part of the laser cycle drags the electrons out of the plasma/vacuum boundary. After the sign of the electric field has changed, they are accelerated back to the boundary. If these Brunel electrons reach the skin depth, they are not influenced by the laser field anymore and penetrate deeper into denser parts of the plasma by driving oscillations in their wake. These oscillations emit XUV radiation in case of an inhomogeneous density and p-polarised angle of incidence. Otherwise, only longitudinal oscillations are excited which cannot emit light [11]. CWE harmonics do not occur in plasmas with very steep density gradients [103].

Two different kinds of chirps occur during the generation of CWE harmonics: The **harmonic chirp** inside each harmonic is caused by the intensity fluctuation of the driving laser pulse during one pulse: The electrons therefore spend different amounts of time in the vacuum before they re-enter the plasma [102]. This effect leads to a spectral broadening of each harmonic in the spectrum. The second type of chirp, which is called **atto-chirp**, is a consequence of each harmonic being generated in a different depth at a different plasma gradient. The higher harmonics travel a longer path through the plasma, since their origin is a higher plasma density [104, 100](see figure 2.7). As a consequence of their chirp properties, CWE harmonics are no ideal source of attosecond pulses [10]. Further experimental results can be found in [100].

2.5.2 Relativistically oscillating mirror harmonics

Another generation mechanism of harmonics, which is called **R**elativistically **O**scillating **M**irror (**ROM**) model, has gained more importance with the increasing availability of laser pulses with relativistic intensities. The electromagnetic field of the laser causes a

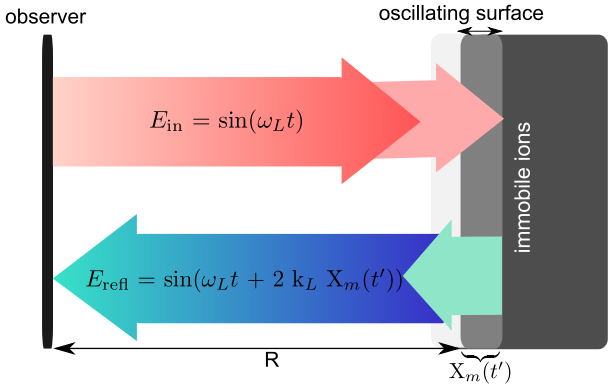

Figure 2.8: Simple model of the relativistically oscillating mirror. The electric field of the incoming laser is shown in red and the reflected part in blue. The plasma surface oscillates around X_m. See similar in [105].

movement of the plasma surface. This movement is periodically driven by the Lorentz force. As the electric term of the Lorentz force has more impact under oblique incidence and p-polarisation, the oscillation frequency of the electron density corresponds to the frequency of the laser. A description of these processes is also known as the "moving mirror" model [106]. In a simple form of the model (see figure 2.8), the harmonics are created by the Doppler up-shift resulting from the reflection from the relativistically oscillating plasma/vacuum interface [105]. The reflected light from the moving mirror $X_m(t')$ arrives at the observation point later:

$$t' = t + (R + X_m(t'))/c \tag{2.50}$$

where t' is the retarded time, t the observer time and R the distance between observer and mirror. To simplify the expressions, it is assumed in this case that the light is incident normal to the surface. Therefore, the incoming electric field is:

$$E_{\text{in}} = E_0 \sin(\omega_L t) \tag{2.51}$$

After the reflection, the field changes to:

$$E_{\text{refl}} = E_0 \sin(\omega_L t + 2k_L X(t')) \tag{2.52}$$

As an assumption, the motion of the surface can be described as:

$$X_m(t') = A_m(t) \sin(2\omega_L t' + \Phi) \tag{2.53}$$

in which Φ denotes the phase shift between the driving laser and the corresponding response of the surface. The amplitude A_m can be estimated from the maximum velocity of the mirror $v_{\max}/c = \beta_{\max} = 2A_m\omega_L/c$. By using the relativistic gamma factor $\gamma_{\max} = \left(\sqrt{1-\beta_{\max}^2}\right)^{-1}$, the amplitude can be denoted as:

$$A_m = \frac{\lambda_L}{4\pi\gamma_{\max}}\sqrt{\gamma_{\max}^2 - 1} \tag{2.54}$$

The simple model, which is only described by the Doppler effect of a moving plasma slab colliding with the laser pulse, does not explain harmonic generation for $> 4\gamma^2$. Nevertheless, harmonics exceeding the 1000$^{\text{th}}$ of the fundamental frequency were obtained in simulations [97] and experiments [107, 98]. Several nonlinearities, resulting from the fact that the surface does not oscillate as one unity, lead to a higher cut-off frequency [108], processes like nanobunching [109], and substructures inside the harmonic spectra [10].

ROM harmonics were first predicted by PIC simulations [8, 110]. They are only generated for laser pulses with $a_0 >> 1$. Scaling laws were described by Baeva et al. (in 1D) [108, 111]. The spectral envelope for these harmonics is $I(\omega) \propto I_0\omega^{-8/3}$, where the roll-off frequency is $\omega_r \sim \gamma_{\max}^3$. Recent experiments and simulations show a deeper understanding of the contributing processes [10, 109]. By varying the laser contrast with different substrates of the plasma mirror, a fine structure in the harmonic spectrum was observed. Up to now, harmonics up the $\sim 3000^{\text{th}}$ order of the fundamental laser frequency were detected in an experiment at the VULCAN PW laser system [107]. The phase properties of both CWE and ROM harmonics were studied by Quéré et al. [103]. The highest order harmonic is generated at the point where the oscillating surface has its maximum velocity. For ROM harmonics, the phase properties were studied theoretically in [112]. A chirp of individual ROM harmonics can occur from multi-cycle driving lasers. ROM harmonics have a low divergence of ∼20–25 mrad [99, 113].

Surface denting caused by the ponderomotive force of the laser pushing the electrons inwards, leads to different emission times [114]. The opportunity of generating attosecond pulses using the ROM mechanism has led to intensified research on this topic [115, 116]. Autocorrelation measurements of the XUV radiation can be found in [104].

The harmonic spectra obtained from a 2D particle-in-cell (PIC) simulation code are shown in figure 2.9. The target was placed under an angle of 45 ° in the simulation box. The intensity of the 27 fs long laser pulse was 10^{20} W/cm^2. The spectra were evaluated along the specular direction of the laser pulse. Figure 2.9 illustrates the harmonic spectra for two different plasma gradients which correspond to a high and medium temporal contrast of the laser pulse (see following chapter). The harmonics are better resolved in case of a steep

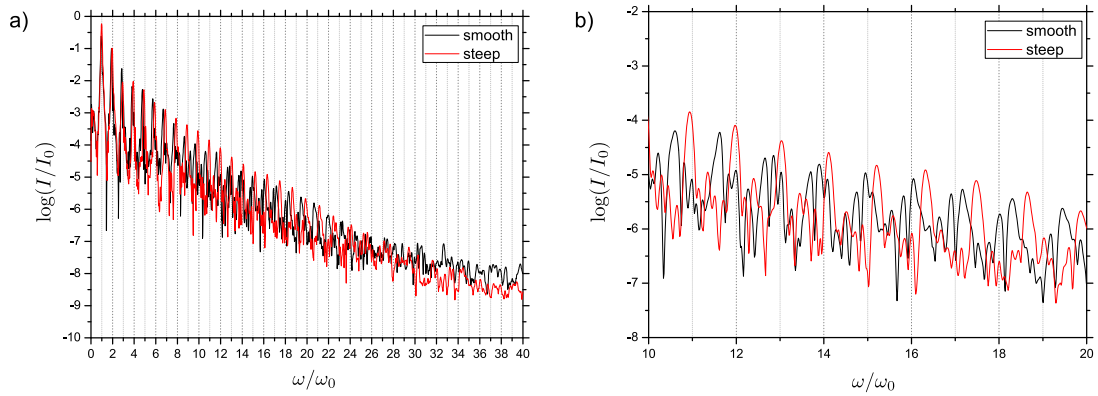

Figure 2.9: Results from 2D PIC simulation with EPOCH code: harmonics from flat targets in the specular direction. The laser with an intensity of $10^{20}\,\mathrm{W/cm^2}$ is incident 45 ° towards the target normal. The harmonic spectra for two different preplasma gradients (steep: $L \to 0$, smooth: $L \gg 0$) are shown.

gradient (red curve). An extended, exponentially decaying gradient (black curve) leads to a broadening of the harmonics. Similar results were previously obtained with the ARCTURUS laser system [10].

2.5.3 High-order harmonic generation from corrugated targets

Recently, a number of theoretical works indicated the possibility of controlling the spectral properties of the emitted radiation by using grating targets [15, 16, 117]. Moreover, grating targets are interesting for the generation of high-order harmonics, because the structure of their surfaces leads to a higher absorption [118, 119] and thus, to an increased coupling of the laser to the target [120]. For rectangular gratings fulfilling the condition $2/3 \leq a/\lambda_{\mathrm{Laser}} \leq 1$, a higher absorption due to the excitation of surface waves was observed in simulations [121]. Theoretical predictions of high harmonic generation (HHG) apart from the specular direction were made by Lavocat et al. in PIC simulations [15, 16]. In this case, the grating periodicities were multiples of the laser fundamental wavelength $a = \lambda_{\mathrm{Laser}}/k$ (k is an integer). Harmonics that fulfil an interference condition were found along the target surface generated with high efficiency. For the purpose of separating the harmonic signal from the specular direction of the laser, simulations for blazed grating targets were studied in simulations [117]. The results of Yeung et al. indicate a separation of the fifth harmonic. The key of this idea is to control the properties of the emitted radiation and to obtain the opportunity to omit strong filters in the setup.

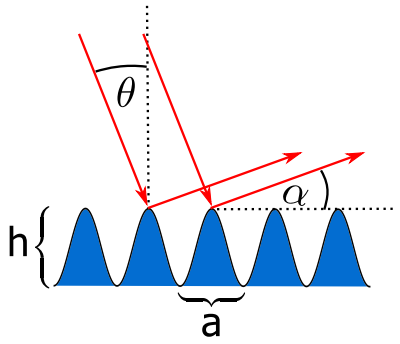

Figure 2.10: Sinusoidal grating structure illuminated with laser light under the angle θ. The observation angle of the radiation is α. The height of the protuberances is h and the grating period is a.

Analytical formula

Incoming laser beams can constructively interfere according to the formula for diffraction gratings:

$$a[\cos\alpha - \sin\theta] = n\lambda_{\text{reflected}}; \qquad \lambda_{\text{reflected}} = \frac{\lambda_0}{m} \tag{2.55}$$

The laser is incident under the angle θ towards the target normal (figure 2.10). The height of the protuberances is h and the grating period is given by a. The angle α is the reflection/ observation angle. The different interference orders are named with n and the reflected wavelength $\lambda_{\text{reflected}}$ is expressed in reciprocal multiples of the fundamental wavelength λ_0. The angle of incidence is measured with respect to the target normal and the observation angle is measured with respect to the target surface.

Lavocat-Dubuis et al. [15] show efficient harmonic generation along the target surface ($\alpha = 0\,^\circ$ and $180\,^\circ$) in their PIC simulations for two different incidence angles ($\theta = 0\,^\circ$ and $30\,^\circ$) and for grating periodicities as multiples of λ_0. They observed a strong enhancement (factor 10^2) compared to flat targets. At normal incidence ($\theta = 0°$), even harmonics of the order 4, 8, 12, ... were obtained at an observation angle close to the target surface. Contrary to that, at oblique incidence ($\theta = 30°$) harmonics of the order 8, 16, 24, ... stood out. For all the simulations shown in [15] and [16], the effects that occur if a Gaussian laser beam is focused onto a target were neglected, because the laser beam was approximated by a plane wave. By increasing the size of the laser spot on the target, they observed more defined harmonic spectra as more protuberances contribute to the generation process.

In figure 2.11, the spectral distribution of the emitted harmonic generation from two

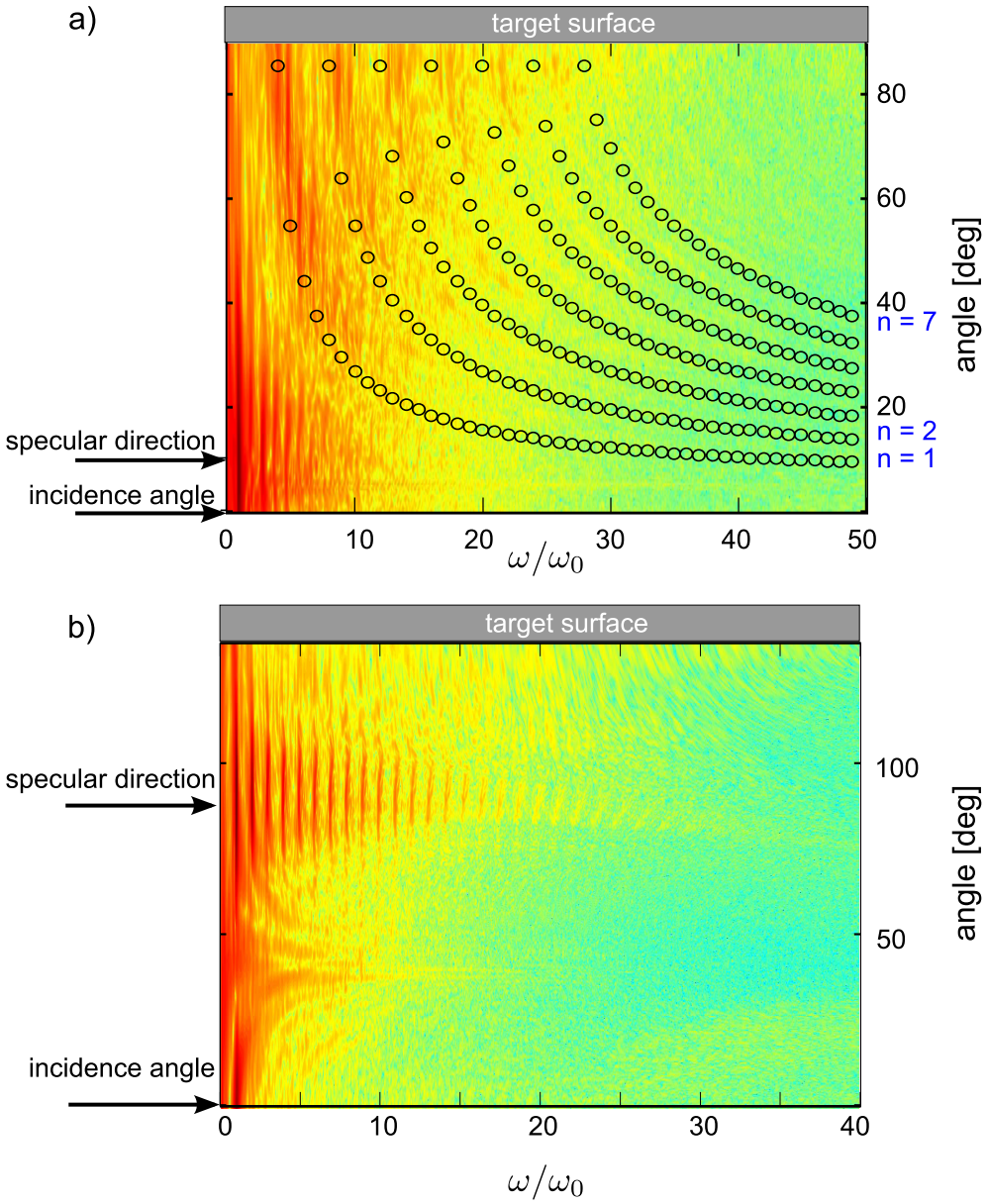

Figure 2.11: Angular distributions of the high harmonic radiation from corrugated and flat targets obtained by 2D PIC simulations with the EPOCH code.
a) Spectrogram of the harmonic generation from corrugated target. The circles mark the harmonic orders which are predicted by the interference formula. The grating periodicity is 220 nm and the incidence angle is 5°. The harmonic spectrum at a distinct observation angle has gaps, especially close to the target surface. The parameter n denotes the interference order. The y-axis shows the angular distribution of the harmonics.
b) Spectrogram of the harmonic generation obtained from a flat target. The incidence angle is 45°. The harmonic emission is concentrated in the specular direction.

different types of targets is depicted. The results were obtained by 2D PIC simulations with the EPOCH simulation code. Part a) shows the harmonic emission for a corrugated target with a periodicity of $a = 220\,\mathrm{nm}$. The angle of incidence is 5°. The circles mark the harmonic orders predicted by the interference formula for seven interference orders ($n = 1, \ldots, n = 7$). Higher-order harmonics can be found close to the target surface (90°). The classical situation for high harmonic generation is shown in part b): The laser is incident under 45° onto a flat target (with respect to the target normal). The harmonics are only emitted in the specular direction of the laser. Their generation efficiency decreases for higher orders. The main difference of both geometries is that the harmonics from grating targets can be detected far away from the specular direction. It is also visible that lower orders are suppressed for observation angles close to the target surface. It has to be stated that the spectral intensity in case of a corrugated target is distributed over a broader angular range. This leads to a lower efficiency of the harmonic if only one observation angle is evaluated.

3 High contrast laser systems

This chapter contains a description of the two different laser systems which were used for the experiments in this thesis. The pulse characteristics of high intensity laser systems are addressed as well. Furthermore, concepts of enhancing the temporal laser contrast ratio of high power systems are introduced. Additionally, the plasma mirror system which was designed for the ARCTURUS laser system to obtain perfect conditions for experiments with high temporal contrast is described. Moreover, contrast measurements of the ARCTURUS laser are presented in this chapter.

3.1 Setup of the ARCTURUS laser system

The first laser system that was used to study relativistic interaction of laser pulses with solid targets, is the ARCTURUS laser, situated at the Heinrich-Heine University in Düsseldorf. The laser is a compact CPA (Chirped Pulse Amplification; principle shown in figure 3.1) system, with peak powers about 100 TW and pulse durations of 25 fs. It is commercially available from *Amplitude Technologies* in France. The system consists of three main parts: 1. the front-end with oscillator, booster amplifier, stretcher, regenerative amplifier and two multipass amplifiers; 2. the main amplifier with a the cryogenically cooled crystal; 3. the grating compressor. Additionally, a second beam line with a second main amplifier

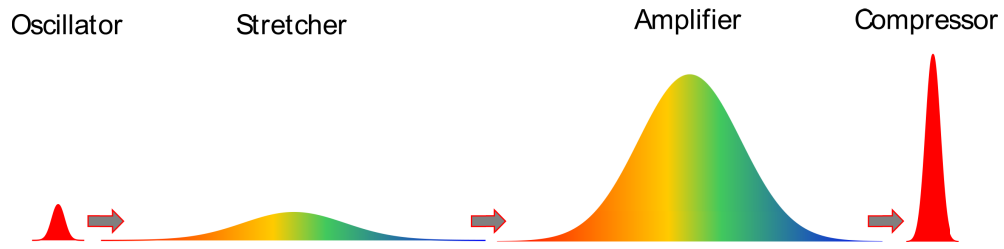

Figure 3.1: Principle of **C**hirped **P**ulse **A**mplification: A short, low intensity pulse is stretched to reduce the peak intensity, strongly amplified and afterwards re-compressed to a high intensity short pulse.

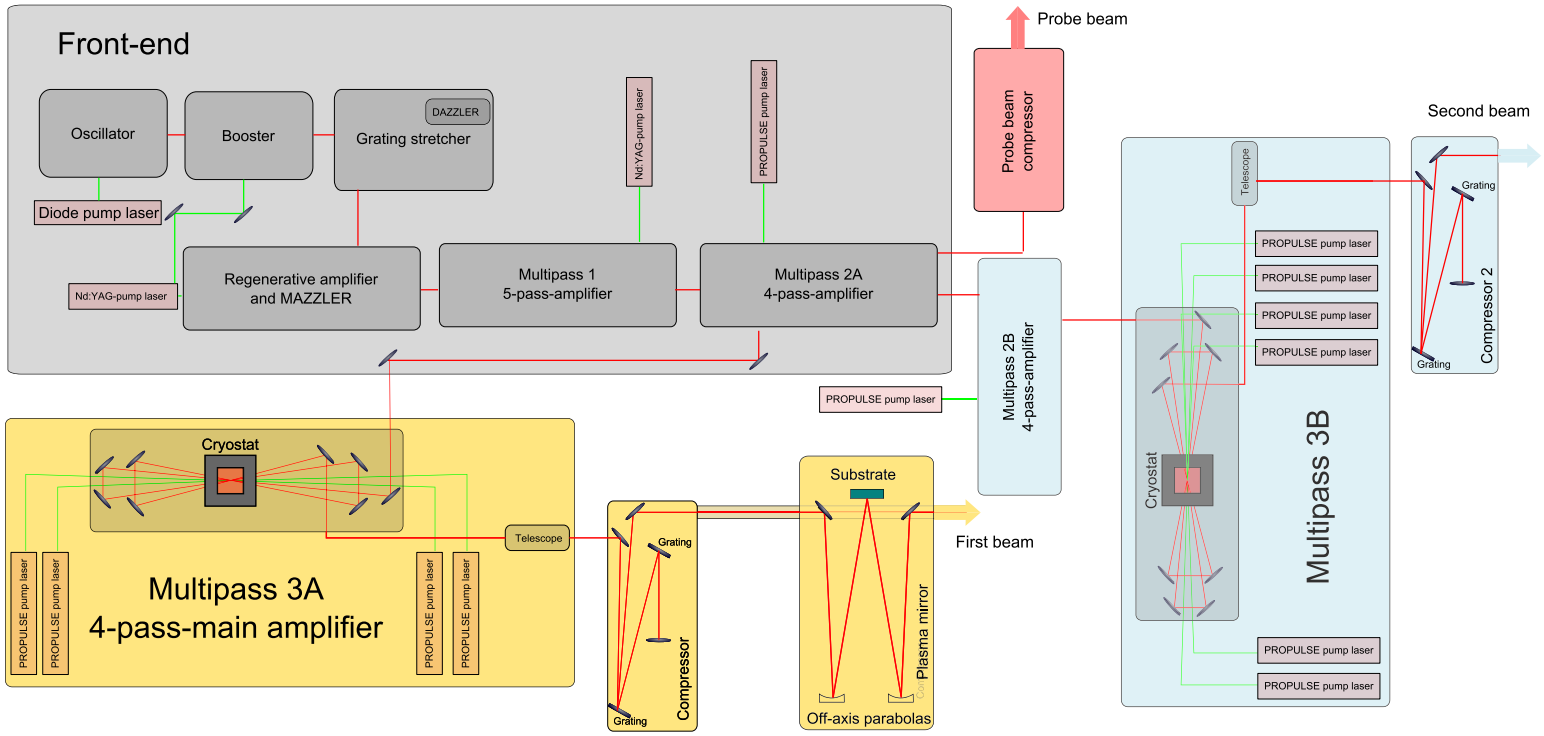

Figure 3.2: Overview of the ARCTURUS laser system at the Heinrich-Heine University Düsseldorf. It consists of the front-end, where the laser pulse is generated, stretched and pre-amplified, the cryogenically cooled main amplifier, grating compressor and plasma mirror (first beam line is shown in yellow). The second beam line with another multipass amplifier (2B) and a cryogenically cooled main amplifier is illustrated in blue. Short pulses (25 fs) with several millijoule of pulse energy can be obtained in the probe beam line (red).

also including a cryogenically cooled crystal, reaching higher pulse energies, was installed recently (see figure 3.2). The ARCTURUS laser system will be described in detail in the following:

Oscillator

The Kerr-lens mode-locked Synergy oscillator is a titanium-doped sapphire (Ti^{3+}:Al_2O_3 or shortly: Ti:Sa) laser, which is pumped by a 5 W continuous wave (cw) diode laser. The central wavelength is around 790 nm with a corresponding bandwidth of $\sim$ 96 nm. The oscillator generates pulses with 23 fs duration at a repetition rate of 75 MHz and a pulse energy of 5 nJ.

Booster Amplifier

The booster is an amplifier which intensifies the energy up to the microjoule level and enhances the temporal contrast at the same time. It contains a Pockels cell which acts as a pulse picker. The repetition rate is reduced to 10 Hz. A saturable absorber cleans the pulse from ASE (amplified spontaneous emission). The multipass amplifier is pumped by a frequency doubled Nd:YAG laser (CFR Ultra).

Stretcher

Afterwards, the pulse is stretched up to $\sim$ 500 ps in the stretcher module in order to reduce the peak intensity for the following amplification stages. The Offner stretcher is free of chromatic aberration, because it only contains two concentrically mounted spherical mirrors. Only symmetrical aberrations can occur as a consequence of this 1/1 telescope. Inside the stretcher, an acousto-optical filter, called DAZZLER[1], is placed, which compensates the group velocity dispersion in order to improve the contrast for later compression. The phase of the pulse can be controlled and adjusted by a computer programme. Using the SPIDER technique (see also section 4.1), the shortest pulse duration can be achieved by flattening the phase to the minimum.

1 Pulse shaper or **A**cousto-**O**ptic **P**rogrammable **D**ispersive **F**ilter (AOPDF), available from FASTLITE, France.

Regenerative Amplifier

The titanium-doped sapphire crystal inside the regenerative amplifier is also pumped by the CRF Ultra Nd:YAG laser. One Pockels cell is used to seed the amplifier cavity with the pulse coming from the stretcher module. The outcoupling takes place after several round trips with a second Pockels cell and a polarising beam splitter. The regenerative amplifier increases the energy up to 1 mJ. To avoid gain narrowing effects, a second acousto-optic element (MAZZLER) is used to flatten the central part of the spectrum which is strongly amplified during the round trips. This technique allows the generation of a broad spectrum even after strong amplification.

Multipass 1, Multipass 2A and probe beam

The first main amplifier is a 5-multipass system, which is pumped by a CRF 200 Nd:YAG laser (pulse energy 120 mJ). The energy is increased from 1 mJ up to 23 mJ in this stage. Before the beam passes the second main amplifier (Multipass 2A), it is expanded by a lens telescope. This amplifier stage is pumped with 2 J by a PROPULSE frequency doubled Nd:YAG laser. After these four passes, the pulse has an energy of 600 mJ. A 50:50 beamsplitter divides the beam into first and second beam. Afterwards, 5 % of the 300 mJ of the second beam are split up into the second main beam line and the probe beam line. In order to obtain the perfect timing of the laser pulses, the probe beam line contains several delay stages to match the propagation length for the different experimental chambers in the radiation shielded target area. The probe beam can be compressed to 25 fs.

3A Main Amplifier (first beam)

The titanium-doped sapphire crystal in the final amplification stage is cryogenically cooled in order to avoid thermal lensing and to keep the fluence below the damage threshold of the anti-reflective coating of the crystal. The four-pass system is pumped by four PROPULSE frequency doubled Nd:YAG lasers with 8 J (2 J each). The size of the crystal is $5\times5\times3\,\mathrm{cm}^3$. The resulting beam diameter is 3.3 cm. After this amplification up to 3.1 J, the beam is again expanded to a diameter of 8 cm by a telescope.

Compressor (first beam)

The vacuum compressor contains two gold coated, parallel aligned gratings which allow a compression down to 23 fs. The transmission of the compressor is $\sim 60\,\%$. It is possible to obtain 2 J on the target which corresponds to an intensity of $10^{20}\,\mathrm{W/cm^2}$ in the focal spot of an f/2 off-axis parabolic mirror.

Plasma mirror

After compression, the pulse is cleaned from ASE and the possible prepulses by a plasma mirror system, which will be discussed in detail in chapter 3.3.

Adaptive optics (optional)

The adaptive mirror contains 32 piezo driven elements, which can be controlled by a computer software using a Shack-Hartmann sensor for wavefront analysis. The surface of this mirror can be smoothed in a way that the wavefronts are corrected to achieve the best focal spot inside the target chambers.

Second beam line (Multipass 2B, 3B Main Amplifier, Compressor)

To ensure a sufficient amount of energy for the second beam, another multipass amplifier, which is pumped by a PROPULSE Nd:YAG laser with 1.2 J, is used to reach 600 mJ before the last amplification stage of the second beam.

The second beam line consists of a second big (3B main) amplifier, a second compressor and an adaptive mirror. By using five of the PROPULSE lasers operating with LBO-crystals instead of KDP-crystals for frequency doubling, each pump laser emits 2.5 J. The resulting pulse energy of the amplified pulses is 4 J before the compressor stage. A second plasma mirror system is planned to be implemented after the compressor.

3.2 Pulse characteristics of high intensity laser systems

Due to the CPA amplification mechanism, the main pulse is accompanied by a nanosecond pedestal and prepulses (see figure 3.3). This implicates that the main pulse cannot interact with a cold target but rather with an expanding plasma. The prepulses are strong enough

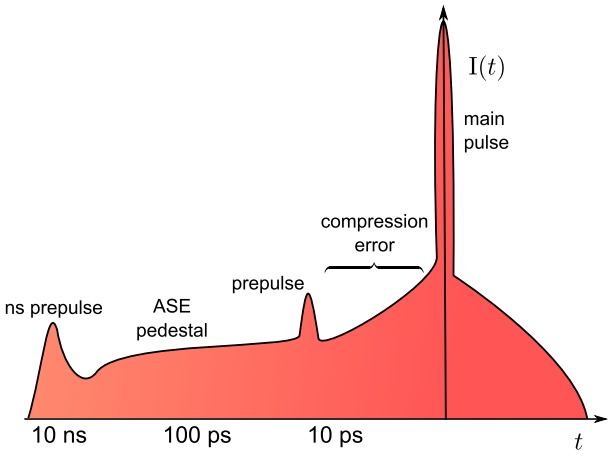

Figure 3.3: Schematic characteristics of high power laser pulses: nanosecond prepulse, ASE pedestal, prepulses and compression error prior to the main pulse.

to ignite a preplasma and ionise the target strongly, before the main pulse reaches the target. To perform experiments with either very thin or specially structured targets, the laser contrast needs to be improved. The temporal contrast is determined by the relation between the maximum intensity and the intensity at any time:

$$C(t) = \frac{I_{\max}}{I(t)} \tag{3.1}$$

On the nanosecond time scale, amplified spontaneous emission is the dominating process generating the pedestal (see figure 3.3). The ASE level mainly depends on the fluorescence lifetime of the gain material, which is 3.2 µs (for T = 300 K for titanium-doped sapphire [122]). Femtoseconds before and after the main pulse, short pulses can be observed due to uncompressed dispersion. The usage of high gain amplifiers contributes substantially to the pedestal. The imperfectness of polarisers inside Pockels cells causes further contrast degradation due to arising prepulses on the nanosecond time scale.

3.2.1 Different ways to enhance the temporal laser contrast

To ensure an interaction of the laser pulse with a steep plasma density gradient, a contrast enhancement is required. This becomes especially important at laser intensities of $10^{20}\,\mathrm{W/cm^2}$, as even prepulses which are seven orders of magnitude less intense still start to ionise the target. There are many different techniques which can improve the temporal contrast of a laser system by several orders of magnitude. Electro-optic techniques can

only be used to remove prepulses on the nanosecond time scale. Also nonlinear processes (i.e. frequency doubling) and especially the **O**ptical **P**arametric **C**hirped **P**ulse **A**mplification (OPCPA) are able to enhance the contrast of a laser system considerably. Other opportunities are saturable absorbers, the cross-polarised wave generation or plasma mirrors which will be discussed below.

Cross-polarised wave (XPW)

One of the various different ways to enhance the temporal contrast is the cross-wave polarisation method (XPW). In this technique, a crystal (i.e. BaF_2) with a $\chi^{(3)}$-nonlinearity of the susceptibility tensor is placed between two polarisers (see figure 3.4). In the four-wave mixing process, the fundamental wave is generated intensity-dependent with an orthogonal polarisation behind the crystal. This method can improve the contrast ratio by 3–5 orders of magnitude and is limited by the extinction ratio of the polarisers [123, 124]. The efficiency is around 10 %, hence an additional amplification stage is needed.

Saturable absorbers

A saturable absorber (SA) is an intensity-dependent switch. The losses of the SA are reduced for high intensities and the material becomes transparent. Either dyes, semiconductor saturable absorber mirrors (SESAM) or grey filters are implemented in different laser systems. They are used for passive mode locking as well as for Q-switching of lasers. The ARCTURUS laser has a grey filter inside the booster amplifier which suppresses the nanosecond pedestal of about one order of magnitude (see section 3.2.3).

Plasma mirrors

The idea of enhancing the laser contrast ratio of femtosecond laser pulses by the reflection from overdense plasmas, generated on glass substrates, is quite old [125]. It gained more

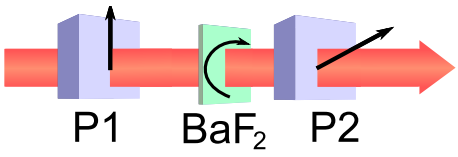

Figure 3.4: Principle of cross-wave polarisation (XPW): BaF_2-crystal is placed between two polarisers.

interest when high power laser systems became more widely accessible [126, 127] during the last decade. The working principle and the setup of the ARCTURUS plasma mirror are described in detail in section 3.3.

3.2.2 Third-order autocorrelators

Laser pulses with femtosecond pulse durations are too short to be measured by photodiodes or other electronic devices. Second-order autocorrelators are utilised commonly in order to estimate pulse durations. The intensity autocorrelation $A_2(\tau)$ of a laser pulse with an intensity distribution $I(\tau)$ is defined as

$$A_2(\tau) = \int_{-\infty}^{\infty} \mathrm{d}t I(t) I(\tau + t) \tag{3.2}$$

[128]. Pre- or postpulses cannot be differentiated by this type of autocorrelation, because the second-order function is symmetric. Furthermore, rapid changes in the temporal profile are smoothed and are not resolved. The temporal profile of an ultrashort laser pulse can be resolved by using third-order autocorrelators [129].

To enhance the dynamic range of an autocorrelation, two nonlinear processes are required. Firstly, a second harmonic generation leads to $I^2(t)$, and afterwards the correlation between $I^2(t)$ and $I(t)$ is obtained via sum frequency mixing. The resulting asymmetric third-order autocorrelation function is:

$$A_3(\tau) = \int_{-\infty}^{\infty} \mathrm{d}t I^2(t) I(\tau + t). \tag{3.3}$$

3.2.3 SEQUOIA apparatus and laser contrast measurements

The SEQUOIA[2] apparatus is a third-order autocorrelator which allows to conduct measurements of the laser pulse contrast on a picosecond time scale. The device, which was used for the measurements shown in this section and the chapter about plasma mirrors (chapter 3.3), has a high dynamic range of ~ 12 orders of magnitude. The cross-correlation is obtained via sum frequency generation between the second harmonic and the pulse itself.

2 Distributed by Amplitude Technologies, France.

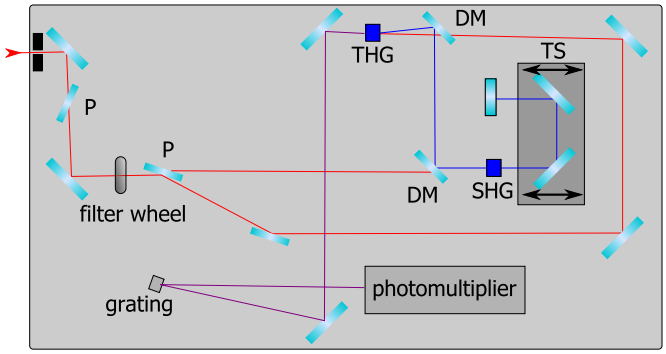

Figure 3.5: Setup of the SEQUOIA apparatus (Amplitude Technologies): **P**: polariser, **DM**: dichroic mirror, **SHG**: second harmonic generation crystal, **THG**: third-order harmonic crystal and **TS**: translation stage.

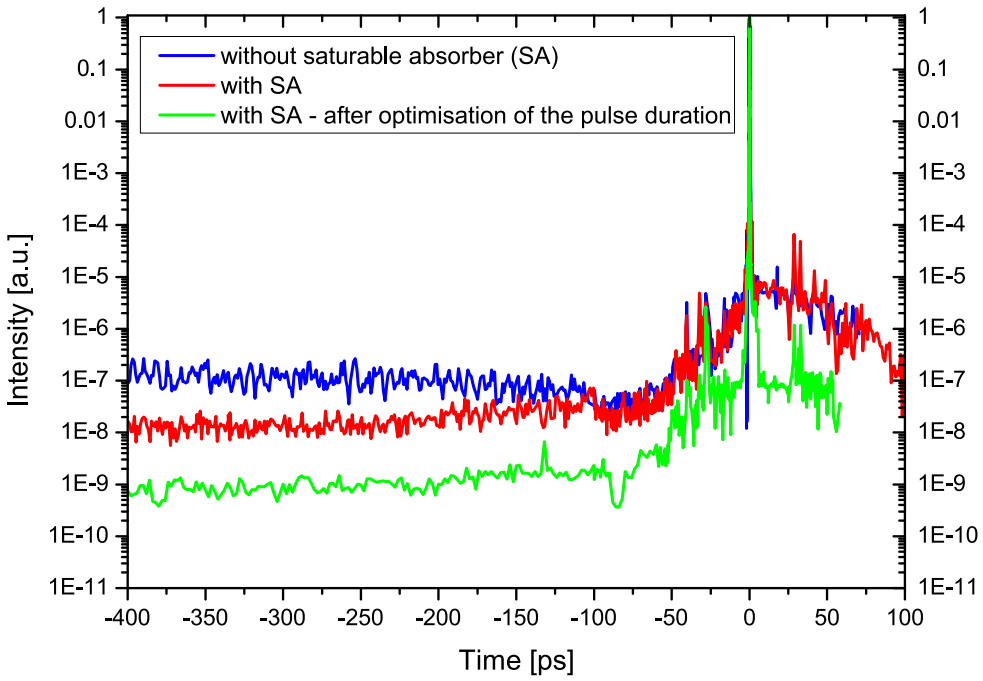

Figure 3.6: SEQUOIA measurements of the ARCTURUS laser *with* and *without* a saturable absorber placed inside the booster amplifier.

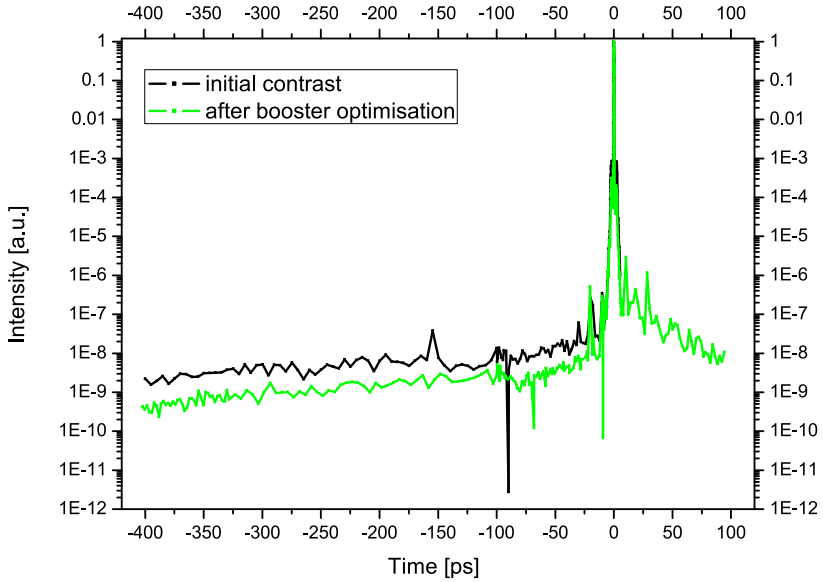

Figure 3.7: SEQUOIA measurements of the ARCTURUS laser: The black curve shows the initial temporal profile with the small negative peak at ∼ -90 ps indicating the maximal dynamic range of the device. The green curve depicts the temporal profile after the optimisation of the SA position inside the booster amplifier.

The second harmonic pulse is delayed by a computer-controlled translation stage with a delay range of ∼ 500 ps. Afterwards, the second harmonic and the fundamental pulse pass through a third-order crystal in a non-collinear geometry. A 'solar blind' photomultiplier is used for the detection of the signal. The computer-controlled calibrated attenuator (filter wheel) ensures the high dynamic range of the measurement. The SEQUOIA trace allows a comparison between the level of the ASE compared to the main pulse. Ghost pulses, which can occur from dielectric coatings and birefringent optics, can be identified as well. The setup of the apparatus is depicted in figure 3.5.

Figure 3.6 shows typical contrast measurements of the ARCTURUS laser system. A saturable absorber (SA) can be placed inside the booster amplifier stage. The comparison of the blue and the red curve illustrates the influence of the SA on the ASE pedestal. Without the SA, the ASE level is rather high ($\sim 2 \times 10^7$) and has a decreasing tendency towards the main pulse (-400 to -120 ps) due to the fluorescence lifetime of the titanium sapphire crystals. By placing the SA into the laser system, the ASE level becomes one order of magnitude lower and slowly increases from -200 ps onwards. An optimisation of the pulse duration via SPIDER measurement and thereby adjustment of the DAZZLER settings, improve the whole temporal contrast further by more than one order of magnitude. Also the time scale from

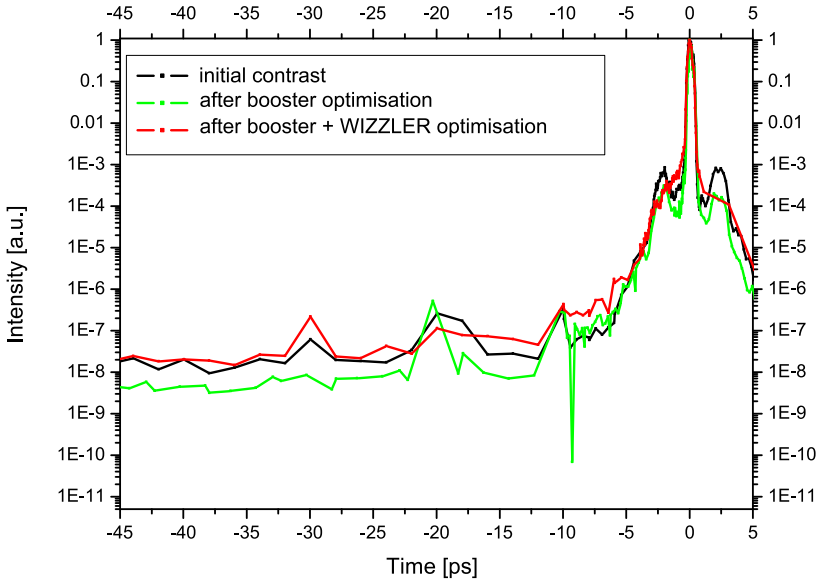

Figure 3.8: SEQUOIA measurements of the ARCTURUS laser: black and green curve are the same as in figure 3.7 but closer to the main pulse. The red curve shows the temporal contrast after an additional improvement of the pulse duration by using a WIZZLER device. The wings at ±2 ps can be flattened.

100 ps before the main pulse, which corresponds to incomplete compression, is affected. On the one hand, the dynamic range of the recorded signal depends on the noise level of the photomultiplier, on the other hand, it depends on the saturation level of the photomultiplier with the highest neutral density filter.

In figure 3.7, the black curve shows the initial temporal profile, with the small negative peak at ∼-90 ps indicating the maximal dynamic range of the device. This can be obtained by blocking the incoming laser light shortly during the measurement. The green curve depicts the temporal profile after the optimisation of the SA position inside the booster amplifier. Figure 3.8 illustrates the temporal profile for three different settings: The black and the green curve are the same as in figure 3.7 but on a time scale closer to the main pulse. Strong 'wings' at ±2 ps are visible. Thus, after the changes of the booster amplifier, an optimisation of the pulse duration by using the WIZZLER[3] was necessary. The red curve illustrates the drawback which occured after this WIZZLER measurement: Although the 'wings' are reduced, the temporal contrast on the time scale -5 to -45 ps becomes worse.

3 Device to measure the pulse duration and phase via self-reference spectral interferometry applying cross-polarised wave generation (XPW), distributed by FASTLITE, France.

Consequently, another loop of optimisation of the booster, MAZZLER, etc. is necessary. Thus, it becomes clear that the improvement of the laser contrast is an iterative process where many components of the laser system play important roles.

3.3 Laser contrast enhancement with plasma mirrors

The very first attempts of using self-induced plasma shuttering were made in the early nineties of the last century by Kapteyn et al. [125]. Gold et al. could prove a drastic enhancement of the temporal contrast of a laser pulse measured with an autocorrelator by using p-polarised incidence at the Brewster angle [130]. Since lasers with several terawatts of intensity became more widely available, intensive studies on the properties of plasma mirror systems have been carried out during the last ten years [126, 131, 132, 133, 134].

In order to perform experiments with a small scale length of the preplasma, the contrast needs to be enhanced. This can be achieved by the means of plasma mirror shuttering. Anti-reflective coated substrates are used to improve the temporal contrast ratio of terawatt laser systems substantially. The principle of the plasma mirror shuttering is illustrated in figure 3.9. The laser pulse is focused onto the coated glass substrate, so that the prepulses and the ASE pedestal are still transmitted. The rising edge of the main pulse ignites an overdense plasma and the main pulse is reflected. In this way, the plasma mirror acts as a

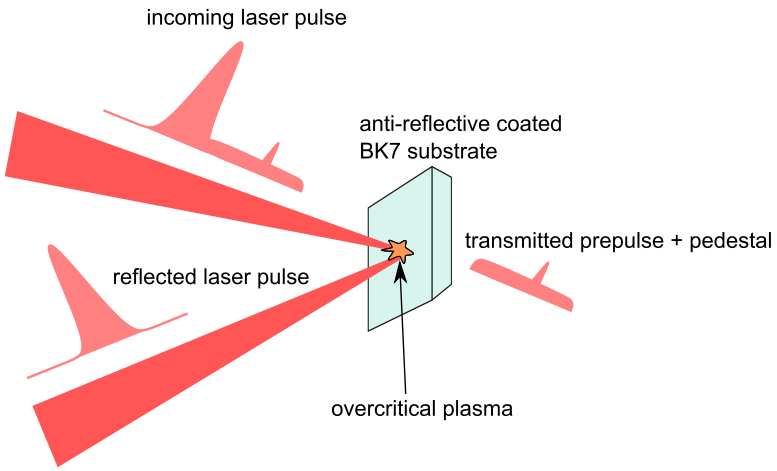

Figure 3.9: Plasma mirror principle: The prepulse is transmitted through the AR-coated surface. The rising edge of the main pulse ignites an overdense plasma, hence the high intensity part of the laser pulse is reflected.

switch with femtosecond response time. In several groups working with high power lasers, a significant enhancement of the contrast could be observed [127, 135]. The damage threshold of dielectric materials (fused silica, BK7) is $\sim 10^{13}\,\mathrm{W/cm^2}$ [136, 137]. Since the plasma mirror substrate is destroyed after each laser pulse, the idea of using a self-replacing target such as a fluid came up soon [138, 139], in order to allow high repetition rates. Usually, the transmitted energy of a plasma mirror system lies between 60–80 % of the incoming laser pulse [133, 131]. By using a double plasma mirror with two consecutive substrates, still 30–65 % transmission can be obtained [140, 141, 142].

The setup of the plasma mirror (PM) needs to be suitable to the laser system it is designed for. The intensity on the substrate has to be high enough to create an overdense plasma exactly at the rising edge of the main pulse. If the intensity is too high, prepulses are partially reflected and trigger the plasma mirror too early. For longer pulses ($\sim$ps), this can result in an already expanded mirror surface of the PM and distort the phase fronts of the reflected beam severely [126]. The plasma expands approximately with the ion sound velocity c_s of $\sim 3 \times 10^5\,\mathrm{m/s}$. Thus, the pulse duration must be shorter than $\sim 2\,\mathrm{ps}$ in order to guarantee a plasma scale length ($L_p = c_s t$) which is significantly lower than a laser wavelength of $\lambda = 800\,\mathrm{nm}$. Of course, the expansion velocity depends on the ionic temperature, hence the incident fluence should be low enough.

The achievable contrast enhancement is given by the ratio of the reflectivity of the plasma and the cold reflectivity of the target [132]:

$$\Delta C = \frac{R_{\mathrm{plasma}}}{R_{\mathrm{cold}}} \tag{3.4}$$

Thus, the contrast enhancement is higher, the better the anti-reflective coating of the PM substrate is.

There are two setup configurations to insert a plasma mirror system into the laser beam path. In case of a multi terawatt laser system like the ARCTURUS laser, it is possible to place it right after the compressor stage, several meters away from the experimental chamber. Two off-axis parabolic mirrors are needed for this kind of setup, which will be described in the following paragraph. Another configuration which is used in petawatt class laser systems (i. e. VULCAN Petawatt in the Rutherford Appleton Laboratory, Central Laser Facility in UK), consists of a plasma mirror substrate, which is placed into the focusing beam of the regular off-axis parabolic mirror in the target chamber [143]. This induces some practical problems in the experimental process. In order to replace the substrate, the target chamber must be vented, and also the alignment is more challenging.

The intrinsic contrast ratio between main pulse and pedestal of the ARCTURUS laser is

quite high (10^9; see also section 3.2) even without the plasma mirror. An intensity of $10^{16}\,\mathrm{W/cm^2}$ on the PM substrate ensures a complete triggering and a suppression of the ASE (and possible prepulses) by approximately three orders of magnitude, if anti-reflective coated targets are used. Hörlein et al. report efficient spatial filtering in the far field for intensities of $10^{19}\,\mathrm{W/cm^2}$, which are much higher than in most of the plasma mirror setups [144]. As a consequence of this high intensity, a significant amount of energy is converted into the second harmonic of the fundamental wavelength which is not necessarily desirable for further experiments. Nevertheless, these properties made the PM itself interesting for investigating high harmonic generation from plasma mirror targets as well [134].

3.3.1 Setup of the ARCTURUS plasma mirror

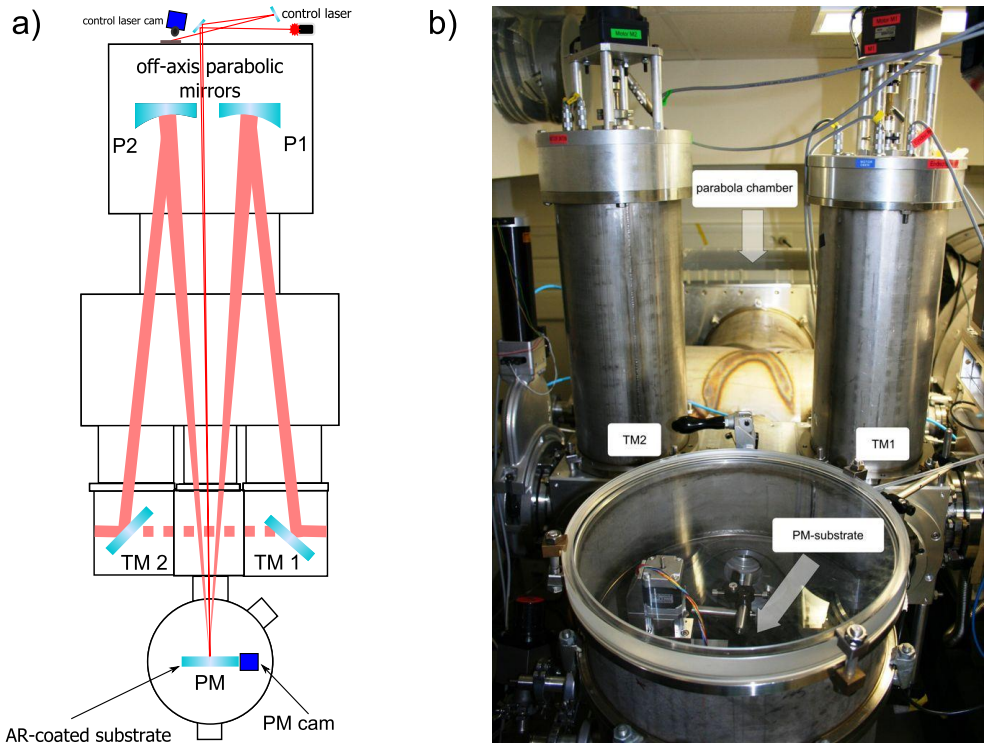

Figure 3.10: Plasma mirror setup in the ARCTURUS laser laboratory
a) Sketch of the PM setup: Laser beam comes from the right-hand side onto TM1, is focused by off-axis parabolic mirror P1 onto the PM substrate and afterwards re-collimated by P2 and redirected into the beam line by TM2.
b) Photo of the PM situated directly after the compressor stage of the ARCTURUS laser: Turning mirrors TM1 and TM2 can be driven out of the beam path so that the PM can be bypassed.

This section contains a presentation of the setup of the plasma mirror designed for the Düsseldorf ARCTURUS laser system. Design aspects for the construction of the PM were the parameters of the ARCTURUS laser such as pulse duration, intensity and the geometrical limitation in the laser room as well as the possibility of a quick replacement of the PM targets. One big advantage of the plasma mirror is that the laser system itself does not have to be changed as for XPW and that the input power is principally not limited. The PM is situated after the compression stage where the ultra intense pulse is short. A six inch turning mirror (TM1), which can be inserted into the beam path by a motor, directs the laser pulse onto the first four inch off-axis parabolic mirror (P1; effective focal length f = 1524 mm). The beam is focused onto the anti-reflective coated substrate (PM) to a radius of 350 µm (FWHM[4]) at an intensity of 1–2×10^{16} W/cm^2, so that an overdense plasma is ignited by the main pulse. The angle of incidence on the PM substrate is kept very small (2.4 °), hence resonance and Brunel type absorption do not contribute significantly to the energy loss.

After the reflection from the overdense plasma, the beam is re-collimated by a second off-axis parabolic mirror (P2; f = 1524 mm). Afterwards, the cleaned laser pulse is redirected into the beam line by the outcoupling mirror (TM2), which is also automatically insertable. The plasma mirror system is fully motorized and all motors have encoders for exact alignment. By the means of two apertures placed in front of the two off-axis parabolic mirrors, the beam position can be examined every day. The substrate has to be moved after each shot, since the surface is destroyed by the interaction with the strong laser pulse. In order to sustain the alignment, a red diode laser is used, which is overlapped with the Ti:Sa laser on the substrate with the help of a CMOS camera (PM cam in Figure 3.10). The back-reflection of the red diode from the PM substrate can be checked with the control laser camera during the shots. With the help of the back-reflection of the diode laser, an already damaged PM surface can be identified.

Off-axis parabolic mirrors

To focus high laser intensities, off-axis parabolic mirrors, which are produced out off a section of a paraboloid, are commonly used (see figure 3.11). The aperture number is given by:

$$F_{\#} \sim \frac{f}{2w} \tag{3.5}$$

4 Full width at half maximum.

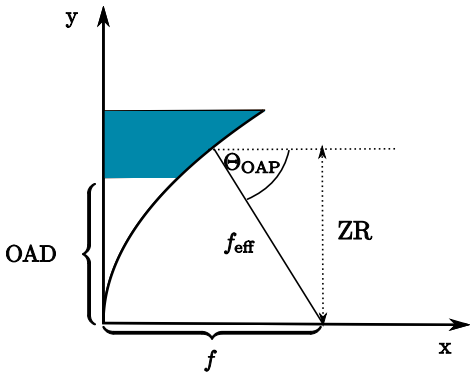

Off-axis parabolic mirrors used for the plasma mirror	
ZR	254 mm
f_{eff}	1543 mm
f	1532 mm
Θ_{OAP}	9.39 °

Figure 3.11: 2D sketch of an off-axis parabolic mirror: effective focal length f_{eff}, off-axis angle Θ_{OAP}, off-axis distance OAD and zonal radius ZR. The section of the paraboloid used for the off-axis parabolic mirror is shown in blue.

Therefore, the minimum focal radius can be estimated:

$$w_{0,\text{min}} \sim \frac{2\lambda F_{\#}}{\pi} \tag{3.6}$$

The distance from the parabola apex to the centre of the off-axis parabolic mirror is called zonal radius ZR. The effective focal length of an off-axis parabolic mirror can be calculated by the equation:

$$f_{\text{eff}} = \frac{2f}{1+\cos(\Theta_{\text{OAP}})} \tag{3.7}$$

To obtain the off-axis angle, the following equation can be used:

$$\tan(\Theta_{\text{OAP}}) = \frac{ZR}{f_{\text{eff}}} \tag{3.8}$$

Figure 3.11 contains the information about the parabolic mirrors used in the plasma mirror setup. The focal spot of the off-axis parabolic mirror P1 is 25.5 µm (FWHM) (see figure 3.12 a)). In order to reach an intensity of $\sim 10^{16}$ W/cm^2, the plasma mirror substrate has to be moved 24 mm out of focus (see figure 3.12 b)).

Plasma mirror targets

The PM substrate itself should have an optical quality with a low surface roughness ($\sim \lambda/10$ on any $\oslash$ 5 mm). Two different kinds of plasma mirror targets were used for the experiments.

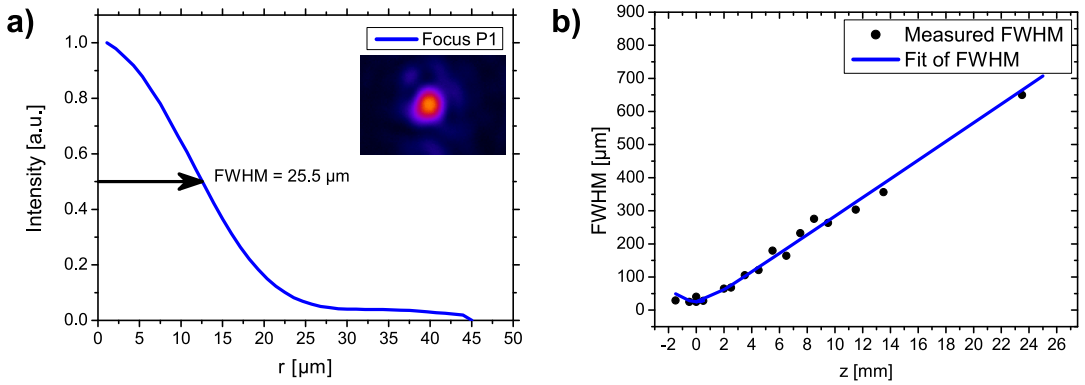

Figure 3.12: a) Focus of the off-axis parabolic mirror P1 recorded with microscope lens and camera.
b) Beam diameter (FWHM) for different z-positions of P1 recorded with PM cam.

By using uncoated BK7 substrate, a medium contrast can be obtained [133]. Multilayer AR-coated targets provide anti-reflective features for wavelengths between 750–850 nm. The maximum reflectivity of the 'cold' substrate is 0.17 %. Additionally, the AR substrates are coated with a 5×100 mm silver stripe for higher reflectivity allowing an easier alignment in the target chambers. The damage size of each shot on the substrate is ∼2 mm in diameter. Up to 550 shots can be placed on one plasma mirror target without venting the system. Since the substrate compartment has a separate vacuum shutter, the targets can be replaced within several minutes without breaking the vacuum of the whole PM chamber.

3.3.2 Characterisation of the plasma mirror

In order to find the optimal operation regime for the plasma mirror system, the transmission was measured by placing a calorimeter after the outcoupling mirror. The AR-coated substrate was moved in z-direction towards the focus of the plasma mirror parabola P1. The efficiency of the PM drops significantly for z-positions very close (<1 cm) to the focus (see figure 3.13). Moreover, the energy varies stronger from shot to shot, due to too early triggering of the PM. At the position 2.4 cm out of focus of off-axis parabolic mirror P1, the transmission efficiency is around 74 % which corresponds to an intensity of $1.3 \times 10^{16}\,\mathrm{W/cm^2}$ on the substrate. Measurements applying intensities above $3 \times 10^{16}\,\mathrm{W/cm^2}$ where only made once in 2011, because high intensities enabled prepulses to trigger the PM, and the reflection from the plasma was occasionally scattered strongly. The early triggering of the PM causes the main pulse to be reflected from an already expanding surface and thus it becomes possible that optics along the beam path are destroyed due to the changed beam divergence. As Ziener

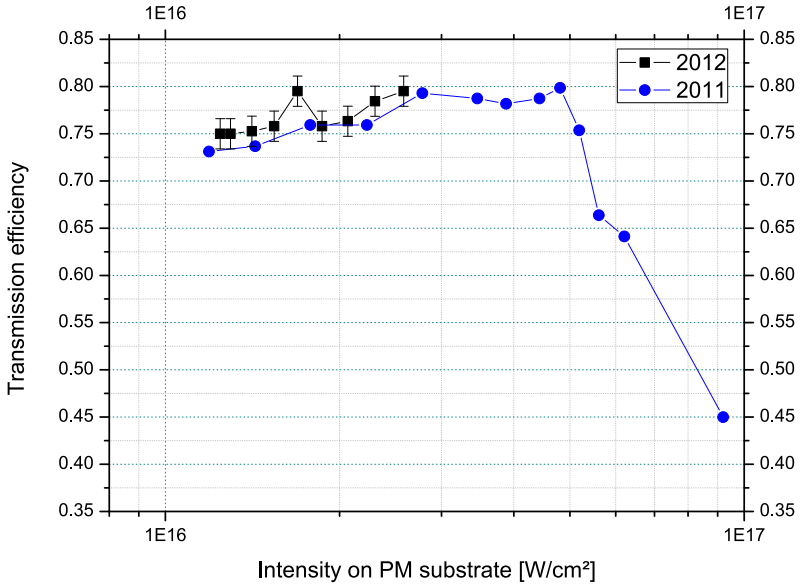

Figure 3.13: Transmission of the plasma mirror for different laser intensities on the PM substrate. The PM target was shifted towards the focus of off-axis parabolic mirror P1.

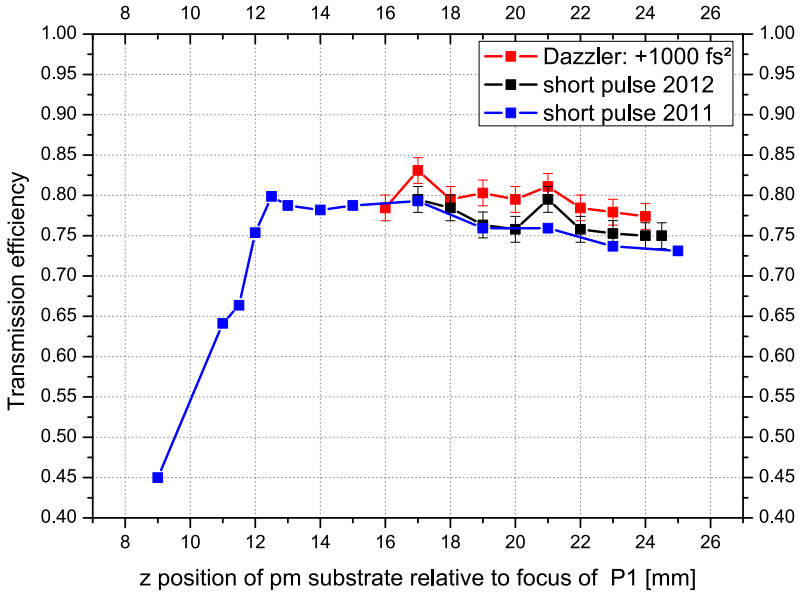

Figure 3.14: Transmission of the plasma mirror for different DAZZLER settings. The x-axis illustrates the PM substrate position with respect to the focus of off-axis parabolic mirror P1. The black and blue curves show the short pulse measurement (25 fs) depicted in figure 3.13. The red curve shows the PM transmission for $D_2 = +1000\,\mathrm{fs}^2$ (~ 100 fs).

et al. had shown for longer pulses (90 fs) [131], the transmission drops if the intensity on the surface exceeds $\sim 10^{17}\,\mathrm{W/cm^2}$ because of enhanced resonance absorption and vacuum heating. Additional problems occur if the intensity is too high: Due to the early ignition of the overdense plasma, parts of the prepulses and/or ASE can be reflected by the PM. The expansion of the overdense plasma can lead to a distortion of the phase fronts of the reflected beam. The reason for using off-axis parabolic mirrors with a very long focal length is that the desired intensity on the substrate should be reached with 'smooth' focusing in order not to destroy the phase fronts of the reflected laser pulse. This is necessary because the target chambers are several meters away from the plasma mirror system. The second curve in figure 3.13 taken in 2012 has a slightly higher efficiency because the initial contrast of the laser was better in this case and thus the loss of the transmitted ASE/prepulses was lower.

Figure 3.14 additionally shows a transmission measurement for a chirped laser pulse. This was obtained by adding a D_2 of $1000\,\mathrm{fs^2}$ in the settings of the DAZZLER. This corresponds to a pulse duration[5] of ∼100 fs.

3.3.3 Full power optimisation

As it is very important to maintain the quality of the focal spot when a plasma mirror is used, the focus in full power shots without PM was compared to the focus of the beam passing through the plasma mirror. In order to measure the spot size, two strong neutral

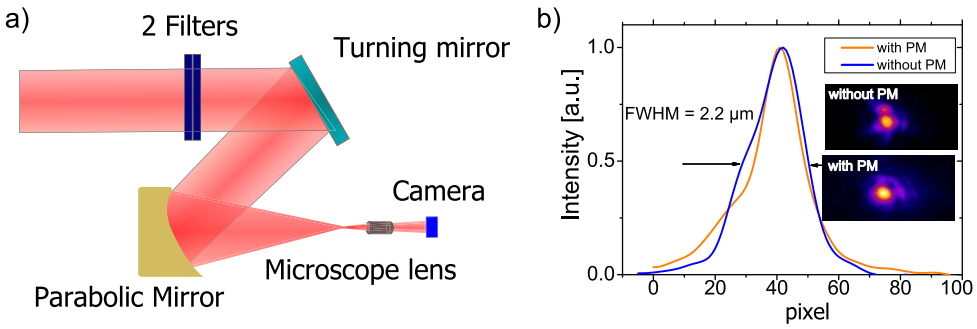

Figure 3.15: a) Setup for checking the plasma mirror alignment in full power shots. **b)** Measurement of the focal spot obtained with the microscope lens. The FWHM of the focus is ∼2.2 µm in both cases.

5 According to the pulse lengthening for Gaussian laser pulses $\Delta\tau = \tau_0\sqrt{1+(4\ln 2\frac{D_2}{\tau_0^2})^2}$.

density filters were inserted into the beam path in the target chamber right before the turning mirror. By inserting a microscope lens (with ten times magnification), which is commonly used for focal diagnostics, the focus was imaged onto a CCD camera (see figure 3.15). The spot size of the focus did not change for the operation with and without PM. This procedure was tested before the first experiments, hence the focus quality and beam pointing were guaranteed for the measurements.

3.3.4 Ion acceleration from thin DLC targets

As a first test of the improved laser contrast by applying the plasma mirror, an experiment for proton acceleration from very thin (d = 10 nm) foils was accomplished. This was done at the same time as the experiment to calibrate the Thomson spectrometer setup (see diploma thesis S. Spickermann [145]). The Thomson spectrometer consists of a pinhole, an electric and magnetic field, both applied in a parallel direction, perpendicular to the propagation path of the ions. After a short free path, the ions enter a multi-channel plate (MCP) which multiplies the signal. The screen is imaged by a camera. As each ionisation stage has a different charge-to-mass ratio, they can be distinguished by the different parabolas which becomes visible on the phosphor screen.

The setup of the experiment is depicted in figure 3.16. The DLC foils (**D**iamond-**l**ike **C**arbon) were mounted on 100 lpi (lines/inch) copper meshes. The angle of incidence was 45 degree.

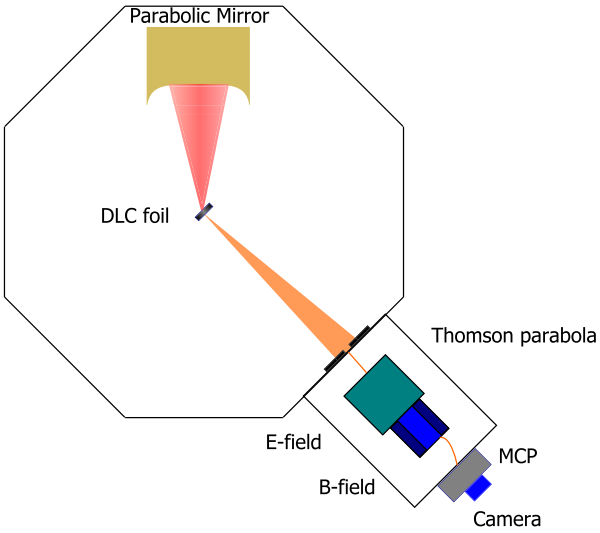

Figure 3.16: Experimental setup: Proton acceleration from DLC foils.

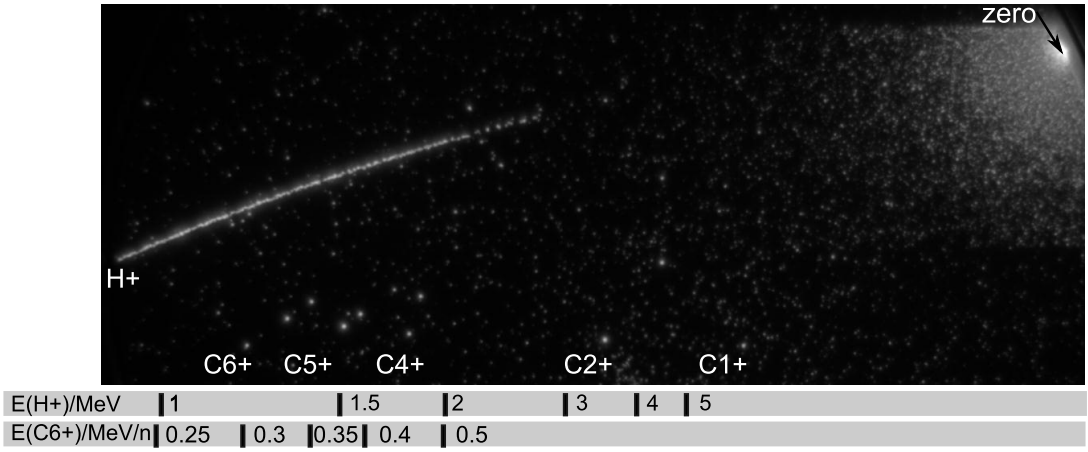

Figure 3.17: Shot 6: Ion acceleration from 10 nm DLC foil; maximum proton energy 2.5 MeV. The bright spot in the right corner is the vertex of the parabolas.

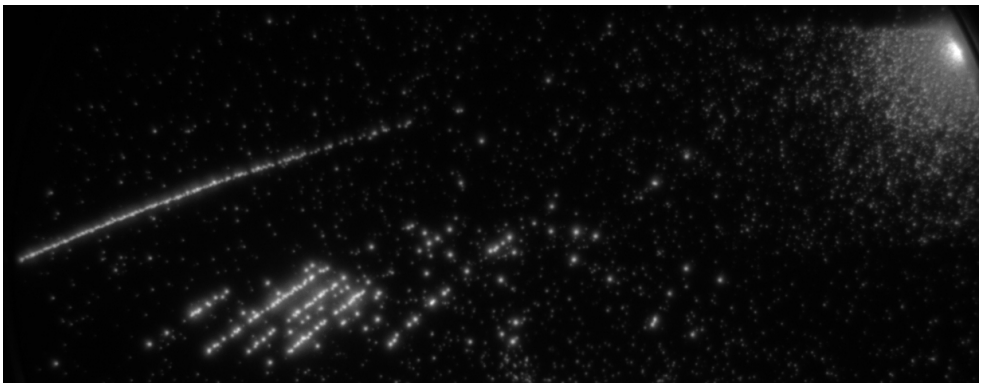

Figure 3.18: Shot 7: Ion acceleration from 10 nm DLC foil; maximum proton energy 2.3 MeV; several distinguishable ionisation stages: C^{+}, C^{2+}, C^{3+}/O^{4+}, C^{4+}, C^{5+}, C^{6+}/O^{8+}.

The Thomson parabola was mounted at the emission angle normal to the target surface. Figure 3.17 shows an image from the phosphor screen. The bright spot in the right corner emerged from the X-ray photons which are not deflected by magnetic or electric fields and thus enable a zero point for the identification of different energies and ionisation stages. The cut-off energy of the protons is 2.5 MeV. The measurement shows that the contrast of the ARCTURUS laser including the plasma mirror system is good enough to preserve a foil with a thickness of 10 nm from destruction caused by the prepulse. Otherwise the acceleration process would not be possible.

The maximum proton energy for the shot depicted in figure 3.18 is 2.3 MeV. Several

ionisation stages are visible (C^{+}, C^{2+}, C^{3+}/O^{4+}, C^{4+}, C^{5+}, C^{6+}/O^{8+}). Their maximum energy does not exceed 0.5 MeV/nucleon.

3.3.5 SEQUOIA measurements with the plasma mirror

In order to prove the temporal contrast enhancement of the Düsseldorf plasma mirror system, a SEQUOIA measurement was set up. After the propagation through the PM, a part of the beam was coupled out through a 1 mm-thick fused silica window. The pulse duration of the initial laser pulse was optimised to 25 fs straight before the measurement by using the WIZZLER apparatus. First, a SEQUOIA trace of the intrinsic contrast of the laser pulse was recorded (see figure 3.19). The delay between two measuring points was 200 fs, and for each delay five shots were taken. The contrast ratio between -400 and -100 ps is 10^{-9}. The intensity increases up to $\sim 10^{-7}$ at -10 ps.

The measurement of the SEQUOIA trace with the plasma mirror is shown in blue in figure 3.19. Several additional difficulties have to be taken into account for this scan. The intensity on the substrate must be high enough to trigger the PM, but still low enough not to destroy

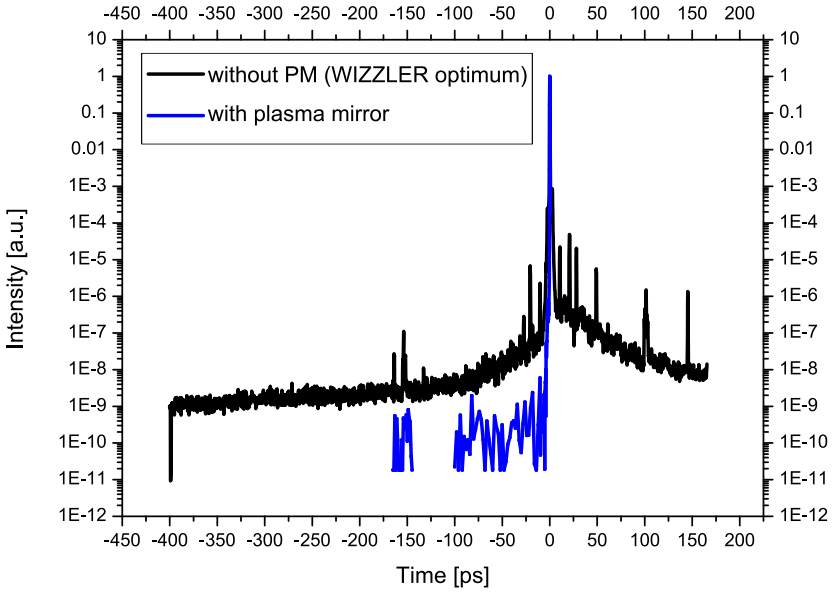

Figure 3.19: Temporal contrast of the ARCTURUS laser system with and without the plasma mirror. The black curve shows the contrast measurement taken with the optimum pulse duration measured using the WIZZLER device. The blue SEQUOIA curve shows the contrast measurement with the plasma mirror.

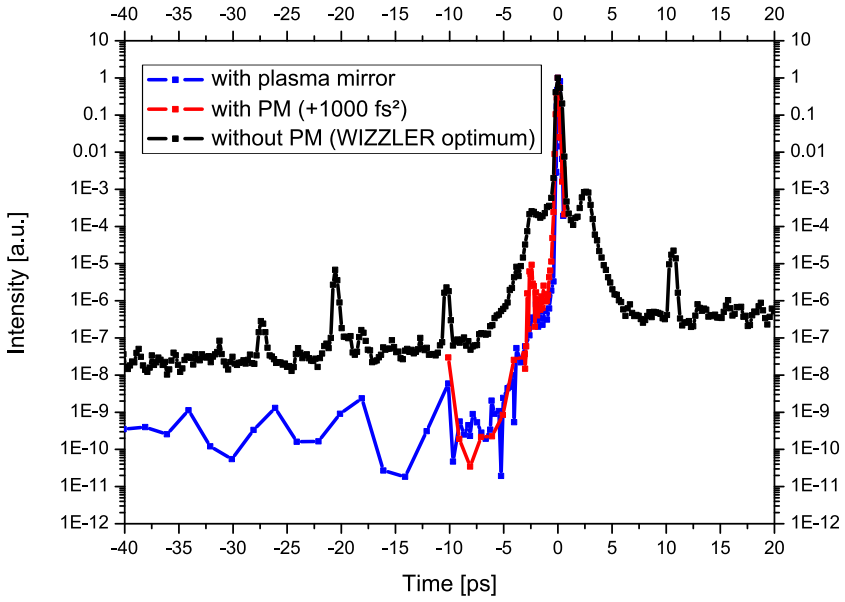

Figure 3.20: Contrast measurement of the plasma mirror system for a short pulse (blue curve) and chirped pulse ($D_2 = +1000\,fs^2$, red curve) compared to the contrast without PM at the shortest pulse duration (black curve).

the pulse shape fully via self-phase modulation inside the outcoupling window. Moreover, it has to be high enough to use the full dynamic range of the third-order autocorrelator. The contrast ratio between -400 and -160 ps exceeds the dynamic of the device and is therefore not shown. The PM substrate needs to be moved after each shot, thus the delay between two measuring points was larger: Between -163 and -143 ps, the delay time was 1 ps and between -100 and -10 ps, it was 2 ps. The main pulse was resolved in 400 fs steps (from -10 ps onwards). The measurement shows a drastic contrast enhancement up to three orders of magnitude. The signal reaches the dynamic limit of the device, so that it can be assumed that the temporal contrast which is achieved by using the PM is even better than the data of the measurement can show.

A closer look at the contrast situation shortly before the main pulse is shown in figure 3.20. The temporal contrast at -6.6 ps is improved from 1.2×10^{-7} to 1.9×10^{-10}. Also, the wings of the main pulse are strongly reduced. The plasma mirror triggers at -0.4 ps where the difference between the black and blue curve becomes negligible. The red curve in figure 3.20 depicts the contrast measurement for a chirped pulse ($D_2 = +1000\,fs^2$). In order to reach the same intensity on the PM, the substrate was moved towards the focus of P1. This contrast is similar to the previous measurement with the PM. Only at -2 ps, it is slightly degenerated.

3.3.6 MULTI-fs simulation of the prepulse conditions

MULTI-fs [146] is a hydrodynamic code for the simulation of the interaction of pico- and femtosecond lasers with matter, which is an extension of the MULTI code [147]. In contrast to the MULTI code which was designed for nanosecond pulses, steep density gradients of the target can be modeled by MULTI-fs. This is particularly important for intense high contrast laser pulses because for these, the target material is strongly heated before it expands. The simulation code is non-relativistic, hence only suitable to calculate the influence of the prepulse on the target.

Figure 3.21 shows the results of the ARCTURUS laser's prepulse interaction for two different contrast settings (the original target position is illustrated by the grey rectangle). The spatial distribution of the electron density n_e is shown. The initial plasma scale length of the preplasma right before the main pulse arrives at the target, is 1.5 µm. By applying a plasma mirror with an anti-reflective coated substrate, the plasma scale length can be decreased to 30 nm. Thus, the target properties like surface quality, surface structure etc. can be maintained prior to the interaction with the short, high intensity main pulse. This result is especially important for the feasibility of experiments with grating targets (see section 2.5.3).

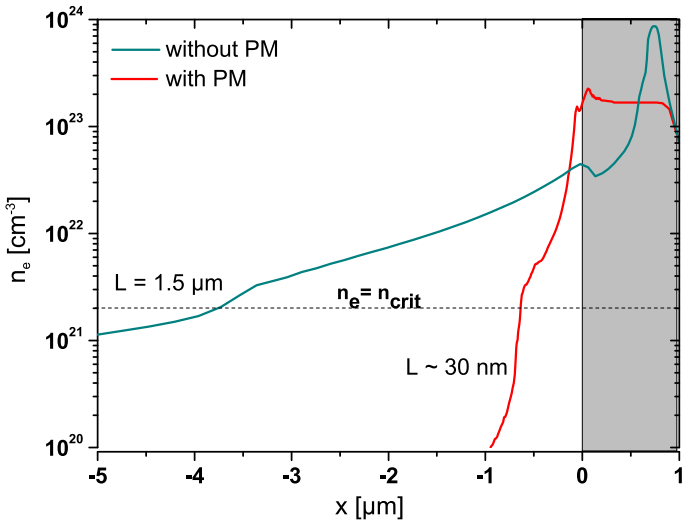

Figure 3.21: Results of the 1D hydrocode MULTI-fs simulation of the electron density prior to the arrival of the main pulse. The resulting plasma scale length for two different contrasts (with and without plasma mirror) is shown. The grey rectangle on the right-hand side depicts the initial position of the target before the interaction.

The plasma mirror system, which was designed and built by the author of this thesis, allows experiments with very high laser contrast. Another advantage is the accessibility of angles of incidence close to the target normal. Without a PM, the minimum incidence angle on the target for short focal length off-axis parabolic mirrors (i.e. f/2) is $\sim 25\,^{\circ}$. Otherwise, a significant amount of energy may be reflected back through the beam line into the laser amplifiers, where the energy possibly could be amplified and lead to severe damages of sensitive components like crystals or mirrors.

3.4 Setup of the FEMTOPOWER compact PRO laser system with hollow core fibre

A second laser system with different parameters was used in order also to investigate the intensity regime of $10^{16}\,\mathrm{W/cm^2}$ with a high laser contrast. This intensity regime is important for the generation of high harmonic radiation in gaseous targets. As previous measurements proved, the contrast ratio of the FEMTOPOWER laser is very high. At a time scale of 1 ps before the main pulse, the ratio is 10^5, and at 6 ps it is 10^8 [148, 149]. Intensive studies of the absorption in solid targets showed that the preplasma is negligible [150].

The FEMTOPOWER compact PRO[6] (setup shown in figure 3.22) also is a CPA based Ti:Sa laser system enabling very short pulse durations in combination with a high laser contrast. The oscillator is pumped by a frequency doubled Nd:YVO_4 laser. The output parameters of the oscillator are 10 fs, 75 MHz and 6 nJ. A Faraday isolator, which uses the rotation of the polarisation by the magneto-optic effect, is implemented to protect the oscillator from any back-reflections from the amplifier. The pulse is stretched to a duration of 10 ps by the propagation through a 5 cm long SF59 glass block to reduce nonlinear effects in the amplifier crystal.

This system uses, as the ARCTURUS laser system, an acousto-optical modulator (DAZZLER) for fine tuning of the dispersion and the generation of extremely short pulses. The nine-pass multipass amplifier is pumped by a Nd:YLF pump laser at 1 kHz; for this reason the repetition rate is decreased to 1 kHz after the fourth pass by a Pockels cell. A prism compressor reduces the pulse duration to 25 fs. The energy transmission of 85–90 % of the prism compressor is higher than for a comparable grating compressor. Due to the

6 Available from Femtolasers, Austria.

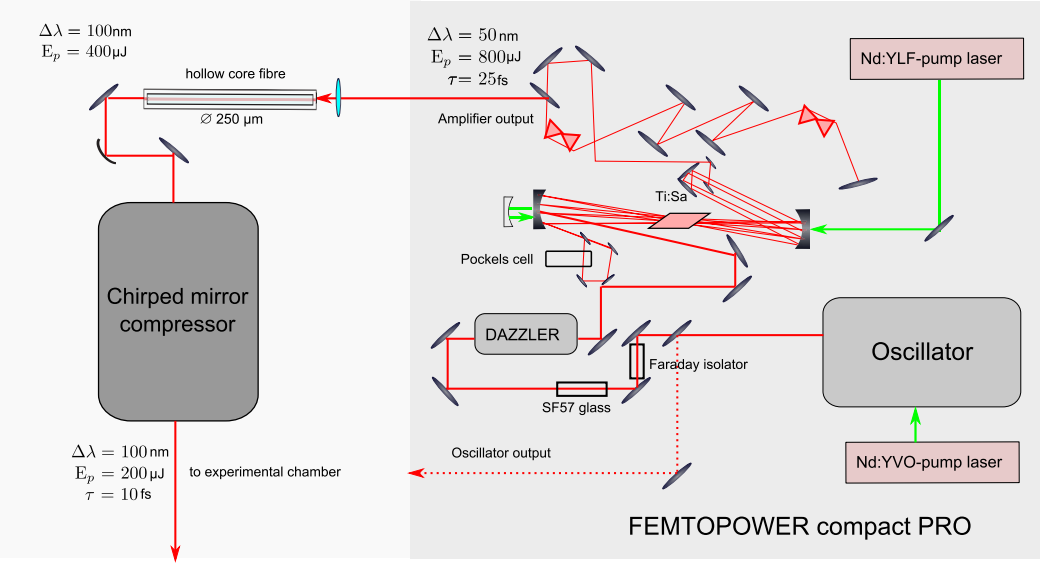

Figure 3.22: FEMTOPOWER compact PRO laser system in Düsseldorf. CPA system with hollow core fibre and chirped mirror compressor.

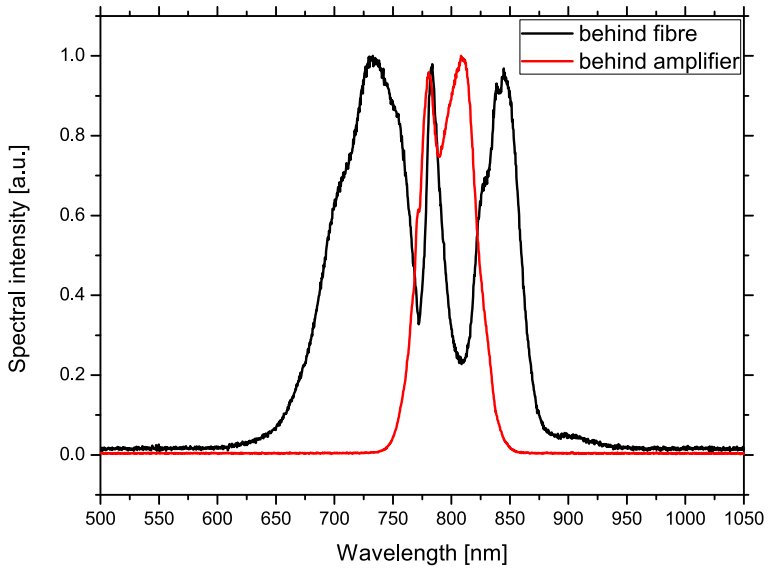

Figure 3.23: Spectra of the FEMTOPOWER compact PRO laser: Red curve was taken behind the FEMTOPOWER amplifier. The black line shows the spectrum after the propagation through the neon gas-filled hollow core fibre before the entrance of the compressor. The spectral broadening due to self-phase modulation is clearly visible.

gain-narrowing effect, the bandwidth $\Delta\lambda$ is diminished from $\sim 100\,\text{nm}$ to $\sim 50\,\text{nm}$. The output energy of the amplifier is $800\,\mu\text{J}$.

For the purpose of reaching pulse durations below 10 fs, the spectrum is broadened by self-phase modulation in a 1 m-long hollow core fibre filled with 1.8 bar of neon gas. Because of the fixed phase relations of the new generated spectral components to the existing ones, the pulses can be re-compressed temporally afterwards. The energy transmission of the fibre is $\sim 50\,\%$. Subsequently, the pulse duration is reduced by a chirped mirror compressor. Several reflections in the beam line lead to the final parameters in the experimental chamber with a pulse duration of 10 fs and a pulse energy of $200\,\mu\text{J}$ at a repetition rate of 1 kHz. Two output spectra from different stages of the laser system are depicted in figure 3.23.

4 Diagnostic methods and experimental setups

This chapter gives insights into the diagnostic methods used in the experiments that will be described in chapter 5 and 6. Furthermore, the experimental setups and devices are depicted. First, the SPIDER technique is introduced, followed by the characterisation of the gas nozzle target. Then the setup for the SPIDER measurements of the laser pulse propagation dynamics in noble gases is explained. The chapter ends with the experimental setup for the measurements of the harmonic generation from corrugated targets and the introduction of different spectrometers.

4.1 SPIDER technique

The properties of ultrashort laser pulses with pulse durations of 10 fs cannot be characterised by using photodiodes or other electronic devices. Self-referencing interferometry is a reliable method to measure ultrashort laser pulses. The principle of spectral interferometry is based on the superposition of at least two coherent incoming laser pulses. They are delayed in time by τ and afterwards superimposed and recorded by a spectrometer. In order to obtain the electric field of a laser pulse, the SPIDER technique (acronym of **S**pectral **P**hase **I**nterferometry for **D**irect **E**lectric **F**ield **R**econstruction) can be used. This self-referencing method was first described by Iaconis and Walmsley in 1998 [151, 152]. The SPIDER technique is based on shearing interferometry in the frequency domain.

The electric field of a laser pulse can be described as:

$$E(t) = |E(t)| \exp\left[i(\phi_t(t) + \phi_0 - \omega_0 t)\right] \tag{4.1}$$

where $|E(t)|$ is the envelope, ω_0 the carrier frequency, $\phi_t(t)$ the time-dependent phase and ϕ_0 the absolute phase.

The expression in the frequency domain is connected via a Fourier transformation of $E(t)$:

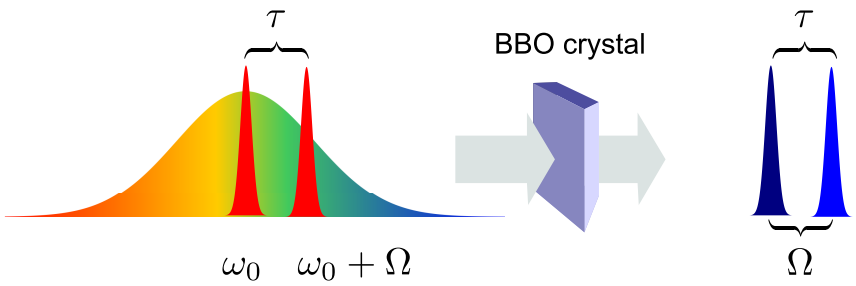

Figure 4.1: SPIDER principle; generation of the spectral shear: Two pulse replicas are overlapped with a chirped pulse in a BBO crystal. They are shifted in the time domain by τ. After the sum-frequency generation, they are spectrally differentiable by the shear Ω.

$$\tilde{E}(\omega) = \int_{-\infty}^{\infty} dt E(t) \exp[i\omega t] = \begin{Bmatrix} \tilde{\varepsilon}(\omega), & \omega > 0 \\ o, & \omega \leq 0 \end{Bmatrix} = \left|\tilde{E}(\omega)\right| \exp[i(\phi_\omega(\omega) + \phi_0)] \quad (4.2)$$

$\left|\tilde{E}(\omega)\right|^2$ is the spectral intensity which can be measured with a spectrometer, and $\phi_\omega(\omega)$ is the spectral phase.

The standard SPIDER technique makes use of three pulses, all originating from the test pulse. Two of them are replicas of the short pulse, obtained by separation in a beam splitting optical element. The third pulse is chirped by a stretcher module. Inside a crystal with a nonlinearity of the susceptibility tensor (i.e. BBO[1]), the short pulse replicas are superimposed with the chirped pulse (see figure 4.1). The sum-frequency generation in the crystal leads to the spectral shear of the two pulses as each of them is superimposed with a different part of the spectrum of the chirped pulse. The new frequencies of the pulses are [152]:

$$\omega_{1'} = \omega_0 + \omega_1 \qquad \omega_{2'} = \omega_0 + \omega_2 \quad (4.3)$$

Their spectral separation is given by the shear $\Omega = \omega_{1'} - \omega_{2'}$.

The resulting interferogram which is measurable by a spectrometer can be denoted as:

$$S(\omega) = |\tilde{E}(\omega)|^2 + |\tilde{E}(\omega+\Omega)|^2 + 2|\tilde{E}(\omega)\tilde{E}(\omega+\Omega)| \cos[\phi_\omega(\omega+\Omega) - \phi_\omega(\omega) + \omega\tau] \quad (4.4)$$

1 β-barium borate (β-BaB_2O_4).

The first two terms are the spectra of the test pulse and the frequency-sheared replica. In the last term, the spectral phase in form of the phase difference of both pulses is depicted. The linear phase term $\omega\tau$ can be subtracted. It is retrieved from the Michaelson interferogram which consists of the overlap of two replicas. In order to simplify the following formulas, θ is defined as:

$$\theta(\omega) = -\phi_\omega(\omega - \Omega) + \phi_\omega(\omega) \tag{4.5}$$

By adding up the phase differences in the following way, the spectral phase can be retrieved for discrete frequencies separated by the shear Ω [152]:

$$\phi_\omega(\omega_0 - 2\Omega) = -\theta(\omega_0 - \Omega) - \theta(\omega_0) \tag{4.6}$$
$$\phi_\omega(\omega_0 - \Omega) = -\theta(\omega_0) \tag{4.7}$$
$$\phi_\omega(\omega_0) = 0 \tag{4.8}$$
$$\phi_\omega(\omega_0 + \Omega) = \theta(\omega_0 + \Omega) \tag{4.9}$$
$$\phi_\omega(\omega_0 + 2\Omega) = \theta(\omega_0 + 2\Omega) + \theta(\omega_0 + \Omega) \tag{4.10}$$

For a very small shear value relative to the structures of the phase, the spectral phase can be obtained via integration:

$$\phi(\omega) \approx \frac{1}{\Omega} \int d\omega\theta(\omega) \tag{4.11}$$

The shear Ω should not be too small as otherwise, the spectral phase changes become unperceivable. Furthermore, Ω must be large enough to ensure that the phase sampling interval is larger than the Nyquist limit[2]. The phase $\phi(\omega)$ can be extracted by integration as long as $2\pi/\Omega$ is greater than the duration of the laser pulse.

4.1.1 Phase reconstruction from SPIDER interferograms

Figure 4.2 illustrates how the phase and finally the temporal evolution of a short laser pulse can be reconstructed. Part a) of the figure depicts the spectral interferogram taken by the SPIDER apparatus. After a Fourier transformation into the temporal domain, the resulting components at $+\tau$ are multiplied by a supergaussian filter function (part b)). The phase

2 Nyquist-Shannon sampling theorem for complete reconstruction of a bandwidth-limited signal. The sampling rate must be greater than $2f_{\max}$.

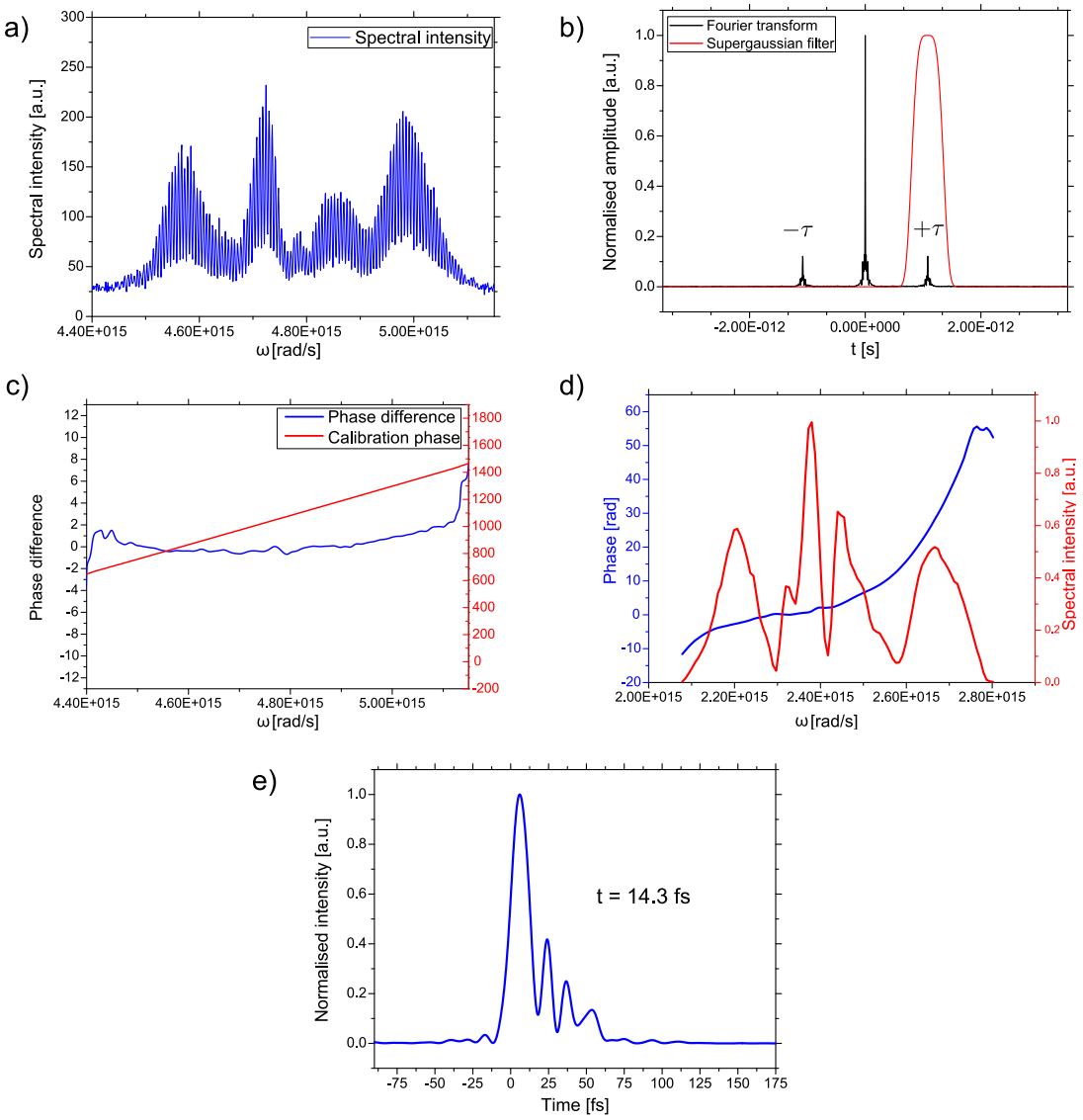

Figure 4.2: Evaluation of the spectral phase and reconstruction of the pulse duration:
a) SPIDER interferogram.
b) Fourier transform of the interferogram and filter function.
c) Phase difference retrieved after back-transformation and calibration phase ($\omega\tau$).
d) The red curve depicts the spectrum measured with Ocean Optics spectrometer. In blue, the phase obtained by summing up the phase differences is shown.
e) Retrieved pulse shape calculated from d).

difference can be obtained by an inverse Fourier transformation into the spectral domain (part c)). The $\omega\tau$-term, where τ denotes the delay between the two short pulses, can be subtracted. By adding up the phase differences in $\phi(\Omega+\omega)-\phi(\omega)$, the spectral phase is retrieved (part d)). The electric field is calculated by combining the phase and the intensity spectrum of the pulse. After a Fourier transformation into the time domain, the pulse shape can be obtained by taking the square of the absolute value (part e)).

An alternative method to characterise ultrashort laser pulses is the FROG technique. FROG is an acronym for **F**requency **R**esolved **O**ptical **G**ating and was developed by R. Trebino et al. [153]. The simplest version of an SHG-(Second-harmonic generation) FROG apparatus consists of the setup of an intensity autocorrelator including a beamsplitter, a delay stage and a crystal for second-order harmonic generation. Instead of an intensity detector, a spectrometer is used. By varying the delay, the FROG trace, which contains the pulse intensity and the optical frequency as a function of the time delay, can be retrieved. The electric field can only be obtained by an iterative retrieval algorithm, which is a distinct drawback of the FROG method in comparison to the SPIDER technique. Another advantage of SPIDER is the simplification of the measurements due to the lack of moveable components in the setup. However, different problems can occur using the SPIDER technique: The measurement of longer pulses is limited because of the non-availability of a suitable spectral shear. Another problematic issue can be spectra from lasers which have strong minima due to self-modulation. These gaps can impede the full reconstruction of the spectral phase.

4.2 Gas nozzle

In order to study the laser pulse propagation dynamics in different noble gases, a gas jet target was used. It was important for the measurements to keep good vacuum conditions. Therefore, a short, adjustable opening time was required. The nozzle, which was used for the generation of the gas jet, consists of a Parker Hannifin (series 9) valve with a fast response time and modified body head with a supersonic Mach 3.3 nozzle (see figure 4.3). The inner diameter of the nozzle head is 1 mm. A characterisation of a similar nozzle system can be found in [154] and [155].

The Mach number is defined by the velocity of the flow v in respect to the sound speed c_s:

$$M = \frac{v}{c_s} \tag{4.12}$$

If M is > 1, the flow is called supersonic. The maximum flow rate $\frac{dm}{dt}$ is limited by the

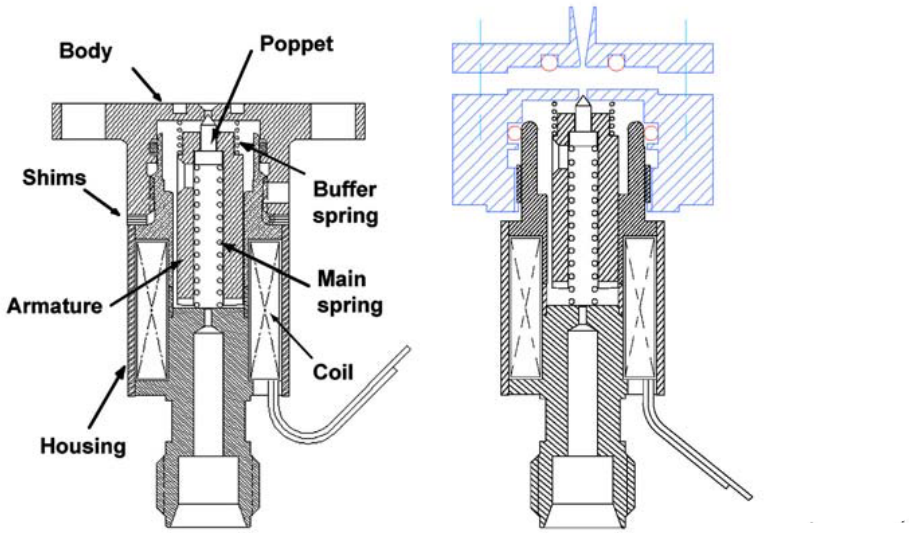

Figure 4.3: *Left-hand side*: Parker Hannifin series 9 valve; *right-hand side*: modified body head (image taken from [154]).

minimal cross section A^*:

$$\frac{dm}{dt} = \sqrt{\frac{k_a}{R_s}} \frac{p_0}{\sqrt{T_0}} \left(\frac{2}{k_a + 1} \right)^{\frac{k_a+1}{2(k_a-1)}} A^* \tag{4.13}$$

where k_a is the adiabatic constant (the ratio of the specific heats c_p/c_v), T_0 the temperature, p_0 the pressure and R_s the specific gas constant. In this case, the assumption of an ideal gas is valid, as only noble gases were used.

Figure 4.4 b) shows the density profile 600 µm above the nozzle, which was the position of the focal spot in the experiment. The profile of the gas jet (see figure 4.4 a)) was measured by a Normarski interferometer [156]. The interferograms were analysed using the IDEA software [157]. During the propagation of the laser pulse through the gas jet, the refractive index changes, thus the phase is shifted. After an Abel inversion of the resulting phase shift (figure 4.4 a)), the electron density can be calculated by applying:

$$n_e = n_{\text{crit}} \left(1 - \left(1 - \frac{\lambda}{2\pi} \xi \alpha(r) \right) \right) \tag{4.14}$$

where $\alpha(r)$ is the spatial phase obtained from the Abel inversion and ξ the geometrical magnification factor of the image.

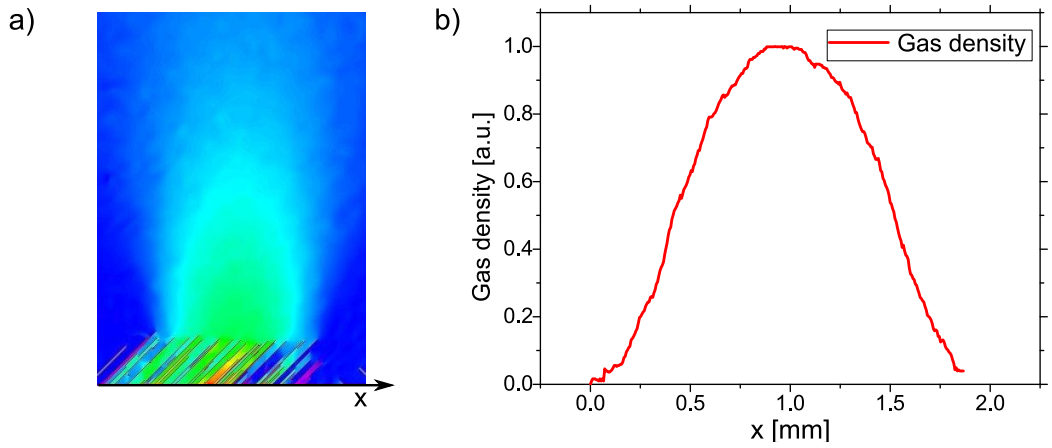

Figure 4.4: a) Phase profile of the Mach 3.3 gas jet, obtained with a Normarski interferometer. **b)** Gas density profile 600 µm above the gas nozzle (normalised).

Considering the characteristics of the gas nozzle system, it is suitable for studying the ionisation of noble gases since it has a fast response time and a reproducible gas density profile.

4.3 Experimental setup: SPIDER measurements after the laser pulse propagation through gaseous targets

The influence of the gas pressure on the spectral phase of the laser after the propagation through underdense targets and the corresponding ionisation dynamics were investigated applying the following setup (see figure 4.5). The beam of the FEMTOPOWER Compact PRO laser was focused by an f/3 off-axis parabolic mirror with an effective focal length of 89 mm above the gas nozzle. The size of the focal spot was 4.3 µm (FWHM) (figure 4.6). In order to generate a reproducible gas density profile, a Mach 3.3 Parker series nozzle with 1 mm diameter was used (see section 4.2). The position of the laser focus was set 600 µm above the gas nozzle. After the propagation through the gas, the laser beam was re-collimated by an achromatic lens with 30 mm focal length. The central part of the beam left the chamber through a 1 mm-thick fused silica window with 10 mm diameter. Outside the chamber, a periscope directed the beam onto the table with the SPIDER apparatus. The main part was used for the SPIDER measurement, whereas a small section was coupled into an Ocean Optics spectrometer in order to measure the spectrum simultaneously to the SPIDER interferogram.

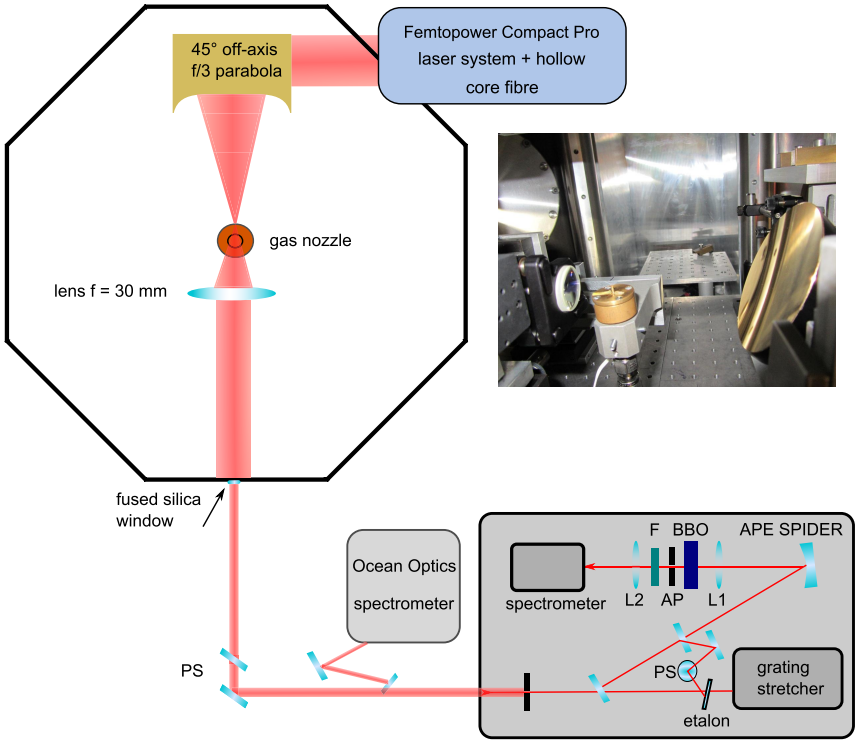

Figure 4.5: Setup of the SPIDER measurements to study the laser pulse propagation dynamics in gaseous targets. The inserted picture illustrates the off-axis parabolic mirror and the gas nozzle in the target chamber. The input parameters using the FEMTOPOWER Compact PRO laser system were: 10 fs pulse duration and 200 µJ pulse energy.

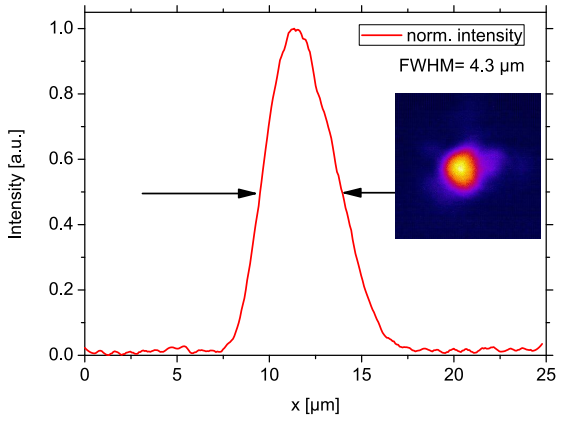

Figure 4.6: Focal spot of the laser beam obtained with an f/3 off-axis parabolic mirror with an effective focal length of 89 mm.

The pulse energy inside the chamber was 200 µJ, which corresponds to a peak intensity of $6.8 \cdot 10^{16}$ W/cm^2 in the focus of the off-axis parabolic mirror. The pulse duration was ∼10 fs. Three different types of noble gases (helium, neon and argon) were used to study the laser pulse propagation dynamics during the ionisation for several atomic numbers.

Inside the SPIDER apparatus[3], the incoming laser pulse is split up into two replicas by an etalon. A third pulse is stretched to a pulse duration of several picoseconds by a grating stretcher. Both short pulses are separated temporally in order to obtain an interference pattern with different parts of the spectrum of the long pulse inside the BBO crystal (see section 4.1). The products of the sum-frequency generation are frequency-shifted by the shear $\Omega = \frac{\tau}{D_2}$ [158]. The temporal delay between the two short pulses can be obtained from the Michaelson interferogram by measuring the fringe distance $\tau = 2\pi/\delta\omega$. For the APE SPIDER, τ is around 1.078 ps. Small variations due to possible deviations in the alignment have to be checked every day. The spectral shear, which results from the stretching factor of the long pulse, is $\Omega = 7.54 \cdot 10^{12}$ rad/s (stretcher module C).

In order to reduce the noise level after averaging over the number of shots, 30 SPIDER interferograms for each gas pressure were taken under the exact same conditions. The experimental results are presented in chapter 5.

4.4 Experimental setup: Harmonics from corrugated targets

In the experiment described in this section, the p-polarised ARCTURUS laser was focused onto the target with a focal diameter of 2.1 µm (FWHM) by an f/2 off-axis parabolic mirror in the solid target chamber (see figure 4.7 and 4.8). This corresponds to an intensity regime of $\sim 10^{20}$ W/cm^2. The pulse duration was 27 fs. The temporal contrast of the ARCTURUS laser was enhanced to its optimum by inserting a saturable absorber into the booster amplifier and applying anti-reflective coated targets in the plasma mirror system. The settings ensure perfect contrast conditions for a minimal preplasma before the interaction of main pulse and target takes place. Moreover, the usage of the plasma mirror averts back-reflections from the target into the beam line at incidence angles close to the target normal and preserves the structure of the grating targets prior to the main pulse interaction. The targets, which were used for the harmonic generation, had a sinusoidal profile and were characterised by atomic force microscopy (see section 6.3).

Two incidence angles on the target were investigated with two different spectrometers.

3 1.53 SPIDER apparatus from APE Angewandte Physik und Elektronik GmbH, Berlin.

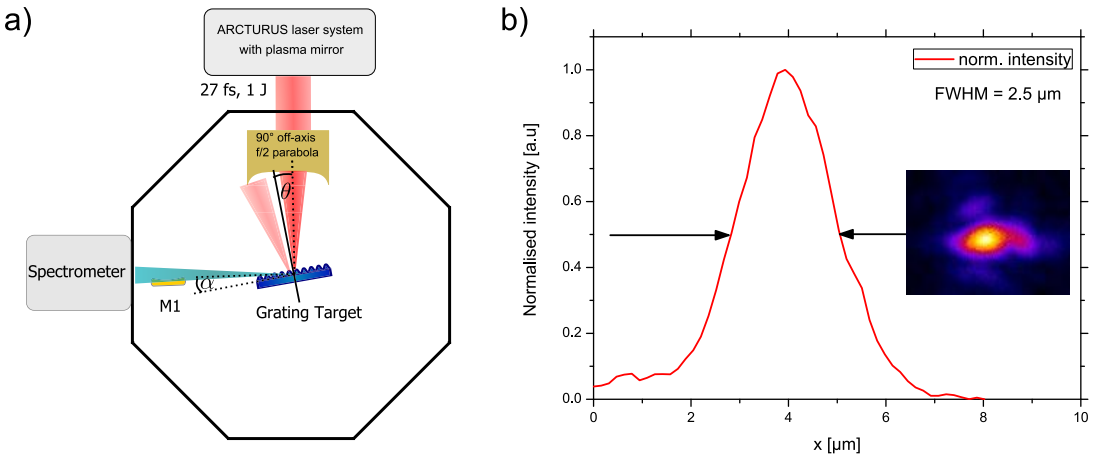

Figure 4.7: a) Experimental setup in the target chamber: High harmonics from grating targets (XUV range)
b) Focal spot of the ARCTURUS laser obtained with an f/2 off-axis parabolic mirror in the solid target chamber 2.

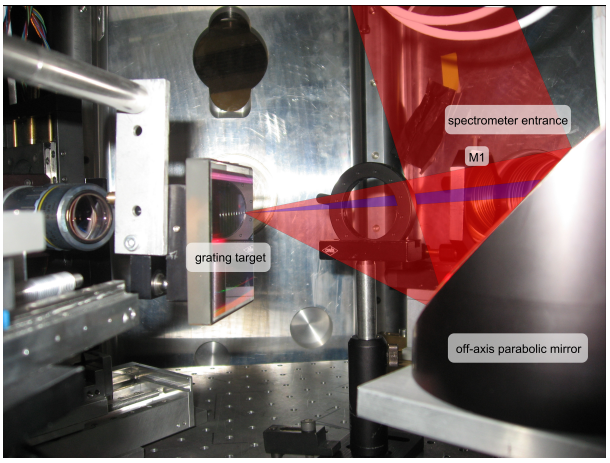

Figure 4.8: Photo of the setup in the target chamber. The incoming laser beam is marked in red colour. It is focused onto the grating target. The harmonic signal, which passes through an aperture into the spectrometer entrance, is depicted in blue.

To measure the harmonic emission in the XUV range, a flat-field grating spectrometer (see section 4.5.1) was used. The angle of incidence on the target was close to the target normal with 5 °, which is far away from the well-established incidence angle of 45 ° for the generation of harmonic radiation from flat targets [11, 10]. The XUV spectrometer was placed 5 ° with respect to the target surface (see figure 4.9). The accessible spectral range was 16–35 nm.

The purpose of the second configuration of spectrometer and incidence angle was the investigation of the low-order harmonics (2^{nd} and 3^{rd}). In this case, the McPherson UV spectrometer (see section 4.5.2) was placed 25 ° with respect to the target surface. The angle of incidence was 25 ° from the target normal.

4.5 Spectrometers

4.5.1 Flat-field XUV spectrometer

The XUV radiation generated by the laser pulse interaction with corrugated targets, was recorded by a flat-field grazing incidence spectrometer (figure 4.9). Two gold-coated spherical mirrors with a diameter of 50.8 mm were aligned in a modified Kirkpatrick-Baez arrangement [159] in order to collect the XUV signal. The first mirror (M1) with a radius of curvature of 7 m, was set at grazing incidence of 2.2 °. It focused the light in a line focus onto the entrance slit of the spectrometer. Mirror M2 (radius of curvature 10 m, grazing incidence angle 2.6 °) imaged the plasma onto the CCD camera plane. The acceptance solid angle was calculated to be 0.04 msr. Behind the collection mirror system, an aluminium filter was placed to block any remaining laser light. For dispersing the radiation spectrally, a concave Hitachi grating of variable line-spacing was used (nominal spacing: 1200 lines/mm) at a

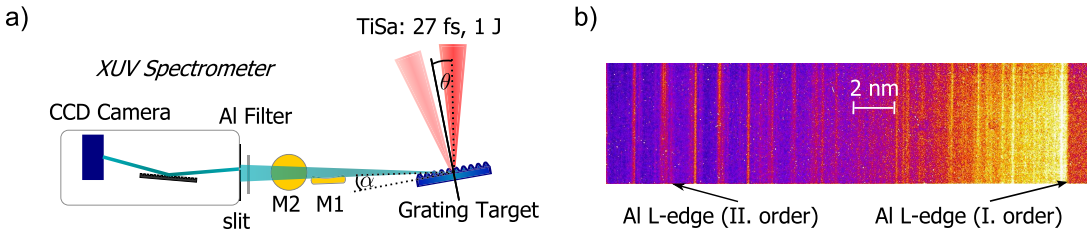

Figure 4.9: a) Setup of the grating harmonics experiment with XUV spectrometer at 5° angle of incidence.
b) Raw spectrum obtained with the XUV spectrometer.

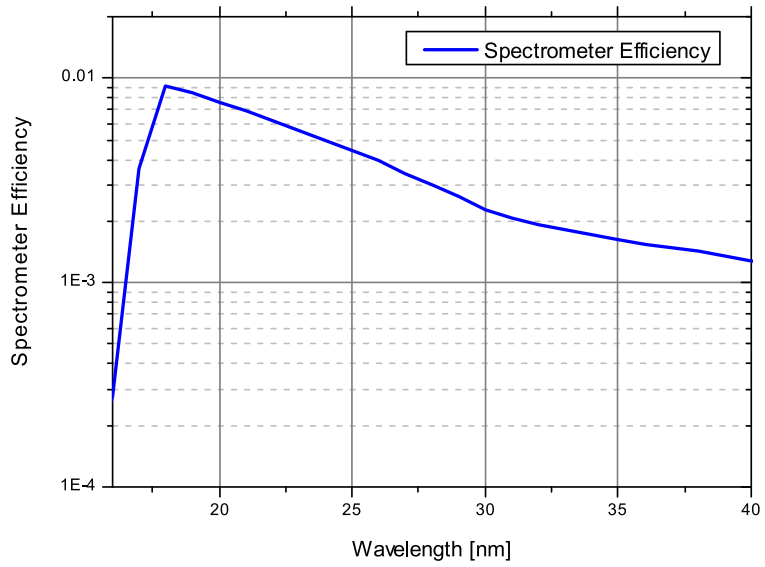

Figure 4.10: Spectral efficiency of the XUV spectrometer for the investigated wavelength range. This curve takes into account the quantum efficiency of the CCD camera, the reflectivity of the gold mirrors at grazing incidence, the transmission of the aluminium filter and the efficiency of the Hitachi grating.

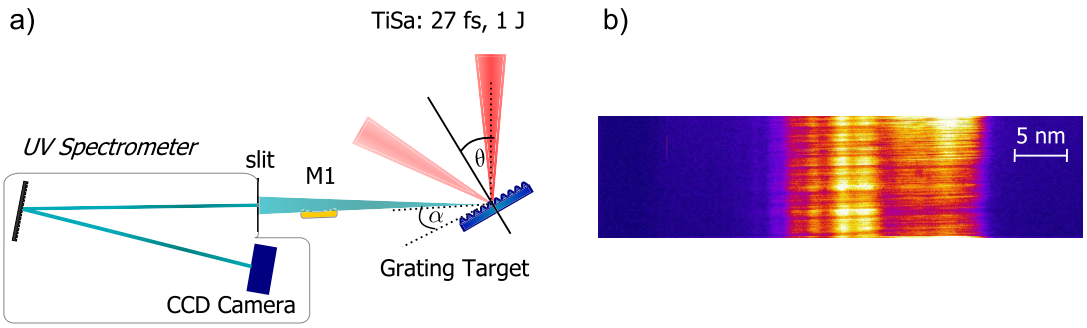

Figure 4.11: a) Setup of the grating harmonics experiment with UV spectrometer at 25° angle of incidence.
b) Raw spectrum of the second-order harmonic obtained with the UV spectrometer.

grazing incidence angle of 3 °. The nominal dispersion of the Hitachi grating is 0.6 nm/mm [160]. An Andor CCD camera (DO420-BN) with a chip size of 6.35 × 25.4 mm detected the spectra. The spectral efficiency of the spectrometer setup for the investigated spectral range was around 0.9 % for 18 nm and decreased to 0.17 % for 34 nm. The spectral efficiency curve of this spectrometer is shown in figure 4.10.

4.5.2 UV spectrometer

The lower-order harmonics of the laser were detected by using a monochromator McPherson (type 225) spectrometer (see figure 4.11). One spherical mirror of diameter 76.2 mm and a radius of curvature of 8 m imaged the plasma source vertically onto the entrance slit of the spectrometer. The spherical grating with 600 lines/mm and a focal length of 1 m dispersed the spectra onto the Andor CCD camera (same as used for the XUV spectrometer) with a deviation of 15 ° between the entrance slit and the dispersion plane. The linear dispersion of the grating on the CCD camera plane was 1.66 nm/mm. The motorised holder of the grating allows a rotation of the grating around the horizontal axis. Thus, a broad wavelength range (250–600 nm) was accessible in this experiment covering the low harmonic orders (2^{nd} and 3^{rd}) of the fundamental frequency.

5 Propagation dynamics of ultrashort laser pulses in noble gases

The interaction of ultrashort laser pulses with gaseous targets and the proceeding ionisation process during the propagation of the laser pulse play an important role in the generation of high harmonic radiation in underdense targets. This chapter gives insights into the influence of ionisation on the laser pulse propagation in three different noble gases (helium, neon and argon). Measurements using the SPIDER technique in order to evaluate the spectral phase after the interaction with the gas jets are shown. Moreover, numerical investigations of the spectral and temporal characteristics of the laser pulse during the propagation through gaseous targets are presented.

5.1 Introduction

The influence of the gas pressure on the initial laser pulse was studied in [161]. The evaluated dispersion contribution of the gaseous medium indicates that negative as well as positive dispersion can be the consequence of the laser pulse interaction with a gas jet. Interest in this subject arises from the fundamental understanding of the influence of the ionisation dynamics on properties of the laser pulse, which is important for the generation of high harmonic radiation from gaseous targets for example.

Self-focusing in high-density gas jets was investigated in [162]. One of the applications of optical-field ionisation-induced spectral broadening in noble gases is the compression of high energy laser pulses [163]. Nowadays, the generation of isolated attosecond pulses is possible by applying carrier envelope phase (CEP) stabilised few-cycle laser pulses [164]. Nevertheless, the rather low conversion efficiency of the harmonics from gaseous targets remains a problem. Other opportunities are more complicated techniques that make use of transient phase matching [165] or increase the pulse energy by optical parametric amplification [166, 167]. Further ideas to shorten the laser pulse are the propagation through hollow core capillaries [84] or self-guiding filaments [82, 87].

In [168], a numerical study of the influence of the gas pressure on the laser pulse propagation in argon gas cells is described. By applying an extended version of the **N**on**l**inear **S**chrödinger **E**quation (NLSE), different pressure regimes were identified. For a weakly focused ($w_0 = 200\,\mu m$) laser pulse with a pulse duration of 200 fs and a peak intensity of $10^9\,W/cm^2$, the low pressure regime (10^{-3} atm to 1 atm) is dominated by plasma-induced defocusing, tunneling ionisation and blue-shifting. At higher pressures (1 atm to 10 atm), self-focusing gains influence. Over 10 atm, the impact of normal group velocity dispersion and multiphoton ionisation becomes significant. The experiment which is described in this chapter, addresses a new interaction regime with an ultrashort (∼10 fs) and strongly focused ($w_0 = 4.3\,\mu m$) laser pulse.

5.2 Ionisation-induced blue-shift

The spectra of the laser after the propagation through the gas jet were measured with an Ocean Optics spectrometer[1]. All the spectra that were recorded after the interaction with the gas jet show a significant blue-shift (figure 5.1). The reference shots, measured prior to the gas jet interaction, are depicted in black. For the helium gas jet, the spectra indicate an increasing blue-shift with rising gas pressure. Moreover, a noticeable red-shift occurs at 7 bar backing pressure (plot a)). On the right-hand side plots of figure 5.1 (b), d), f)), the reference was subtracted from the spectra. Especially spectral components around 850 nm are shifted towards lower wavelengths.

By applying a neon gas jet (figure 5.1 (c) and d)), the spectral shift looks similar compared to the helium spectra. The intensity in the lower wavelength part of the spectrum rises, whereas the components around 850 nm vanish. The red-shift which is significantly smaller than for helium, becomes visible at 880 nm.

In case of the laser pulse propagation through the argon gas jet (part e) and f)), the strongest blue-shift was observed. The width of the spectra increased significantly. Signals down to 610 nm were detected with the spectrometer. The red part of the reference spectrum completely disappeared for backing pressures above 7 bars. The stronger blue-shift is induced by the low ionisation potential of argon. Hence, the ionisation process takes place more rapidly. A prominent periodical structure appears.

For all three gases, the blue-shift is the consequence of the irreversible ionisation process on the time scale of the laser pulse. No recombination of electrons and ions can take place

1 Type: USB2000+.

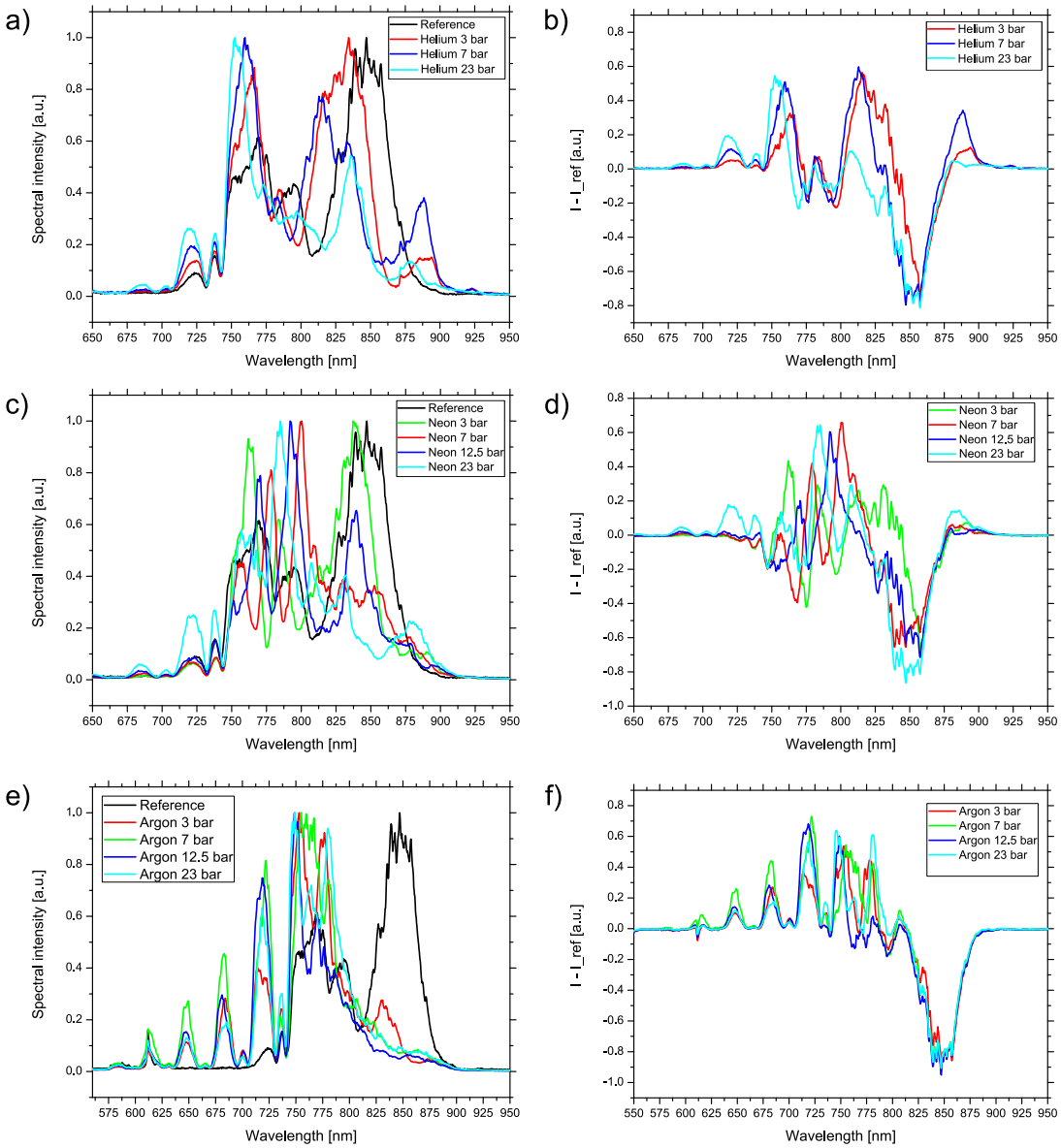

Figure 5.1: Blue-shifted spectra for different gas pressures after the laser pulse interaction with the gas jet target for helium (**a)**), neon (**c)**) and argon (**e)**) compared to the reference spectrum (black line) which was measured without gas. The change of the spectral intensity for helium (**b)**), neon (**d)**) and argon (**f)**) is shown on the right-hand side plots.

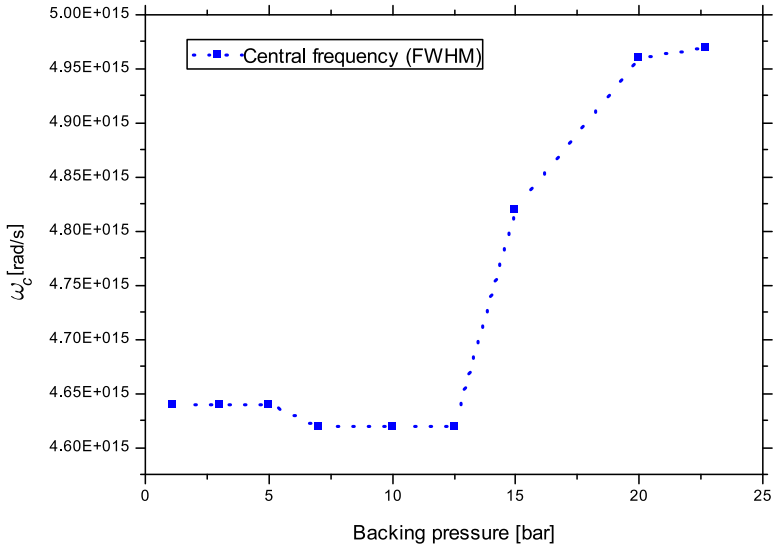

Figure 5.2: Change of the central frequency (at the FWHM of the spectra) by increasing the gas pressure in helium.

during the short duration of the laser pulse. It should be stated that due to the blue-shift, the central frequency of the laser spectrum also changes. The frequency at the FWHM of the spectra after the interaction with the helium gas jet is illustrated in figure 5.2. In this case, the central frequency is stable in the low pressure regime. However, by increasing the backing pressure over 12.5 bar, the frequency rises abruptly.

5.3 SPIDER measurements

The evaluation of the SPIDER data is described in the following paragraph. In order to obtain an optimal signal-to-noise ratio, 30 interferograms were superimposed. Since an increase of the gas pressure causes a strong blue-shift, the central frequency changes during the pressure scan. The spectral phase was retrieved for each central frequency by a programme that follows the steps which are explained in section 4.1.1. The change of the central frequency also changes the second-order dispersion (D_2 coefficient). This was taken into account for the evaluation of the phase. Afterwards, the phase difference was fitted by using a Taylor expansion (see equation 2.32).

The pressure dependency of the D_2 coefficient was obtained by recording a reference interferogram without any gas in the experimental chamber. The D_2 coefficient was

calculated after subtracting the reference phase from the phase which included the gas jet interaction.

5.3.1 Results for helium gas

Three interferograms after the interaction with helium gas are shown in figure 5.3 b)–d). Plot a) of the figure illustrates the reference interferogram which was recorded prior to the helium measurements. A low pressure of 1.1 bar already leads to a blue-shift (plot b)). When the pressure becomes higher, more modulations in the spectral envelope of the interferogram appear (plot d)). Figure 5.4 depicts the phase which was retrieved from the interferograms. The reference phase (without gas) was subtracted. The phase differences can be divided into two regimes. In the lower pressure cases (part a)), the phase differences are negative for lower frequencies and become positive for frequencies above $\sim 4.62\times10^{15}$ rad/s. Part b) of figure 5.4 shows the phase shift for high pressures. The phase shifts are positive in case of low frequencies and become negative for frequencies higher than ~ 4.85 rad/s. Moreover, it can be seen that the highest pressure leads to the strongest phase shift.

Figure 5.5 illustrates the gas pressure dependency of the D_2 coefficient. In the low pressure regime, the D_2 value is negative. Starting with -55 fs^2 at 1.1 bar, D_2 drops to -117 fs^2 at 10 bar. By a further increase of the pressure, it rises up to the maximum value of +238 fs^2 (at 20 bar) before dropping again to 172 fs^2 (at 22.7 bar). A dotted line connects the points for visualising purposes. The depicted error bars result from the error of the Taylor expansion fit of the phase.

The results for the D_2 coefficient on five different days are illustrated in figure 5.6. It is apparent that the absolute value of the D_2 fluctuates from day to day. The reasons for this fluctuation lie in the laser pulse generation itself: The laser pulse of the FEMTOPOWER compact PRO laser system is sent through a hollow core fibre filled with neon gas in order to obtain a broad spectrum which allows a pulse compression down to 10 fs (see section 3.4). Once the gas inside the hollow core fibre is replaced, it starts to degenerate due to the interaction with the laser pulse and small leakages of the vacuum compartment. This has an influence on the spectrum of the broadened laser pulse, hence the initial chirp of the laser pulses changes.

A second reason for possible fluctuations is the radial profile of the laser beam. Since the intensity is higher on the propagation axis, the central part of the laser beam experiences a higher electron density than the outer parts. The SPIDER apparatus can only measure a small fraction of the beam which is not necessarily the same fraction on each day.

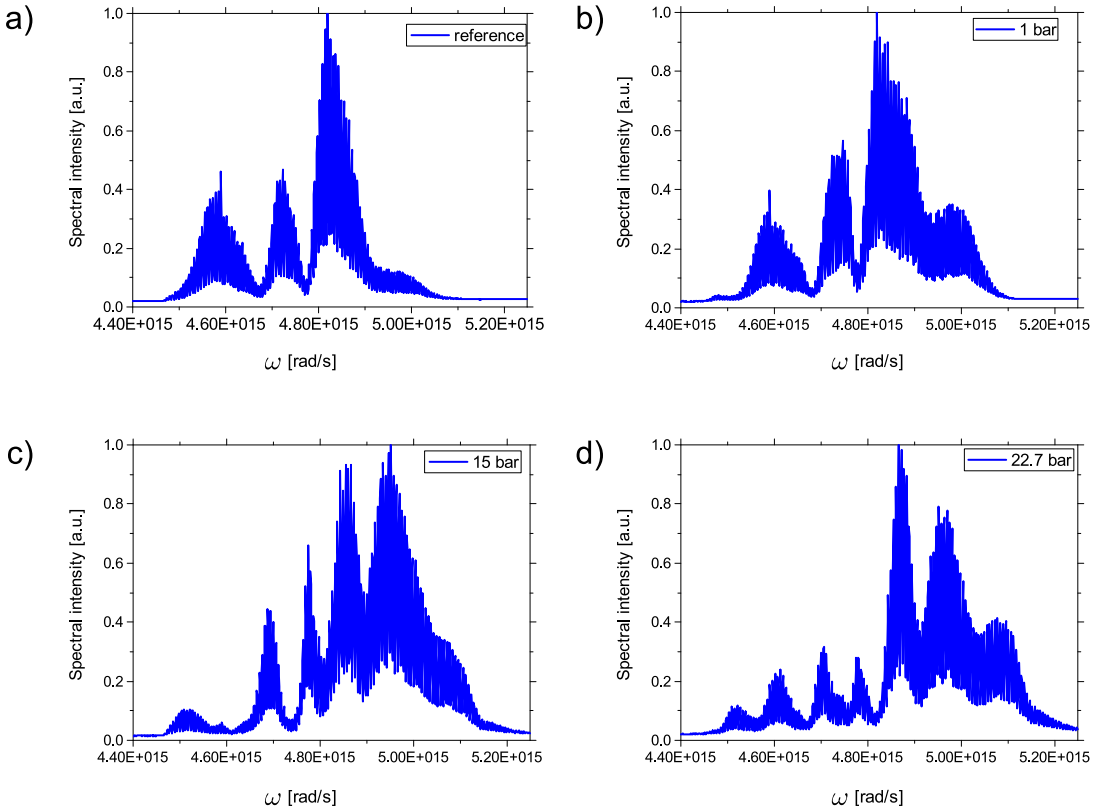

Figure 5.3: SPIDER interferograms measured for different gas (backing) pressures after the laser pulse interaction with the helium gas jet (**b)-d)**) and reference interferogram (**a)**).

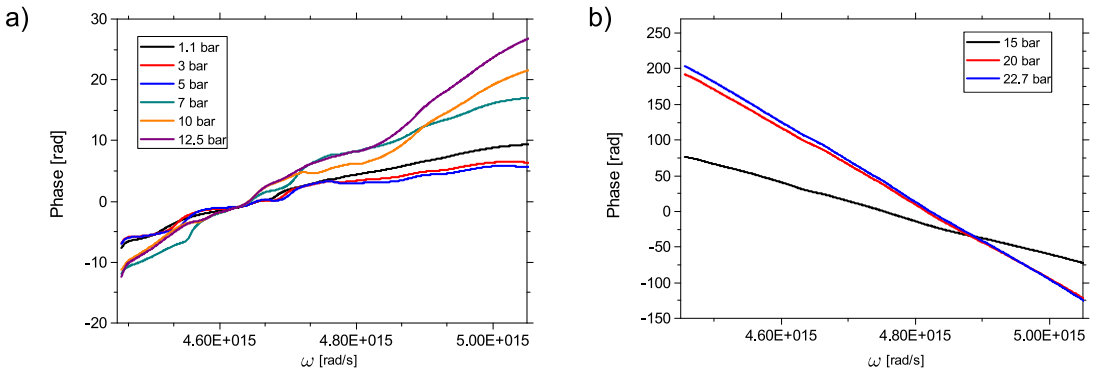

Figure 5.4: Spectral phase measured after the laser pulse interaction with the helium gas jet. The reference phase was subtracted.
a) Low pressure regime (1.1–12.5 bar backing pressure).
b) High pressure regime (15–22.7 bar backing pressure).

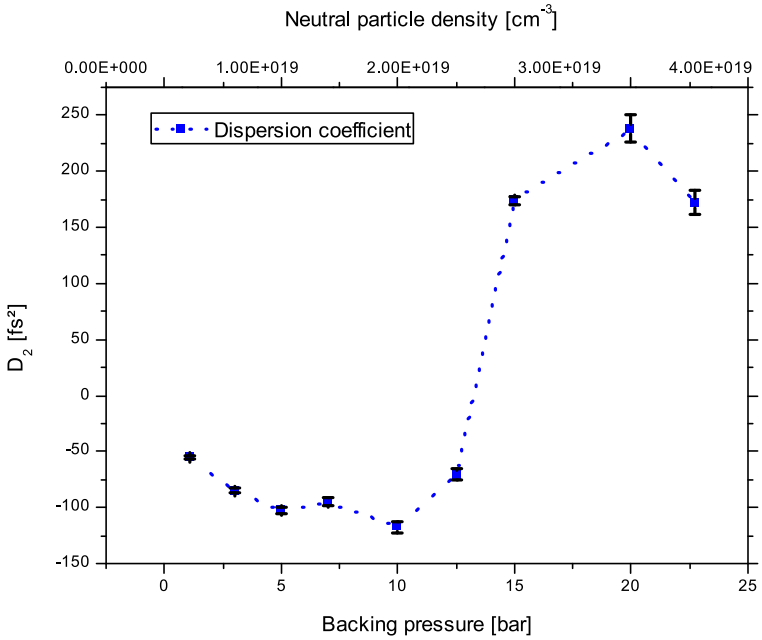

Figure 5.5: Influence of the gas jet pressure on the D_2 coefficient for the helium gas jet. The error bars denote the error of the Taylor expansion fit.

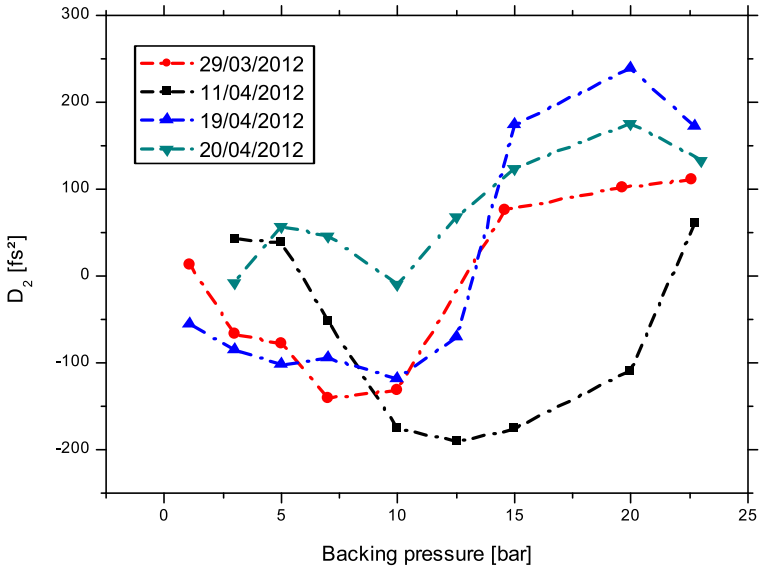

Figure 5.6: Influence of the gas jet pressure on the D_2 coefficient on different days. On the 11th of April, the neon gas inside the hollow core fibre was replaced.

Nevertheless, the tendency of a negative D_2 value for low pressures rising to positive values at higher pressures occurs on all days.

Interpretation of the interaction with the helium gas jet

According to the BSI theory[2], the laser intensity which was used in this experiment, is sufficient to ionise helium up to the second ionisation stage before the intensity maximum of the laser pulse is reached. As a consequence of the progressing ionisation during the interaction with the laser pulse, the electron density rises. This effect is especially present on the axis of the laser pulse, hence defocusing due to the change of the refractive index occurs. Defocusing of the laser pulse becomes more important with increasing pressure. The counteracting process is self-focusing which is also strongly intensity-dependent and thus has its maximum influence on the propagation axis as well. Moreover, spectral broadening due to the influence of self-phase modulation is apparent in the interferograms (figure 5.3) and spectra (figure 5.1).

The ionisation process leads to a time-dependent refractive index. Hence, different parts of the laser experience different phase shifts. The refraction index is proportional to the density of free electrons.

Analysis of measurement errors and evaluation dependencies

The exact measurement of the spectral phase is limited by several fluctuations which cannot be suppressed. First, the initial laser pulse itself is not completely stable during the day. This was analysed by taking reference interferograms at both the beginning and end of one measurement day. The reference phase changes due to slight fluctuations caused by the necessary focusing of the amplified laser beam into the hollow core fibre. A reason for possible misalignments are thermal changes in the laser area.

Another circumstance influences the spectral phase measurement: The initial chirp of the laser pulse varies from day to day as the spectral phase is not regularly flattened by a DAZZLER adjustment. Hence, when the neon gas inside the hollow core fibre becomes "older" and degenerates, it is not guaranteed that the pulse duration reaches its possible minimum which is around 8 fs.

Additionally, due to the fluctuations of the energy of the pump laser(s), the output energy

2 A list of the ionisation thresholds can be found in appendix A.

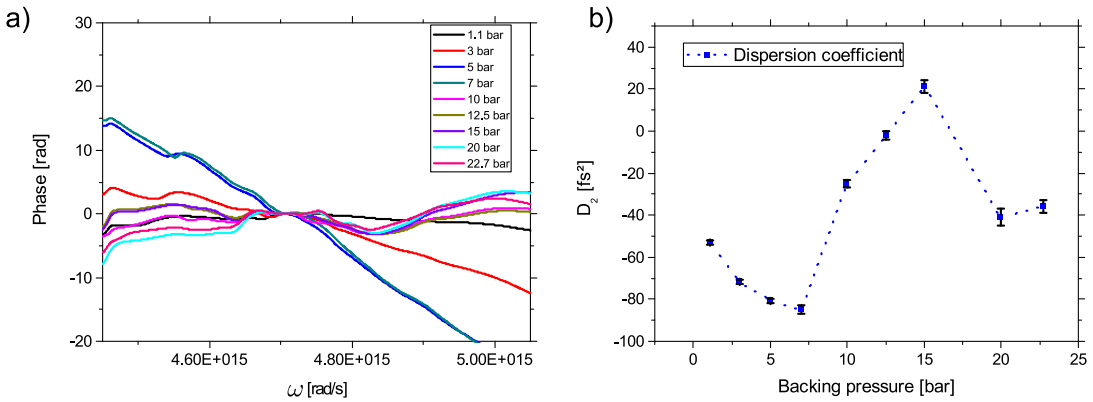

Figure 5.7: Evaluation for a fixed central frequency ω_c:
a) Spectral phase after the interaction with the helium gas jet for different backing pressures. The reference phase was subtracted.
b) D_2 coefficient for different backing pressures. The depicted error bars result from the error of the Taylor expansion fit of the phase.

may vary during the day and consequently changes the intensity in the focal spot in the target chamber. Nevertheless, the shot-to-shot difference of the spectral intensity of the interferograms was less than 5 %.

Furthermore, it has to be stated that the evaluation method influences the absolute values of the D_2 coefficient as well. Figure 5.7 illustrates the results for the phase shift and the D_2 coefficient for an evaluation method where the central frequency ω_c is kept constant at the central frequency of the initial laser pulse[3]. It is visible that the tendency of the D_2 coefficient curve stays the same. It starts with negative values (-55 fs^2) at 1.1 bar, drops down to -85 fs^2 at 7 bar and rises to a maximum of 20 fs^2 at 15 bar. At higher pressures, the D_2 coefficient drops again to negative values (-40 fs at 20 bar). The shape of the resulting D_2 curve is very similar to the previously shown graph in figure 5.5. Nevertheless, in the higher pressure regime above 15 bar backing pressure where the spectral blue-shift becomes significant (see also figure 5.2), the sign of the coefficient is different.

5.3.2 Results for neon gas

The interaction with the neon gas jet was studied for backing pressures of 3–23.5 bar. The resulting interferograms can be found in figure 5.8. Already the lower pressures lead to a

3 $\lambda_c = 800$ nm.

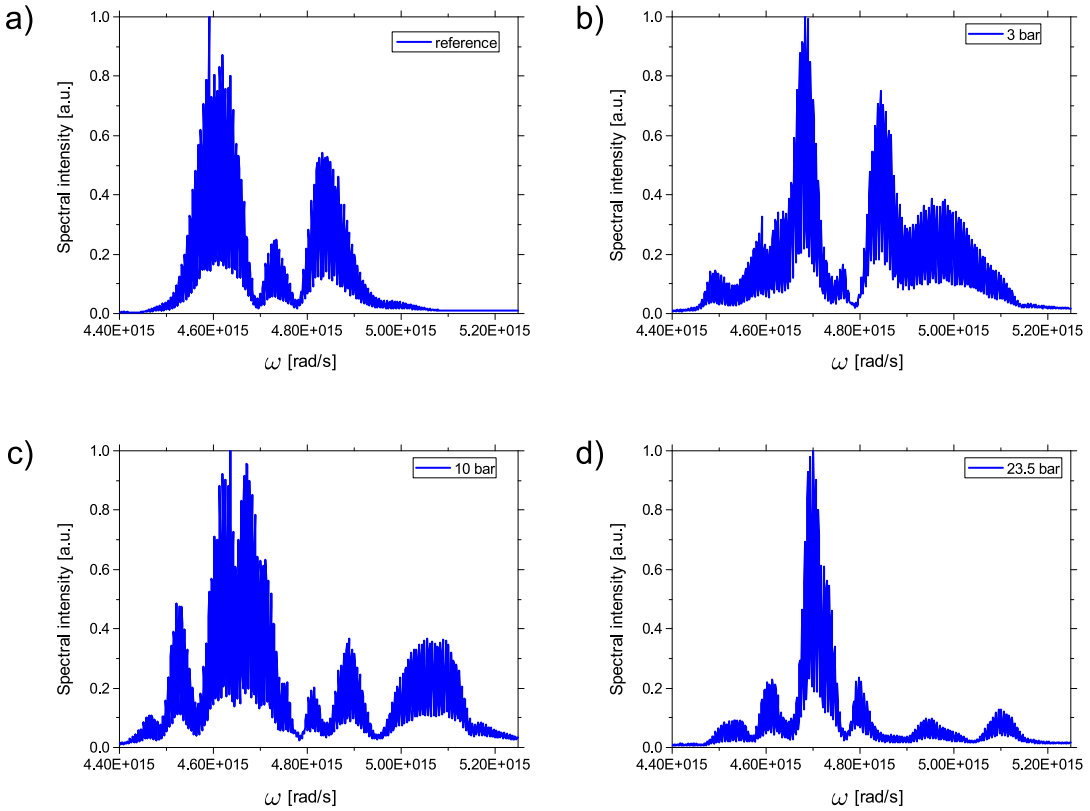

Figure 5.8: SPIDER interferograms measured for different gas (backing) pressures after the laser pulse interaction with the neon gas jet (**b)-d)**) and reference interferogram (**a)**).

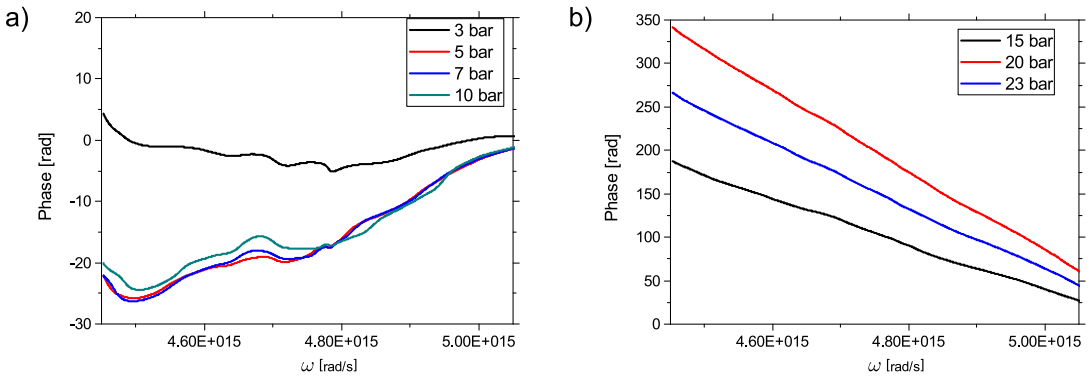

Figure 5.9: Spectral phase measured after the laser pulse interaction with the neon gas jet. The reference phase was subtracted.
a) Low pressure regime (3–10 bar backing pressure).
b) High pressure regime (15–23 bar backing pressure).

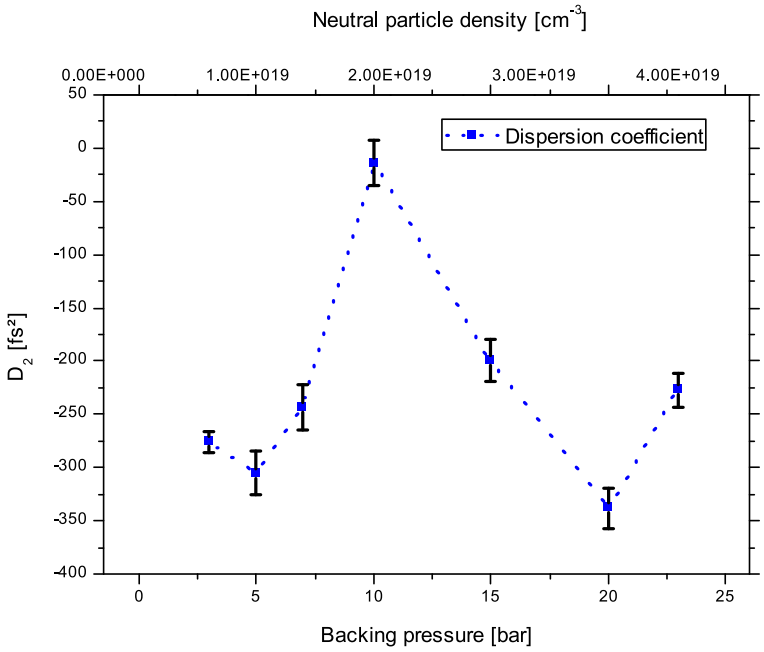

Figure 5.10: Influence of the gas jet pressure on the D_2 coefficient for the neon gas jet. The error bars denote the error of the Taylor expansion fit.

strong blue-shift and spectral broadening of the interferogram. More modulations appear in the intermediate pressure regime (10 bar). At the highest pressure, a strong peak at 4.7×10^{15} rad/s dominates the interferogram.

The phase changes due to the neon gas interaction with the laser pulse are shown in figure 5.9. The phase shift is very small in case of a backing pressure of 3 bar. In the intermediate pressure regime between 5 bar and 10 bar, the phase shift stays almost constant (plot a)). It is negative for lower frequencies and rises with an increase of the frequency. In contrast, the high pressure regime shows a different behaviour (plot b)): The phase shift is larger for lower frequencies and drops with increasing frequency. It reaches a maximum at a backing pressure of 20 bar. The figure reveals that the usage of neon instead of helium gas leads to stronger phase shifts, especially in the high pressure regime.

The resulting D_2 curve is depicted in figure 5.10. All D_2 values are negative. Starting with values of -276 to -305 fs^2 at low pressures, it begins to increase at 5 bar and reaches the maximum of -14 fs^2 at 10 bar. Afterwards, it drops again to -338 fs^2 (at 20 bar) before rising to -227 fs^2 (at 23 bar).

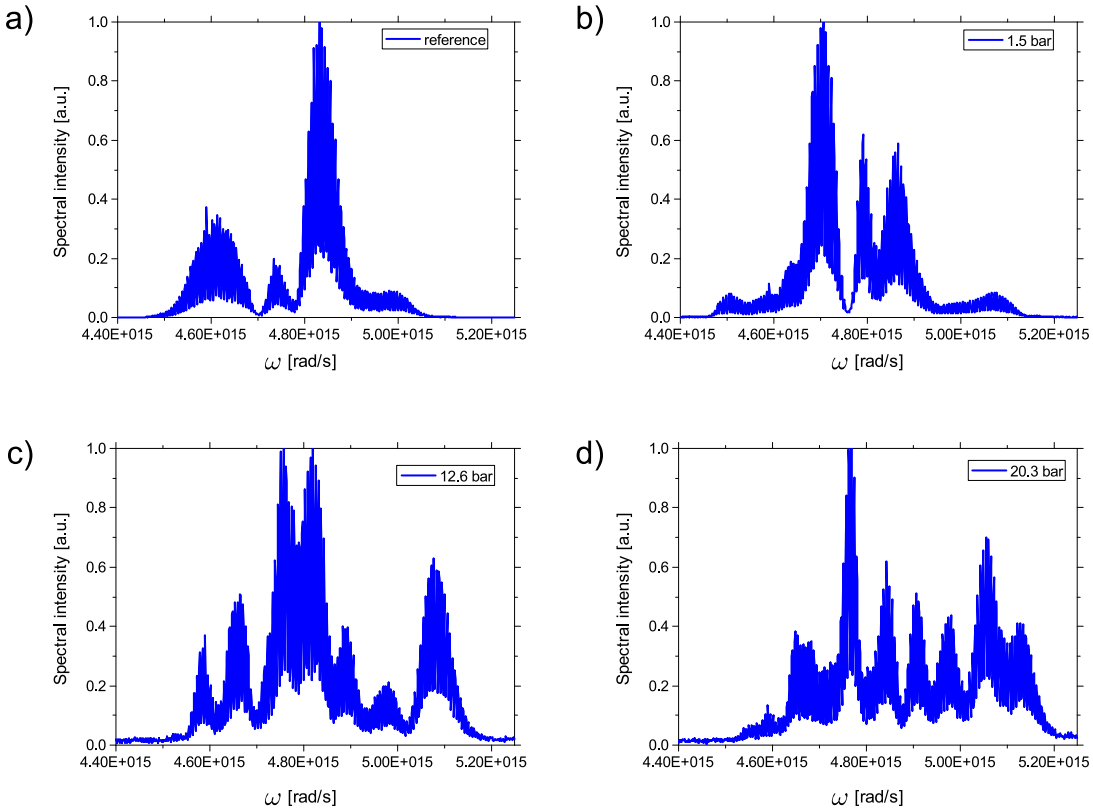

Figure 5.11: SPIDER interferograms measured for different gas (backing) pressures after the interaction with the argon gas jet (**b)-d)**) and reference interferogram (**a)**).

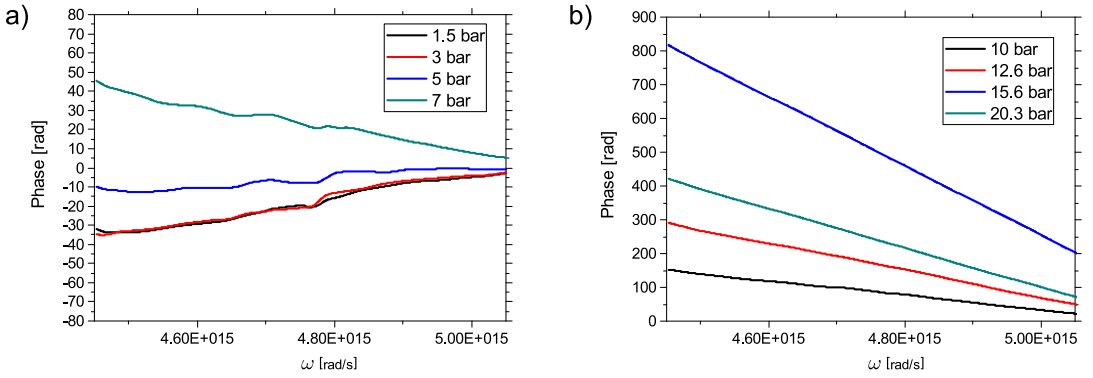

Figure 5.12: Spectral phase measured after the laser pulse interaction with the argon gas jet. The reference phase was subtracted.
a) Low pressure regime (1.5–7 bar backing pressure).
b) High pressure regime (10–20.3 bar backing pressure).

5.3.3 Results for argon gas

The laser pulse interaction with argon, the noble gas with the highest atomic number and the lowest ionisation threshold out of the three noble gases used in the experiment, was investigated for backing pressures between 1.5 and 20.3 bar. In figure 5.11, the interferograms after the interaction with the argon gas jet are shown. The periodical modulations are very distinct, especially for the highest pressure of 20.3 bar. Already for the low pressure regime, spectral components above 5×10^{15} rad/s become visible.

Figure 5.12 illustrates the phase changes due to the laser pulse interaction with the argon gas jet. Low pressures (1.5–5 bar) lead to a larger phase shift compared to helium and neon, while the trend of starting with negative values at lower frequencies is similar to the other two gases. This tendency is reversed starting at an intermediate pressure of 7 bar. A further increase of the gas pressure results in a very large phase shift with a maximum at 15.6 bar. At the highest pressure of 20.3 bar, the phase shift is still very strong. The pressure dependency of the D_2 coefficient is depicted in figure 5.13. In the low pressure regime, the D_2 coefficient is negative (-471 fs^2 at 3 bar). Starting at 3 bar, the D_2 value increases further with rising pressure and becomes positive for pressures above 12 bar. At 20.3 bar, it reaches a maximum value of 500 fs^2.

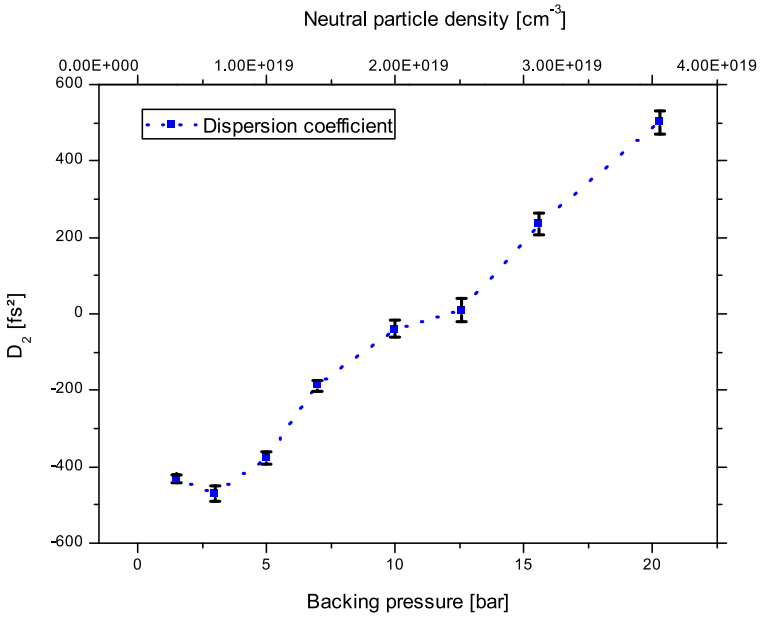

Figure 5.13: Influence of the gas jet pressure on the D_2 coefficient for the argon gas jet. The error bars denote the error of the Taylor expansion fit.

5.4 Computational results: Propagation dynamics of short laser pulses

Since solely based on the experimental results, a separation of the different effects which affect the spectral phase of the laser pulse is almost impossible, two different numerical codes were used to study the impact of the ionisation on the laser pulse.

5.4.1 3D Finite-Difference Time-Domain simulation

The simulation results were obtained in cooperation with Prof. A. Kim and E. Efimenko from the Institute of Applied Physics, Russian Academy of Sciences, Nizhny Novogord, Russia. The source code that was used is a 3D Finite-Difference Time-Domain (FDTD) simulation code [169] including plasma currents, balance equations for ionisation and Kerr-nonlinearity. The calculations were done on the Joint Supercomputer Center of the Russian Academy of Sciences (JSCC). The FDTD method is a grid-based model which uses the Maxwell equations in a discretised form. As the code is written in the time domain, the nonlinear response can be directly calculated. It is well suited for parallel-processing computer architectures [170].

The parameters of the simulation differ slightly from the experimental ones. The results were evaluated after a propagation length of 450 µm, since due to ionisation-induced

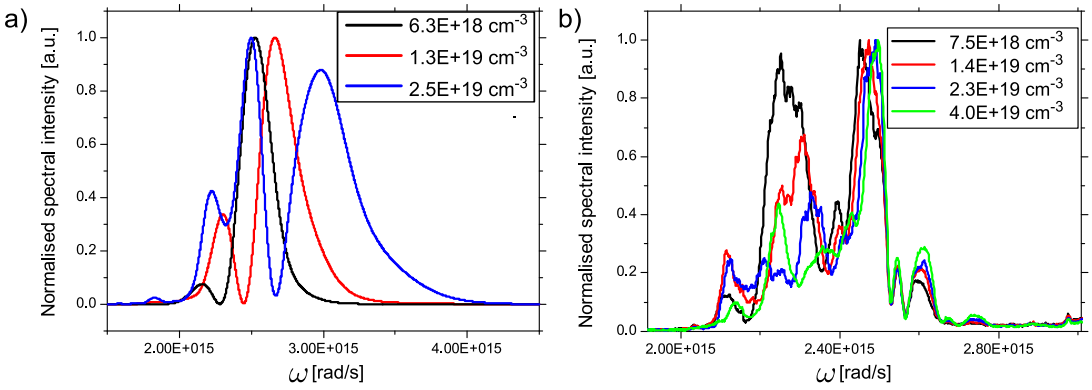

Figure 5.14: Spectra for different neutral particle densities of helium gas obtained from FDTD simulations compared to the experimental results:
a) Spectra obtained after a propagation length of 450 µm with the FDTD code.
b) Spectra obtained after the interaction with the helium gas jet in the experiment (see also: figure 5.1).

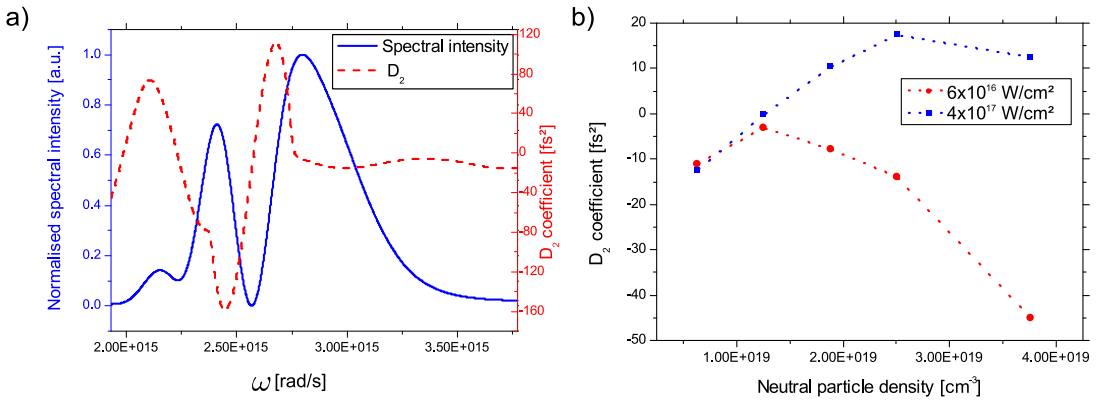

Figure 5.15: Results of the 3D FDTD simulation for helium gas:
a) Spectrum and D_2 curve for a neutral particle density of 1.9×10^{19} cm^{-3} (solid blue curve) and dispersion coefficient (red dashed curve)
b) Resulting D_2 coefficient for different neutral particle densities for two different intensities in the focal spot. Red dots show the results for a vacuum focal intensity of 6×10^{16}W/cm^2 and the blue dots correspond to an intensity of 4×10^{17}W/cm^2.

defocusing, the spectral amplitude became too low. A laser pulse with a Gaussian spectrum was injected into the 2 mm-long parabolic gas density profile. The focal spot of 4.3 µm (FWHM) was set at 250 µm after the beginning of the gas jet. The resolution of the grid was 896×896×960, one space step was $0.2\times0.2\times0.05$ µm^3 and the simulation area was $179.2\times179.2\times48$ µm^3. In the focal spot, the maximum intensity was 6×10^{16} W/cm^2 (vacuum focus). The pulse duration was 10 fs (FWHM). An additional pressure scan was done for an intensity of 4×10^{17} W/cm^2 which corresponds to a focal spot diameter of 1.6 µm, while the pulse energy remained constant.

FDTD results for helium

Figure 5.14 a) shows the resulting spectra after a propagation length of 450 µm through the parabolic helium gas jet profile for three different neutral particle densities (6.3×10^{18}–2.5×10^{19}cm^{-3}). By an increase of the particle density, the blue-shift of the spectra rises. Plot b) of the figure shows the experimental results for similar gas pressures for comparison purposes. The results of the FDTD simulation indicate a larger blue-shift than obtained in the experiment. Since the laser pulse in the experiment had a spectrum which was dominated by self-phase modulation from the propagation through the hollow core fibre prior to the gas jet interaction, it is not surprising that the blue-shift after the gas jet turns out to be smaller than in the simulation.

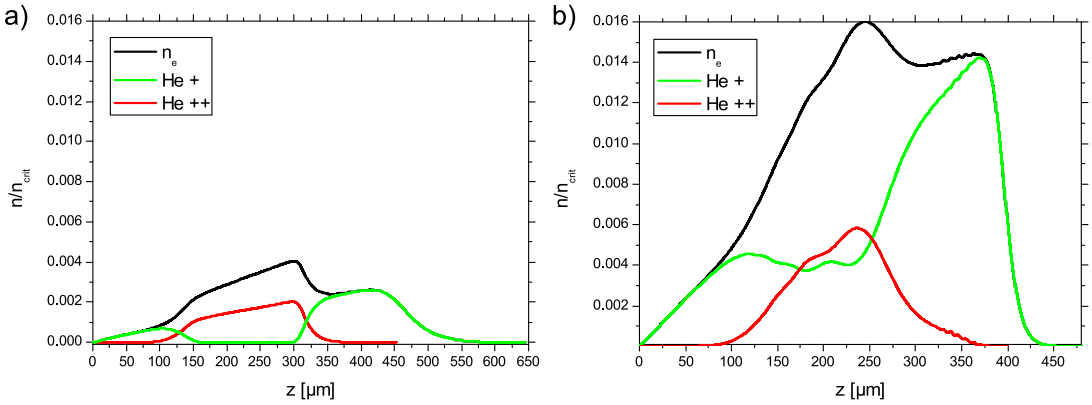

Figure 5.16: Density of the different ionisation stages of helium (He^+ and He^{++}) and electron density (n_e) as a function of the propagation length z. The intensity of the laser pulse was $6\times10^{16}\,W/cm^2$ in both cases.
a) Low pressure ($6.3\times10^{18}\,cm^{-3}$).
b) High pressure ($3.8\times10^{19}\,cm^{-3}$).

The D_2 coefficient was calculated by using a Taylor expansion. The D_2 values plotted in the graphs were evaluated at the maximum of the corresponding intensity spectrum (S_{max}). In figure 5.15 a), the spectrum for a neutral particle density of $1.9\times10^{19}\,cm^{-3}$ and the corresponding D_2 curve are shown. The resulting pressure-dependent D_2 curves for two different focal spot intensities ($6\times10^{16}W/cm^2$ and $4\times10^{17}W/cm^2$) are illustrated in plot b). It is apparent that the higher intensity leads to a shift of the D_2 curve to positive values, whereas for the lower intensity, all D_2 values stay negative and decrease even more with rising pressure. In the high intensity case, the D_2 value starts at negative values and becomes positive for neutral particle densities over $1.3\times10^{19}\,cm^{-3}$. The slope is negative for densities above $2.5\times10^{19}\,cm^{-3}$.

The ionisation dynamics during the laser pulse propagation through the helium gas jet are depicted in figure 5.16. In case of a low gas pressure ($6.3\times10^{18}\,cm^{-3}$), the ionisation starts immediately and the electron density rises. After a propagation length of 100 µm, two-fold ionisation of the helium begins. The maximum electron density is reached at $z = 300\,\mu m$. Afterwards, n_e drops and the fraction of one-times ionised helium rises, whereas the second ionisation stage vanishes. Due to the decrease of the intensity amplitude of the laser pulse during the propagation, the ionisation stops after $\sim 500\,\mu m$. For the higher pressure case ($3.8\times10^{19}\,cm^{-3}$), the fraction of He^+ rises faster than for the lower pressures. During the propagation, a part of the gas remains in the first ionisation stage. The maximum of n_e is reached at $z = 250\,\mu m$ already. No further ionisation occurs after a propagation distance of 425 µm.

Influence of ionisation versus Kerr-effect

The influence of the Kerr-effect due to the nonlinear part of the refractive index in helium gas for a neutral particle density of $2.5\times10^{19}\,\mathrm{cm}^{-3}$ is illustrated in figure 5.17. This simulation was done for the higher intensity of $I_{focus} = 4\times10^{17}\mathrm{W/cm}^2$ in order to enhance the visibility of the effect. For the first simulation run, which implemented an ionisation routine and no Kerr-effect, the spectrum of the laser pulse is strongly blue-shifted (solid blue curve) as a consequence of the proceeding ionisation and the connected change of the refractive index. The resulting D_2 value is positive with $13.4\,\mathrm{fs}^2$ at the maximum spectral intensity at $2.62\,\mathrm{rad/s}$ (dashed blue curve). If the ionisation model is 'switched off' in the FDTD simulation at the same gas pressure, only the Kerr-nonlinearity contributes to the changes of the D_2 coefficient. While the spectrum does not change during the interaction with a constant, homogeneous density profile inside the gas (solid red curve), the D_2 value becomes negative with -25 fs^2 at $2.35\times10^{15}\,\mathrm{rad/s}$ due to the Kerr-effect (dashed red curve), which is calculated by $\Delta n = n_2 I(t,r)$.

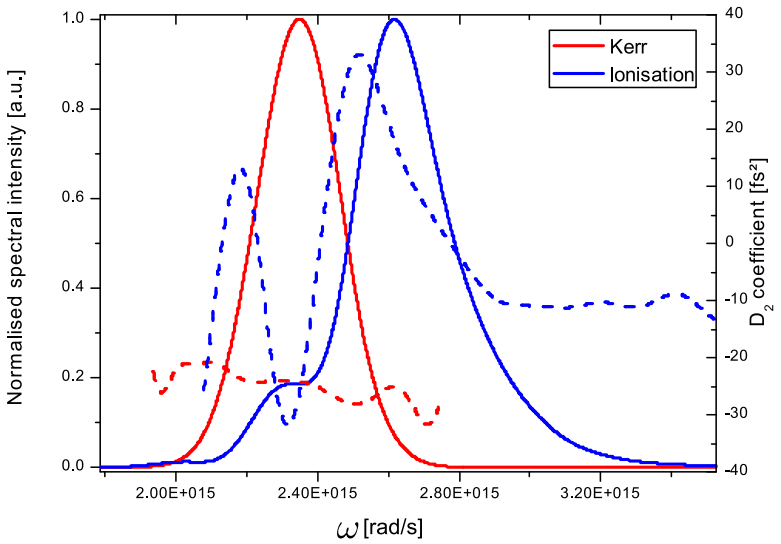

Figure 5.17: Influence of Kerr-effect and ionisation for helium for a neutral particle density of $2.5\times10^{19}\,\mathrm{cm}^{-3}$ and an intensity of $4\times10^{17}\mathrm{W/cm}^2$ in the focal spot. The solid lines depict the spectra of the laser pulse and the dashed lines indicate the D_2 coefficient as the second derivative of the phase in fs^2.

FDTD results for neon

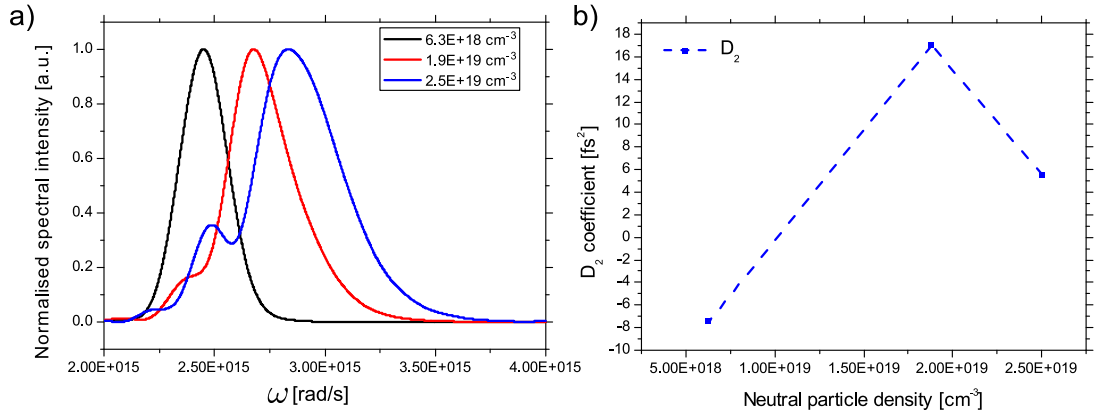

Figure 5.18: Results of the FDTD simulations for neon for an intensity of $6\times10^{16}\,\mathrm{W/cm^2}$.
a) Spectra for different neutral particle densities after the propagation through neon gas.
b) Resulting D_2 coefficient.

In figure 5.18, the results of the FDTD simulation for neon gas are shown. Plot a) illustrates the blue-shifted spectra for three different neutral particle densities. The modulations in the spectra due to self-phase modulation are not as strong as for helium in the previous FDTD simulation.

In plot b), the corresponding D_2 curve is depicted. At low pressures, the D_2 value is negative (-7.5 $\mathrm{fs^2}$), increases to the maximum value of $+17\,\mathrm{fs^2}$ afterwards, and drops down to $+5.5\,\mathrm{fs^2}$. The comparison with the corresponding experimental results illustrated in figure 5.10 reveals an agreement of the shapes of the D_2 curves with the maximum D_2 value at an intermediate pressure of $\sim2\times10^{19}\,\mathrm{cm^{-3}}$, although the total change of the D_2 coefficient was larger than in the experiment.

5.4.2 PIC simulations with the EPOCH simulation code of the laser pulse propagation in helium gas

In order to obtain a deeper understanding of the underlying physical processes during the interaction of a short laser pulse and a gaseous target, additional 2D PIC simulations were performed with the EPOCH code [171] in collaboration with Dr. Götz Lehmann from the Institute of Theoretical Physics I at the Heinrich-Heine-University. The calculations were done at the Jülich Supercomputing Centre.

Since the propagation length of the laser pulse was relatively long (1.6 mm), a moving

window setup was used. In this case, the box around the laser pulse moves through the fixed density profile with the speed of light. Due to the fact that a model for the ionisation process was necessary, version 4.0 of the EPOCH code was used. In this version of the EPOCH code, a model for multiphoton and tunneling ionisation as well as a correction of the ionisation rates based on the BSI theory is included.

The helium gas jet was described by a parabolic density profile. The focal spot size of the laser was 4.3 µm (FWHM) and was set to be reached 350 µm after the beginning of the density profile with a focal spot intensity of $6\times10^{16}\,\mathrm{W/cm^2}$. The moving window simulation box had a size of $120\lambda\times400\lambda$ where λ is the central wavelength of 800 nm. A full propagation length in the simulation was 1.6 mm. The resolution of the grid was 4096×2048 with 10 macro particles per cell. Neutral particle densities from $0.003n_{\mathrm{crit}}$ to $0.1n_{\mathrm{crit}}$ ($5.2\times10^{18}\,\mathrm{cm^{-3}}$ to $1.7\times10^{20}\,\mathrm{cm^{-3}}$) were studied for two different pulse durations (10 fs and 20 fs). It has to be stated that the PIC code has not implemented a model for the Kerr-nonlinearity, thus the influence of the ionisation effects on the laser pulse can be investigated separately from the Kerr-effect.

Figure 5.19 illustrates the spectra after the propagation through the helium density profile for the two pulse durations obtained by the PIC simulation code. Plot a) shows the blue-shifted spectra for the short pulse (10 fs). The blue-shift of the maximum of the spectrum increases with rising pressure and a broadening of the spectrum occurs. Intensity modulations due to self-phase modulations appear especially on the red part of the spectrum. In case of the 20 fs laser pulse (plot b)), the spectral broadening and the total blue-shift turn out to be smaller which is closer to the experiment than the results from the FDTD simulations.

The results of the 2D PIC simulation for the propagation through the helium gas jet for different neutral particle densities ($0.003n_{\mathrm{crit}}$ to $0.1n_{\mathrm{crit}}$) at the same time step and a pulse duration of 10 fs are depicted in figure 5.20. All images were taken after a propagation length of 256 µm. The upper row of images shows the electric field of the laser pulse, the density profile of He^+ is illustrated in the images in the middle row and the bottom row images depict the corresponding electron density. In the low pressure case ($0.003n_{\mathrm{crit}}$), the laser pulse is shown shortly before it reaches its minimum diameter. For the higher pressures, the laser pulse is already defocused at the same propagation length. The higher the neutral particle density is, the earlier the ionisation-induced defocusing becomes significant. Since the first cycles of the ultrashort laser pulse are intense enough to overcome the ionisation threshold of helium, the majority of the pulse passes through the electron density and thereby experiences a time-dependent refractive index change. Single-ionised helium atoms are only present in the front part of the laser pulse, so that the main part of the pulse

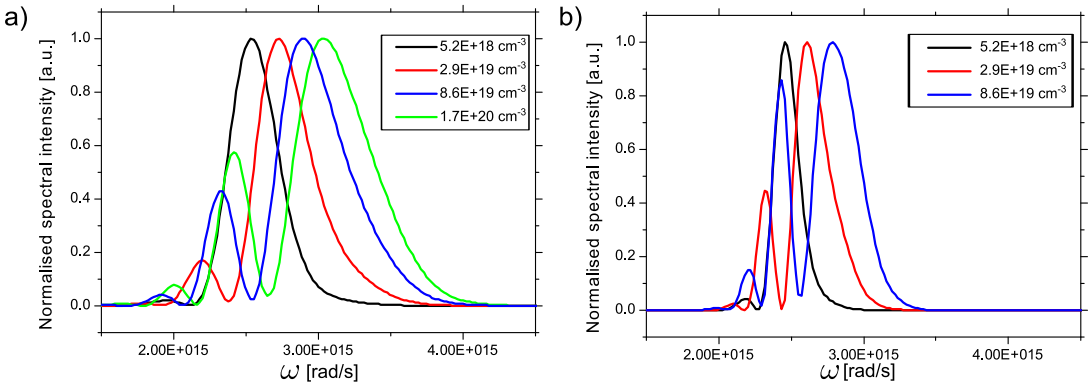

Figure 5.19: Spectra for different neutral particle densities after the laser pulse propagation through the helium gas jet. The intensity in the focal spot was $6\times10^{16}\mathrm{W/cm^2}$ for both cases.
a) Pulse duration of 10 fs.
b) Pulse duration of 20 fs.

interacts with a higher electron density corresponding to the second ionisation stage. By increasing the neutral particle density, the defocusing starts earlier and also the expansion of the electron density profile is extended. The number of electrons within this profile is higher as well, although the laser intensity is diminished.

Due to the ionisation-induced defocusing, the focusablility of the laser beam is limited at higher gas pressures. According to [33], ionisation-induced defocusing becomes dominant if:

$$\frac{n_e}{n_{\mathrm{crit}}} > \frac{\lambda}{\pi z_R} \tag{5.1}$$

Thus, under the experimental conditions, defocusing is important for pressures above $5\times10^{-3}n_{\mathrm{crit}}$.

In figure 5.21, the results for a laser pulse with a duration of 20 fs are depicted. The long duration of the laser pulse leads to an extended electron density profile (in x-direction) compared to the short (10 fs) pulse. In this case, defocusing effects occur at shorter propagation lengths and lower pressures. The first cycles of the laser pulse are not intense enough to overcome the ionisation threshold, hence they cannot be influenced by the electron density. Since the propagation length of the trailing part of the laser pulse through the electron density is longer than for the front part, the defocusing effect is stronger for the trailing part.

Summarising, there are two main influences of the interaction of laser pulse and gas jet on

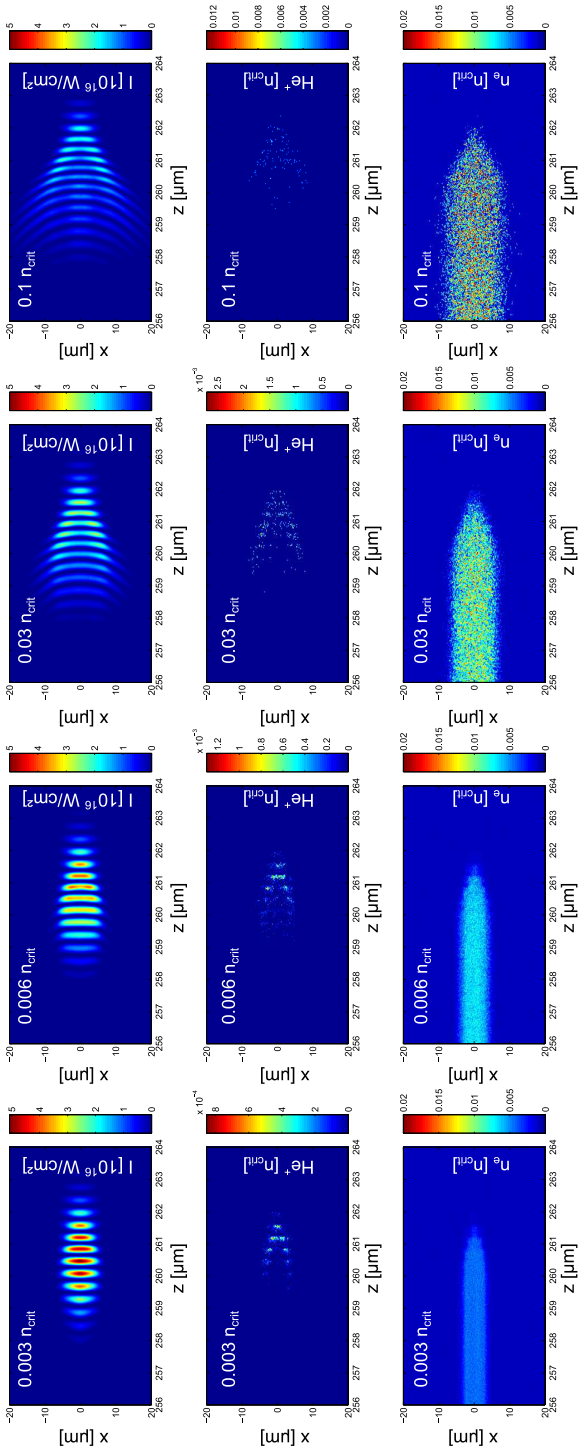

Figure 5.20: Results from 2D PIC simulations: Laser pulse propagation through different neutral particle densities of helium gas. The neutral particle density increases from $0.003 n_{\mathrm{crit}}$ in the left to $0.1 n_{\mathrm{crit}}$ in the right images. The pulse duration is 10 fs.
Upper row of images: Electric field of the laser pulse in $10^{16}\mathrm{W/cm}^2$
Middle row of images: Density of He^+ in units of n_{crit}.
Bottom row of images: Electron density in units of n_{crit}.

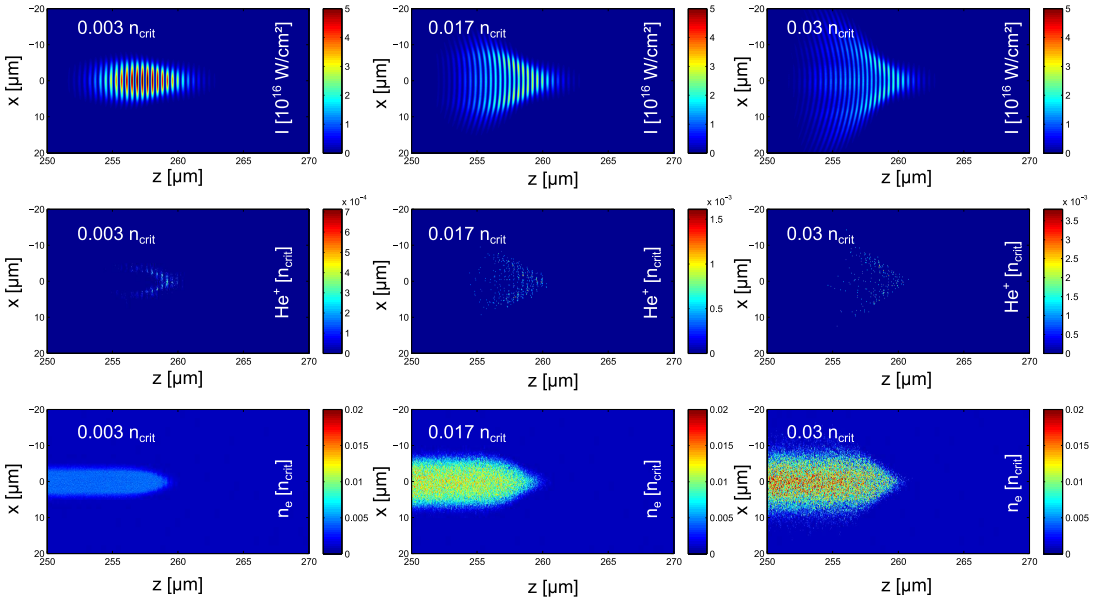

Figure 5.21: Results from 2D PIC simulations: Laser pulse propagation through different neutral particle densities of helium gas. The neutral particle density increases from $0.003 n_{\mathrm{crit}}$ in the left to $0.03 n_{\mathrm{crit}}$ in the right images. The pulse duration is 20 fs.
Upper row of images: Electric field of the laser pulse in $10^{16}\mathrm{W/cm}^2$
Middle row of images: Density of He^+ in units of n_{crit}.
Bottom row of images: Electron density in units of n_{crit}.

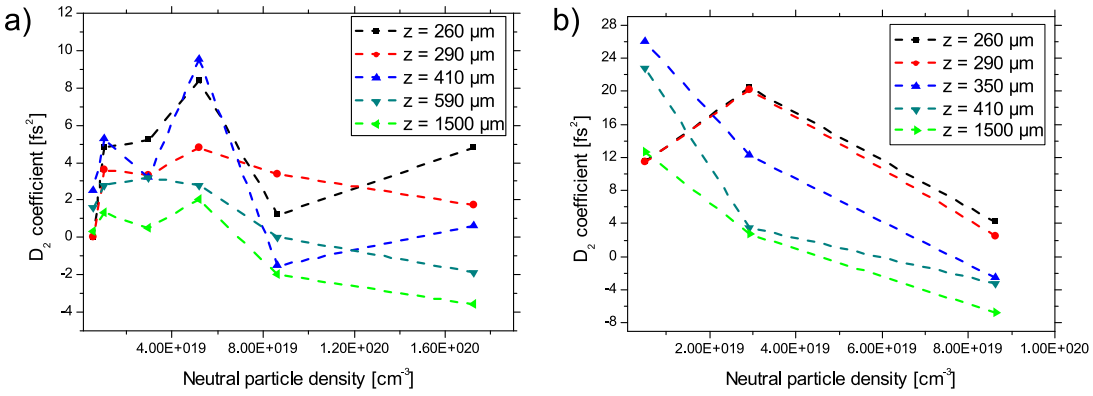

Figure 5.22: Results from the 2D PIC simulations: D_2 coefficients for different neutral particle densities evaluated for different propagation lengths z at the frequency of the maximal spectral intensity.
a) Pulse duration of 10 fs.
b) Pulse duration of 20 fs.

the spectral phase of the laser pulse: Firstly, due to the proceeding ionisation, the electron density varies strongly during the propagation of the laser pulse. Hence, the refractive index changes according to equation 2.41:

$$\Delta n_{\text{plasma}} = \sqrt{1 - \frac{n_e(r)}{n_{\text{crit}}}} \tag{5.2}$$

which can be approximated by $\approx 1 - \frac{n_e}{n_{\text{crit}}}$ in case of an underdense plasma. The second effect is caused by the radial profile of the electron density which leads to different values of focusing or defocusing for different pressures.

The resulting curves for the D_2 coefficients obtained after several propagation lengths z are depicted in figure 5.22. Plot a) shows the results for the 10 fs laser pulse and b) for 20 fs, respectively. The electric field of the laser pulse was evaluated on the centre of the propagation axis at $x = 0$ and the D_2 coefficient was obtained at the frequency of the maximal spectral intensity. For the short pulse case, all D_2 curves look similar: Low pressures lead to a very small change of the D_2 value, the maximum value is reached in the intermediate pressure regime at $5.2\times10^{19}\,\text{cm}^{-3}(0.03n_{\text{crit}})$. At the highest pressure, the D_2 coefficient becomes minimal for most propagation lengths. Only two propagation lengths (260 µm and 410 µm) show an increase of the D_2 value for the highest pressure. For longer laser pulses (plot b)), two different shapes of the second-order dispersion occur: During the ionisation process ($z = 260\,\mu\text{m}$ and 290 µm), the D_2 coefficient starts with positive values of $\sim$12 fs^2, rises to $\sim$20 fs^2 and drops down to $\sim$2 fs^2 at the highest neutral particle density of $0.03n_{\text{crit}}$ ($8.6\times10^{19}\,\text{cm}^{-3}$). In case of longer propagation lengths, where no ionisation takes place due to the lower intensity of the laser pulse, the D_2 value decreases with rising pressure. The total change of the D_2 coefficient is larger than for the short pulse.

In figure 5.23, the evolution of the maximum electron density during the laser pulse propagation through the helium gas jet is shown. It is apparent, that the density rises faster, the higher the neutral particle density is. Moreover, by rising the pressure, the maximum electron density is achieved after a shorter propagation length. The refractive index change Δn is larger in case of higher pressures. While for a neutral particle density of 5.2×10^{18}, Δn is 3×10^{-3} for 20 to 230 µm and 1×10^{-3} on the second part of the propagation (230–330 µm), it is much larger for a density of 1.7×10^{20}: From 20 to 210 µm, Δn is 1×10^{-2} and for the propagation length from 210 to 330 µm, it is 9×10^{-3}. The greater and more rapid change of the refractive index at higher pressures, affects the spectral phase of the laser pulse and thus the D_2 coefficient.

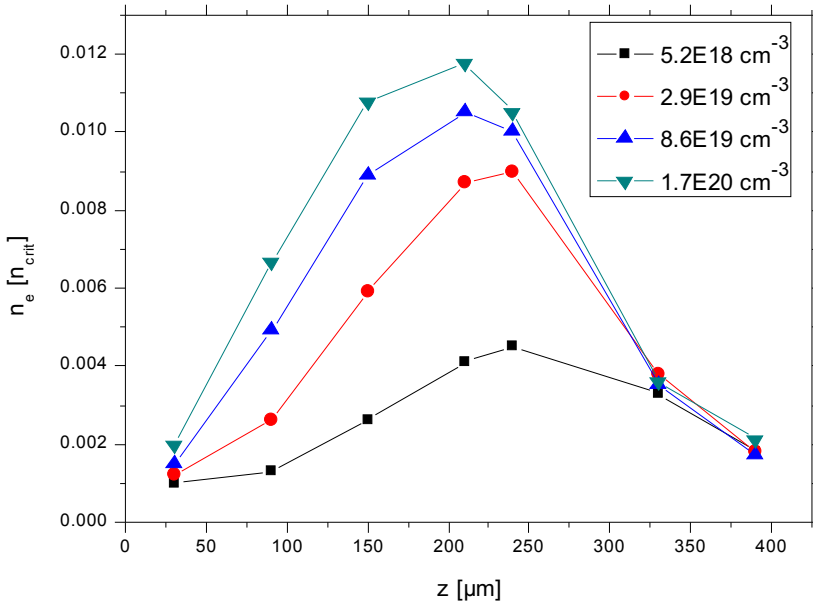

Figure 5.23: Evolution of the maximum electron density during the propagation of the 10 fs laser pulse through the helium density profile. z denotes the propagation length. The curves were obtained for different neutral particle densities.

5.5 Summary and conclusions

The D_2 coefficient indicates where and how the frequency components of the laser pulse are located with respect to the spectral envelope. With the knowledge of the D_2 value after a certain interaction length, the resulting chirp can be compensated with the help of DCMs[4], GTIs[5] or other grating or prisms setups in order to obtain a transform-limited pulse.

In the experiment with the helium gas jet, D_2 coefficients with negative and positive values were obtained. The sensitivity of the second order dispersion to the variation of the input parameters was discussed. Using neon as a target, all D_2 values were negative, although the curve nearly reached a positive value at its maximum in the intermediate pressure regime at a neutral particle density of $2\times10^{19}\,\mathrm{cm}^{-3}$. For the measurement with argon, the gas with the lowest ionisation threshold and the most ionisation stages out of the three gases examined, the total change of the D_2 coefficient was larger than for helium and neon (-400 fs^2 to +500 fs^2). The threshold intensity for the 6$^{\mathrm{th}}$ ionisation stage of argon

4 double chirped mirrors.
5 Gires-Tournois interferometers.

is $7.5\times10^{15}\,\mathrm{W/cm^2}$, whereas for helium gas the second ionisation stage is not reached for intensities lower than $8.5\times10^{15}\,\mathrm{W/cm^2}$ (see appendix A). This fact leads to a higher number of free electrons for the interaction with the argon gas jet, and thus to a greater change of the time-dependent refractive index.

In case of a pure Kerr-nonlinearity contribution, the FDTD simulation showed that the D_2 coefficient becomes negative after the propagation through helium. When the pressure of the gas rises, more electrons are set free. This effect is stronger for the central part of the beam, especially for the high intensity ($4\times10^{17}\,\mathrm{W/cm^2}$), since the ionisation rate is higher on the beam axis. Moreover, the influence of the defocusing effect increases and the D_2 value becomes positive. After a propagation length of a few hundred micrometers, the ionisation process is completed and the D_2 coefficient can drop again due to the influence of the Kerr-nonlinearity. A further rise of the gas pressure results in a corresponding earlier completion of the ionisation process after a shorter propagation length. The same behaviour results from tight focusing to $w_0 = 1.6\,\mu\mathrm{m}$.

The PIC simulations showed that after a certain propagation length ($> 290\,\mu\mathrm{m}$), the D_2 value drops with rising pressure in case of the 20 fs laser pulse. In contrast, the results for the ultrashort 10 fs laser pulse are not as straightforward, since the D_2 curve reaches a maximum in the intermediate pressure regime (at $5.2\times10^{19}\,\mathrm{cm^{-3}}$) before it drops again at higher pressures. For higher neutral particles densities, the change of the refractive index is larger and occurs during a shorter propagation length.

Nevertheless, experiment and simulations revealed that the total value of the D_2 coefficient is very sensitive to small variations of the input parameters like duration of the laser pulse, propagation length, density profile and focal spot intensity. These variations lead to changing ionisation dynamics, hence the refractive index alters influencing the spectral phase and finally the D_2 value. In the experiment, slight inevitable fluctuations of the input laser pulse led to rather large changes of the spectral phase. The spectral phase was measured after the collimation by a lens, therefore variations along the radial profile of the laser beam could not be investigated. However, it could be demonstrated that in case of taking helium as an interaction gas target, the second-order dispersion passes through negative and positive values with increasing the gas pressure. Therefore, changing the properties of the gas jet allows at least a partial dispersion control and thereby a pulse compression during the propagation. In order to make use of this effect efficiently, shorter propagation lengths inside the gas jet should be chosen, since the ionisation process is completed after $\sim$400 µm, and the further propagation through a high density gas leads to a significant amount of absorption of the laser pulse.

The comparison of FDTD and PIC simulation shows that the usage of different ionisation

routines and the implementation of the Kerr-effect lead to different results. As a consequence of the sensitivity of the input parameters, it is complicated to reproduce the exact results of the experiment by one of the simulation methods.

Beyond that, in both simulation methods, PIC and FDTD, a shortening of the laser pulse during the propagation through the gas was observed. By reducing the length of the gas jet in the experiment, this plasma compression method of the laser pulse could be used in future laser systems.

6 High-order harmonic generation from periodically modulated targets

In this chapter, the first experimental demonstration of high harmonic generation along the surface of a periodically modulated target is reported. Experimental results for harmonic generation from grating targets irradiated by laser pulses at an intensity of 2.5×10^{20} W/cm^2 were obtained in two wavelength ranges (lower-order and XUV harmonics). The properties of the generation process were studied by using 2D PIC simulations. Moreover, the influence of the interference properties of the grating is discussed. The numerical analysis indicates the physical parameters which play a crucial role in the generation process, like grating periodicity and focusing properties of the laser, for example. According to the results, there is a possibility of controlling the composition of the harmonic spectra. The separation of the harmonic radiation from the specular direction of the laser makes the grating harmonic process and emission suitable for many applications [6, 91]. The experiments were performed at the 100 TW ARCTURUS laser facility.

A systematic parametric scan performed by means of 2D PIC simulations gives insights into the angular distribution of the harmonic radiation and allows to extend the range of the analysis to interaction geometries which were not experimentally accessible.

6.1 Experimental results: low-order harmonics from corrugated targets

The investigation of high-order harmonics generated by the irradiation of intense laser pulses from corrugated targets was conducted at the ARCTURUS laser facility. The setup is described in section 4.4. The laser was focused at an incidence angle of $\theta = 25\,^\circ$ relative to the target normal onto different grating targets. The lower-order harmonics (2^{th} and 3^{rd}) were detected at an angle of $\alpha = 25\,^\circ$. The UV spectrometer that was used, is described in section 4.5.2. A list of the targets which were utilised in this experiment and an overview of the results can be found below in table 6.1. An atomic force microscope image of one of the

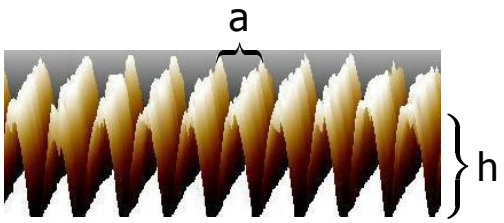

Figure 6.1: 3D atomic force microscope image of a corrugated target (G1: $a = 410\,\text{nm}$, $h = 70\,\text{nm}$).

	a	h	observation at 25°
G2	250 nm	50 nm	weak 2nd order harmonic
G3	410 nm	60 nm	2nd and 3rd order harmonics
G4	480 nm	85 nm	weak 2nd and strong 3rd order harmonics
flat glass	-	-	weak 2nd order harmonic (surface quality: $\lambda/20$)

Table 6.1: Targets used in the grating harmonics experiment (low-order harmonics) and overview of the obtained results at an observation angle of 25°.

gratings is depicted in figure 6.1. The longitudinal periodicity is given by the parameter a, h denotes the vertical amplitude of the protuberances. The grooves were oriented parallel to the laser polarisation. The single plasma mirror system (described in detail in chapter 3.3) was implemented into the beam path in order to preserve the structure of the periodically modulated target prior to the arrival of the main pulse at the surface.

Figure 6.2 illustrates the results of the emission of the second- and third-order harmonic for the different grating targets compared to a flat target. Part a) of the figure shows the emission of the second-order harmonic. The inset depicts a closer look on the harmonics which were not as efficiently generated as the one from grating G3 ($a = 410\,\text{nm}$, blue spectrum). All spectra were obtained under the same experimental conditions. The spectral intensity is expressed in number of counts on the Andor CCD camera. The offset value of 398 counts was subtracted for all spectra.

By employing a flat glass target (surface quality: $\lambda/20$), which is commonly used for high harmonic generation at an incidence angle of 45 °, the 2nd order harmonic was detected at the observation angle with rather low efficiency (maximum of seven counts in six shots, see black spectrum in figure 6.2 a)). An emission of the third-order harmonic could not be detected with the spectrometer. The results for grating G2 ($a = 250\,\text{nm}$) were similar (see orange spectrum). The second harmonic was emitted with a maximum of eight counts in

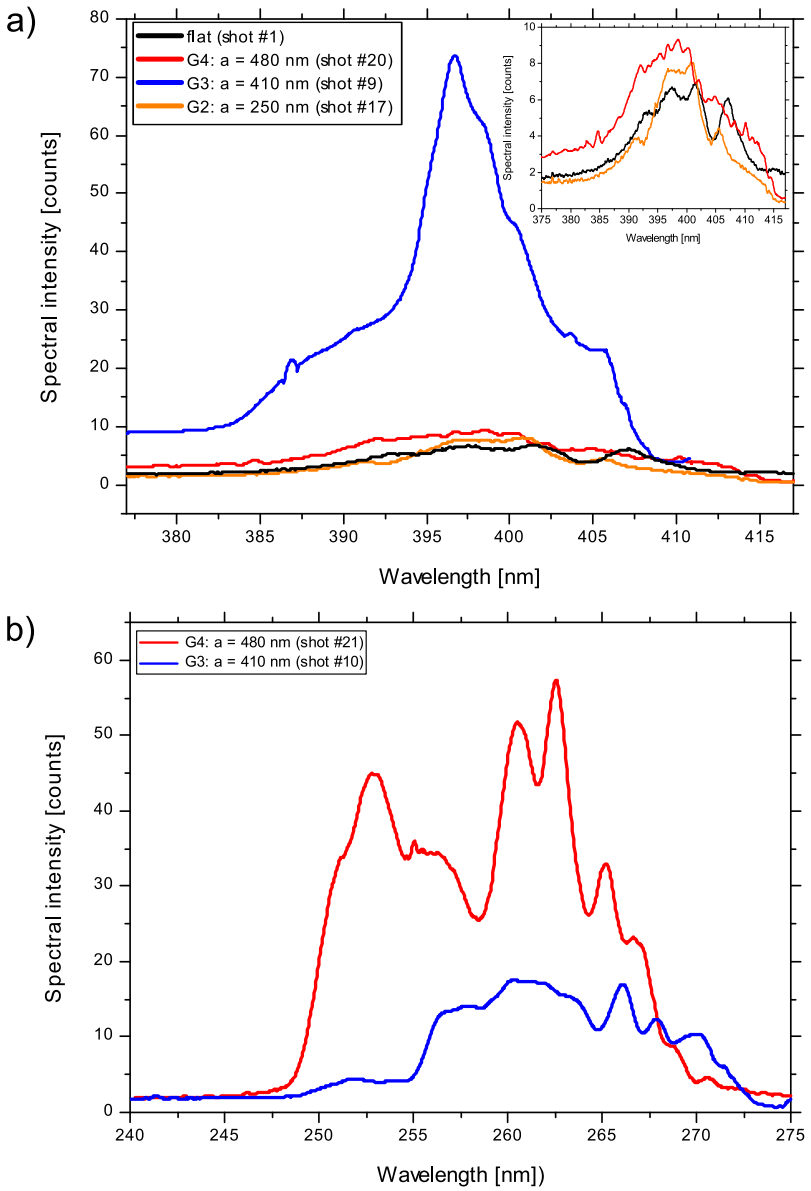

Figure 6.2: Overview of the experimental results of low-order harmonic generation from grating targets. The spectra were obtained with the UV spectrometer.
a) Spectral intensity of the 2nd order harmonic for different types of targets. The inset depicts a zoom into the spectral intensity of the 2nd harmonic for the flat target and grating G2 and G4.
b) Spectral intensity of the 3rd order harmonic from grating G3 and G4. The spectra from the flat target and G2 are not shown, as no counts above the noise level were detected.

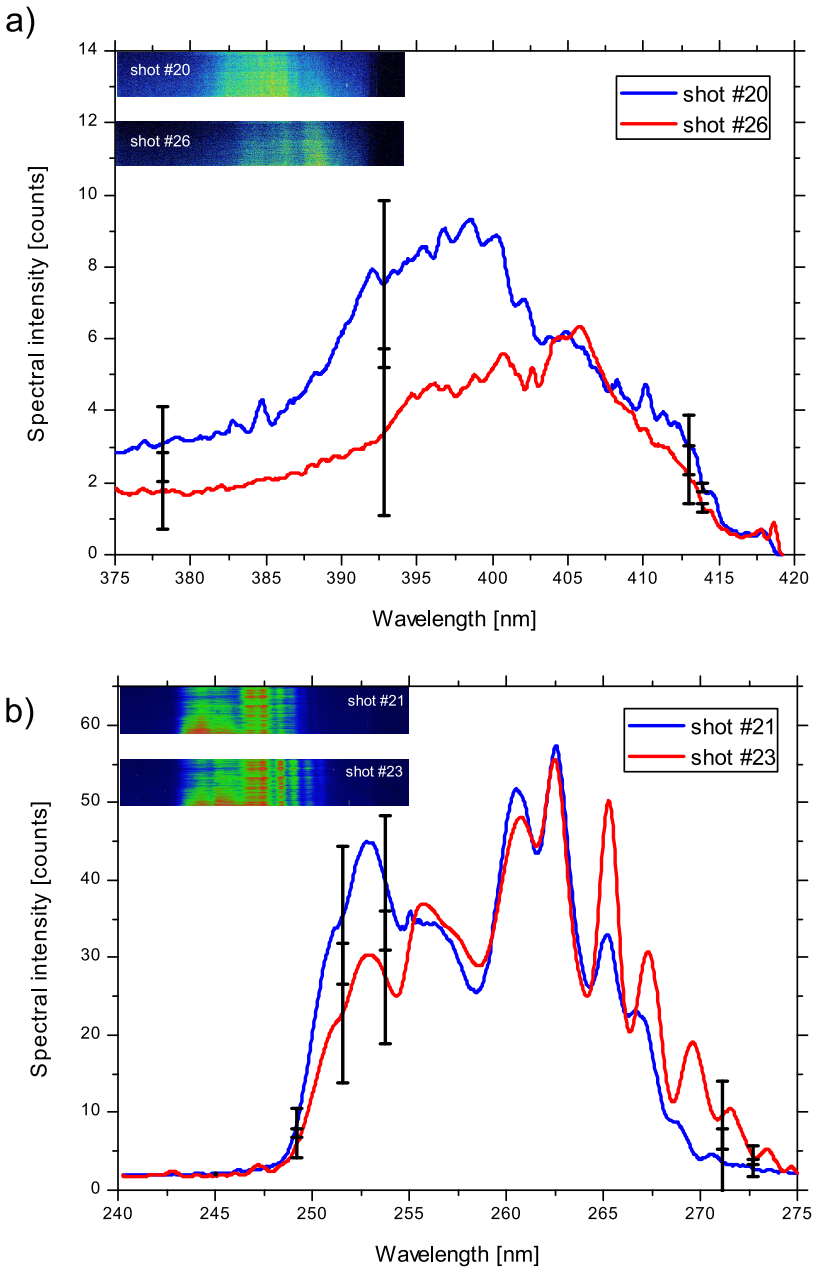

Figure 6.3: Experimental results: Examples of second (**a**)) and third order (**b**)) harmonic generation from G4. The insets show the raw spectra obtained with the UV spectrometer. The observation angle was 25°. In the plots, the error bars mark the standard deviation from the average value of the evaluated shots.

four shots, but the third harmonic could not be recorded either.

The behaviour for G3 (a = 410 nm) was different: Both 2nd and 3rd order harmonics were emitted intensively (see figure 6.2, blue spectra in a) and b)). The generation efficiency of the second harmonic from G3 (maximum 74 counts) was about seven times higher than for the other gratings and flat targets. The comparison of the absolute number of counts of second- and third-order harmonics reveals that the maximum of the spectral intensity of the second-order harmonic is more than four times the maximum number of counts of the third harmonic (16 counts).

By using grating G4 (a = 480 nm) with a periodicity only differing 70 nm from the previous grating (G3), the usual reduction of the third harmonic compared to the second was reversed. The signal of the third harmonic was six times the signal of the second order (see figure 6.2, red curves). The enhancement of the third-order harmonic has not been observed so far and is a direct consequence of the effect of the grating periodicity on the efficiency and angular distribution of different harmonic orders. The results were well reproducible as exemplarily illustrated in figure 6.3. Part a) shows the spectral intensity of the second harmonic for two different shots. The maximum standard deviation for four evaluated shots is marked by the error bars. Even though the error bars seem to be large compared to the absolute number of counts, the tendency of a low emission efficiency of the second harmonic is the same for all the shots. The shot-to-shot variation of the third-order harmonic is depicted in part b). The high number of counts for the third harmonic was obtained repeatedly. This supports the reproducibility of the strong emission of the third order compared to the second harmonic. In order to obtain a better understanding of these effects, 2D PIC simulations were performed that focus on the generation of low-order harmonics. The results are discussed in detail in the next section.

6.2 Simulations of low-order harmonic generation from corrugated targets

A 2D PIC simulation was set up using the EPOCH simulation code [171]. The size of the simulation box was $12\lambda \times 16\lambda$ with 45 macro particles per cell. The resolution of the grid was 166 cells/λ and 125 cells/λ, respectively. The intensity of the laser pulse on the target was 2×10^{20}W/cm^2 and the focal spot size was 1 µm (if not stated differently). The central wavelength was 800 nm. Figure 6.4 illustrates the simulation box. The laser pulse, propagating from the left-hand side, is focused at $(x,y) = (0,0)$. As target, a sinusoidal grating structure with a thickness of 2 µm of ten times ionised aluminium was implemented.

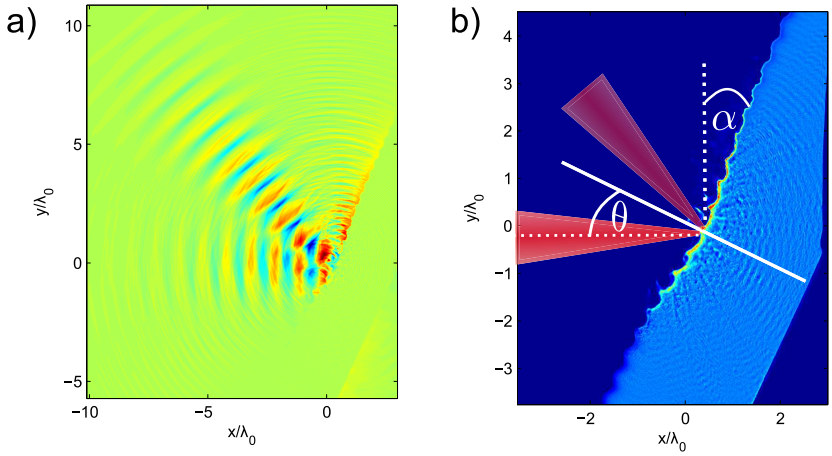

Figure 6.4: Simulation box used in the 2D PIC simulations with the EPOCH code. Laser shines onto the target from the left-hand side. The incidence angle θ is 25 ° towards target normal. Part a) and b) show the same time step.
a) Magnetic field B_z perpendicular to the polarisation of the incoming light.
b) Electron density and angular geometry of incoming and reflected laser beam.

The height of the protuberances h was 50 nm. Part b) of figure 6.4 shows the electron density of the target during the interaction with the 27 fs long laser pulse, whereas a) depicts the magnetic field B_z perpendicular to the simulation plane. An extensive parametric scan was performed in order to study the influence of grating periodicity, focal spot size, preplasma conditions, height of protuberances and incidence angle. The results are discussed in the following sections.

6.2.1 Influence of the grating periodicity

The harmonic emission was evaluated around the angle α equivalent to the experiment. The magnetic field B_z perpendicular to the simulation plane was sampled after the reflection of the laser pulse from the target. Via a 2D Fourier transformation, the spectral distribution was obtained for the observation direction. The results of the 2D PIC simulation for different grating periodicities are depicted in figure 6.5. In comparison to the flat target, an enhancement of the harmonic emission at this angle up to two orders of magnitude can be observed (figure 6.5 b)). For the grating with a periodicity of $a = 250$ nm, harmonics 5–8 dominate the spectrum (black spectrum in figure 6.5 a)). Contrary to this, the spectrum obtained from G3 (a = 410 nm, red curve) is dominated by the emission of the 4$^{\text{th}}$ harmonic. Second and 3$^{\text{rd}}$ order harmonics are emitted with the same efficiency at the evaluated angle

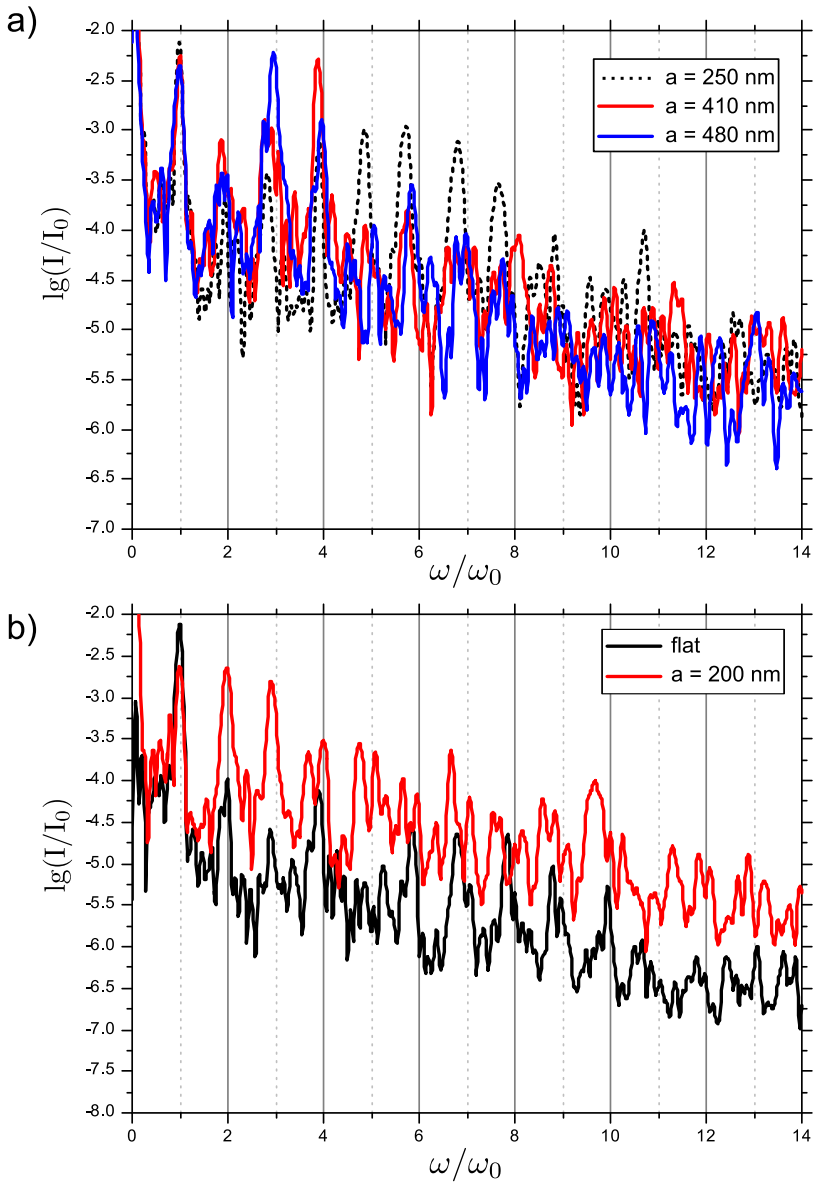

Figure 6.5: 2D PIC simulation results obtained with the EPOCH code. The spectral distributions of the high harmonics at 25° for different grating periodicities are shown for:
a) Grating periodicities used in the experiment.
b) Small grating periodicity compared to a flat target.

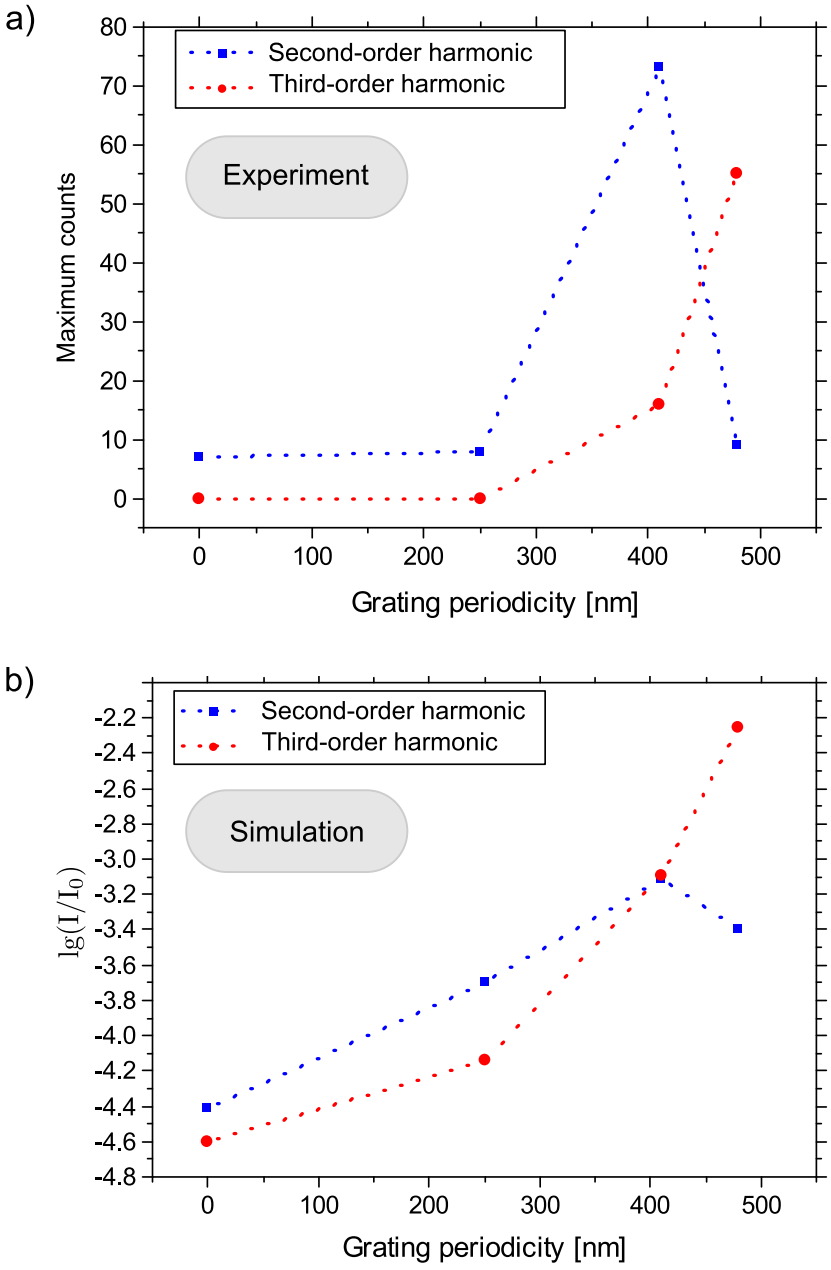

Figure 6.6: Overview and comparison of simulation and experimental results of the second- and third-order harmonic emission for different grating periodicities and flat target at $\theta = 25°$.
a) Maximum counts of the second- (blue dots) and third-order (red dots) harmonics obtained in the experiment.
b) Maximum emission of the second- (blue dots) and third-order (red dots) harmonics obtained by the 2D PIC simulation at the same observation angle as in the experiment.

of $\theta = 25°$ in agreement to the experimental results in section 6.1. A direct comparison will be drawn in the following.

For the grating target G4 ($a = 480$ nm; blue spectrum), the emission of the 3rd harmonic is more than one order of magnitude more intense than the second harmonic. This enhancement of the 3rd order harmonic was also visible in the experiment. By changing the grating periodicity, the emission of selected harmonic orders can be enhanced or suppressed. This effect was observed in the simulations where the results show a very strong emission of the harmonic orders 5–8 for G2, 4 for G3 and 3 for G4. Part b) of figure 6.5 shows an efficient generation of the second and third order for a grating with a periodicity of 200 nm. The results of the simulations indicate the possibility of selecting several harmonic orders by changing the grating periodicity.

In figure 6.6, the results of simulation and experiment are directly compared. The level of emission at 25° is plotted as a function of the grating periodicity[1]. The detected emission level in the experiment is given by the absolute number of counts on the CCD camera while the simulation results are depicted with respect to the incoming intensity ($\log(I/I_0)$). Usually, the emission efficiency drops with the harmonic order (see i. e. figure 2.9), thus the detectable emission of the third harmonic is lower than the second. The same tendency was observed in the grating experiment and simulation for the flat target, grating G2 and G3. By changing the grating periodicity to a = 480 nm (G4), the result is completely different. Both, simulation and experiment show the higher efficiency of the third harmonic compared to the second harmonic for G4 at the investigated observation angle. The trend of the experimental results for second- and third-order harmonics is in good agreement with the results from the simulation (figure 6.6 a) and b)).

In order to study the emission over the full angular range, spectrograms (incidence angle $\theta = 25°$) for the two gratings (comparable to G3 and G4 used in the experiment) are shown in figure 6.7. Lineouts of these spectrograms which were taken at the observation angle (25° with respect to the target surface), were already shown in figure 6.5 a). The circles in the figure mark the harmonics predicted by the interference formula (equation 2.55). It can be seen that for grating G4, the third harmonic can be predominantly found around the observation angle whereas in case of G3, the fourth order harmonic dominates the harmonic spectrum at the observation angle. By changing the grating periodicity, the different harmonic orders can be enhanced at the observation angle which differs from the specular direction. This allows to obtain customised harmonic emission by using a target with a suitable grating periodicity.

1 A grating periodicity of zero denotes the flat target.

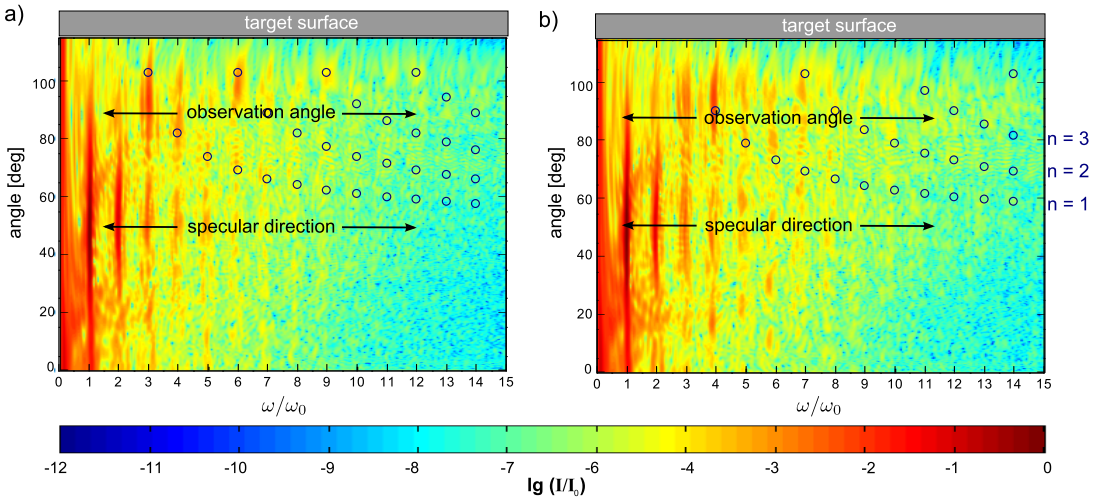

Figure 6.7: Spectrograms from corrugated targets over an angular range of 115° obtained from EPOCH simulation. The observation angle α was 25° with respect to the target surface (corresponds to angle = 90°). The spectral relative intensity is shown as a function of the harmonic order and emission angle. Blue circles mark the emission angles of the harmonics predicted by equation 2.55. n = 1...n = 3 denote the different interference orders.
a) Grating periodicity a = 480 nm (G4).
b) Grating periodicity a = 410 nm (G3).

6.2.2 Influence of the focal spot size

The influence of the focal spot size on the target on the emitted harmonic radiation was studied under the same geometrical conditions as described in the previous paragraph. The results for grating G2 and G3 are shown in figure 6.8 a) and b). By choosing a small focal spot size of $w_0 = 1\,\mu$m, low-order harmonics (3–8) are strongly emitted for G2 (figure 6.8 a)). For higher orders, the spectrum contains gaps, and mainly odd harmonic orders are generated. The illumination of larger areas ($w_0 = 2$ and 4 µm for the same pulse energy) leads to an enhancement of the interference effect and thus a stronger emission of the harmonics around the respective harmonic predicted by equation 2.55 ($\cos\alpha = \frac{n}{m}\frac{\lambda_0}{a} + \sin\theta$). The harmonic orders fulfilling the interference condition are depicted by the green stars in figure 6.8. In case of grating G2 with $a = 250$ nm, four "bunches" around the harmonic orders 7, 13, 20 and 26 are visible for a w_0 of 4 µm (blue spectrum in figure 6.8 a)). The emission of other harmonic orders is suppressed. More bunches (around the 4th, 8th, 12th, 16th, 20th, 24th and 27th harmonic order) appear for G3 ($a = 410$ nm; see figure 6.8 b). In this case even for a small focal spot size ($w_0 = 1\,\mu$m), several harmonic orders are emitted more intensively than the rest (for example 4th, 7th, 16th, 17th, 22th, 24th).

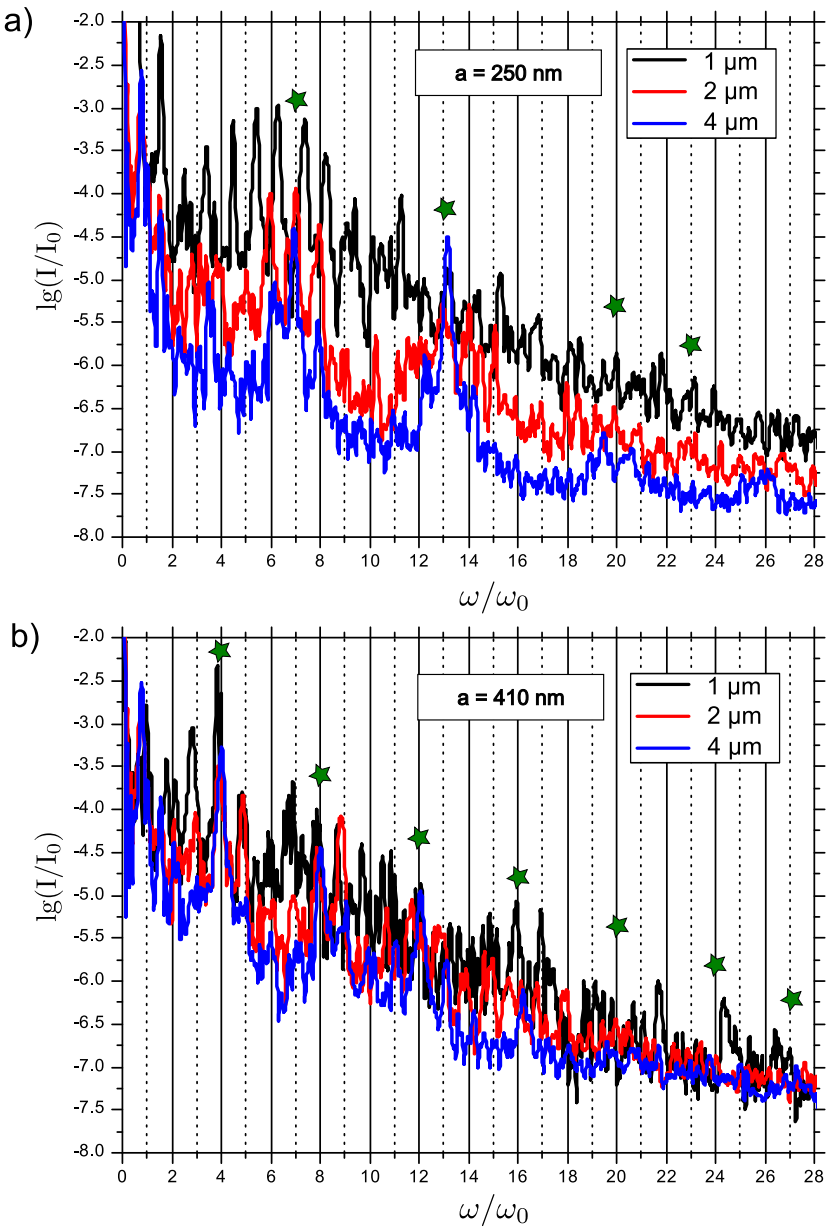

Figure 6.8: 2D EPOCH simulation results: Spectral distribution at $\alpha = 25°$ for different focal spot sizes $w_0 = 1, 2$ and $4\,\mu$m (incidence angle $\theta = 25°$). The energy of the laser pulse is equal for all focal spot sizes. The green stars depict the harmonic orders which are predicted by the interference formula at the observation angle α.
a) Spectral distribution for G2.
b) Spectral distribution for G3.

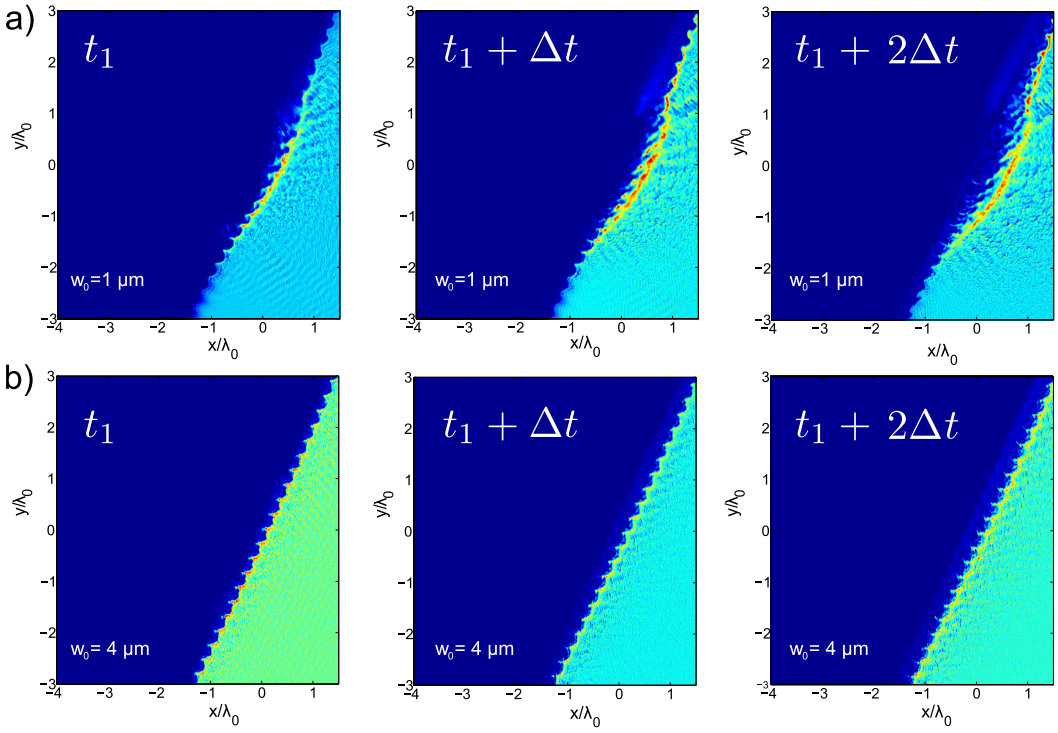

Figure 6.9: Electron density of a grating target (a = 250 nm) during and after the interaction with a 27 fs laser pulse for three different time steps. Δt is 10.7 fs. The t_1 time step depicts the electron density when half of the laser pulse is reflected. In the $t_1 + \Delta t$ time step, the reflection is almost completed, and the last time step shows the electron density right after the reflection. The energy of the laser pulse is equal for both focal spot sizes.
a) Focal spot size $w_0 = 1\,\mu m$.
b) Focal spot size $w_0 = 4\,\mu m$.

The bunching effect around the harmonic orders predicted by the interference formula is more evident for grating G2 since more protuberances contribute to the generation process for the same focal spot size compared to G3. The illumination of larger areas leads to a scenario which is closer to the predictions made by the simulations in [15, 16] as the wavefront curvature does not play a crucial role for larger focal spot sizes. According to the analytical interference formula, the incidence angle on the target is fixed. The simulation results obtained by Lavocat et al. are in good agreement with the predictions by the interference formula as they used a plane wave to describe the electric field of the laser.

Since the electron dynamics play a crucial role in the generation process of high harmonics, they were studied for different focal spot sizes on the target. The electron density on the

target surface (a = 250 nm) during the interaction is depicted in figure 6.9. In part a), the focal spot size is 1 µm. The first time step t_1 pictures the moment when half of the laser pulse is reflected. The periodical structure of the grating target is still noticeable. 10.7 fs later (second picture), when the reflection of the 27 fs laser pulse is almost completed, the surface is strongly dented and the periodical structure starts to disappear. The last time step $t_1 + 2\Delta t$ shows the status of the target right after the reflection. In this picture, the grating structure is completely destroyed. A different behaviour of the electron density is found for larger focal spot sizes. In part b) of the figure, w_0 is 4 µm. The periodical structure of the grating target remains visible for all the time steps. In this case, more protuberances are illuminated by the laser. More interference orders can contribute to the resulting harmonic spectrum, thus the harmonic orders which were predicted by the interference formula become more intense (see figure 6.8 a), blue spectrum). Moreover, because of the lower intensity in the focal spot, the denting of the surface is negligible so that fewer incidence angles have to be taken into account than in case of a small focal spot size in a).

6.2.3 Influence of the preplasma

The temporal contrast of the laser pulse and thus the expansion of the preplasma, play an important role in the generation process of high harmonics from solid surfaces. Figure 6.10 illustrates the simulation results of the harmonic emission for different plasma scale lengths L. The preplasma influence was studied for a 27 fs laser pulse and a grating with a periodicity of 410 nm. The height of the protuberances was 50 nm. In case of a very high temporal contrast of the incoming laser pulse, the resulting preplasma is small. Two small preplasma scale lengths (L = 2.8 nm and L = 17 nm) were considered, and the resulting high harmonic spectra are depicted in figure 6.10 a). For all these steep plasma gradients, the harmonic spectra look very similar. The harmonic orders which appear are sharply defined. By increasing the plasma scale length to 44 nm, the emission efficiency rises by more than one order of magnitude, especially for the lower-order harmonics (see figure 6.10 b)). A further increase of the plasma scale length to L = 60 nm leads to a significant reduction of the emission efficiency and the formation of the harmonics. In this particular case, the plasma scale length exceeds the height of the protuberances. Hence, the target structure is destroyed and interference effects become negligible.

The optimum scale length for an efficient generation of harmonics from grating targets was found to be below the height of the protuberances at several tens of nanometers. Nevertheless, small plasma scale lengths, as obtained from the ARCTURUS laser using a plasma mirror, ensure the generation of grating harmonics as the structure of the periodically modulated surface is preserved before the main pulse interacts with the target (also see

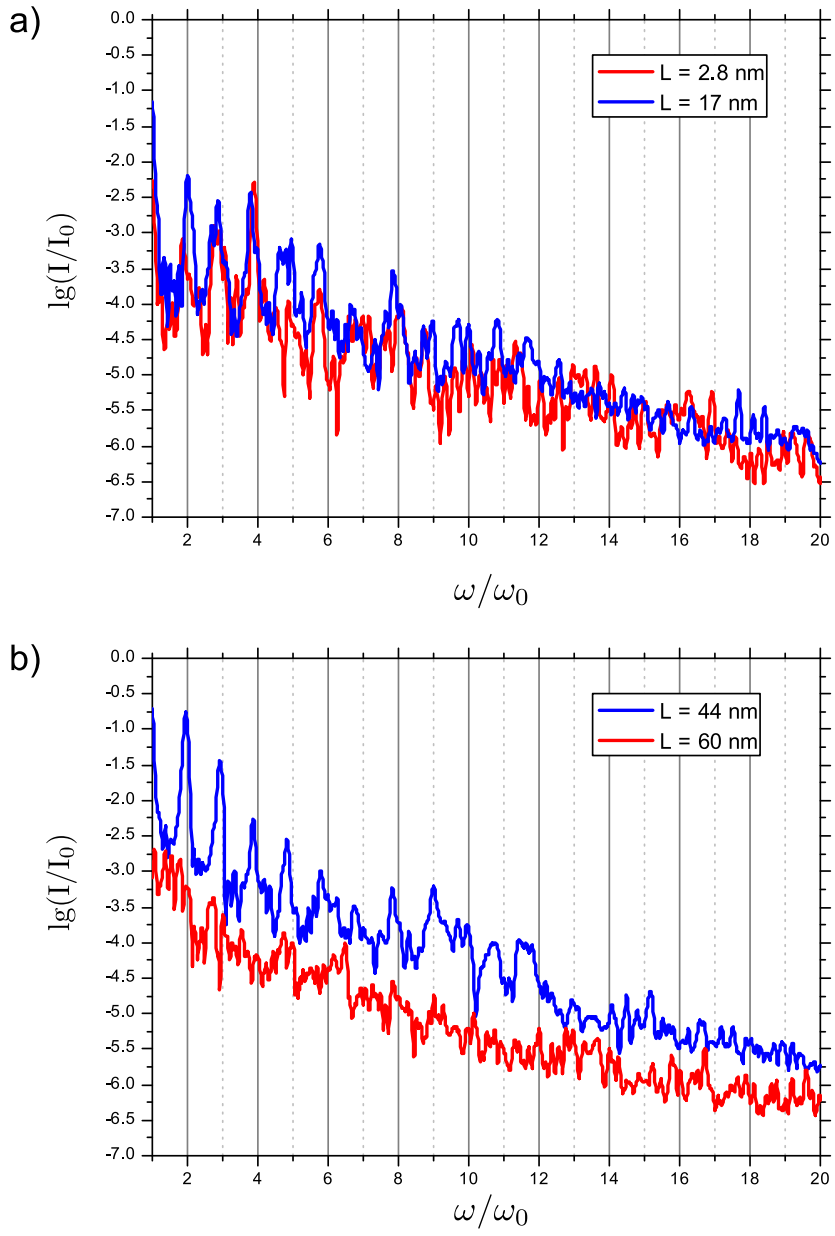

Figure 6.10: 2D EPOCH simulation results: Spectral distribution at $\alpha = 25^\circ$ for different preplasma conditions. The periodicity of the grating was 410 nm and the height of the protuberances was 50 nm.

results of the MULTI-fs simulation in chapter 3.3.6). Behmke et al. [10] showed for flat targets that a medium contrast leads to a more intense emission of CWE harmonics. The contrast requirements for using grating targets are much higher compared to flat ones. Already a plasma scale length of 60 nm which only slightly exceeds the height of the protuberances, leads to a suppression of the harmonic generation at the observation angle as the interference properties of the grating are diminished (figure 6.10 b), red curve).

6.2.4 Effect of the height of the protuberances

The height of the protuberances h was varied from 48–120 nm for a grating with the periodicity of 410 nm. Figure 6.11 illustrates the results. The spectra for all different heights look very similar in terms of efficiency and occurrence of certain harmonic orders. In the simulations, the variation of the height of the protuberances did not lead to a significant change of the spectral distribution. The influence of the interference effect is visible in all evaluated spectra. Nevertheless, the emission efficiency is higher for all heights than for the flat target under the same conditions (see figure 6.5 b)). Since all spectra in this paragraph were evaluated at $\alpha = 25^\circ$, a shadowing effect of the protuberances does not have to be taken into account.

The shadowing effect of the high harmonic beam becomes crucial especially for steep incidence angles close to the target normal where the laser light is blocked between the protuberances. This leads to a diminished emission close to the target surface for heights $h \geq 100$ nm.

The influence of the actual height of the protuberances on the angular emission is not very strong, as long as the preplasma scale length does not exceed the height h. In the simulations, the scale length L was very small (17 nm). For heights below the plasma scale length, the interference effect is negligible and the spectra look similar to the ones in figure 6.10 b) (red curve).

6.2.5 Influence of the angle of incidence

In order to study interaction geometries that were not experimentally accessible, different incidence and observation angles were simulated. Figure 6.12 shows the results of this parameter scan. In part a), the spectral distribution 90° with respect to the incoming laser beam is depicted. This corresponds to the experimental setup, where the angle between the spectrometer and the laser beam could not be changed. For incidence angles close to the target normal (3°, blue spectrum), the emission is almost shadowed by the target as

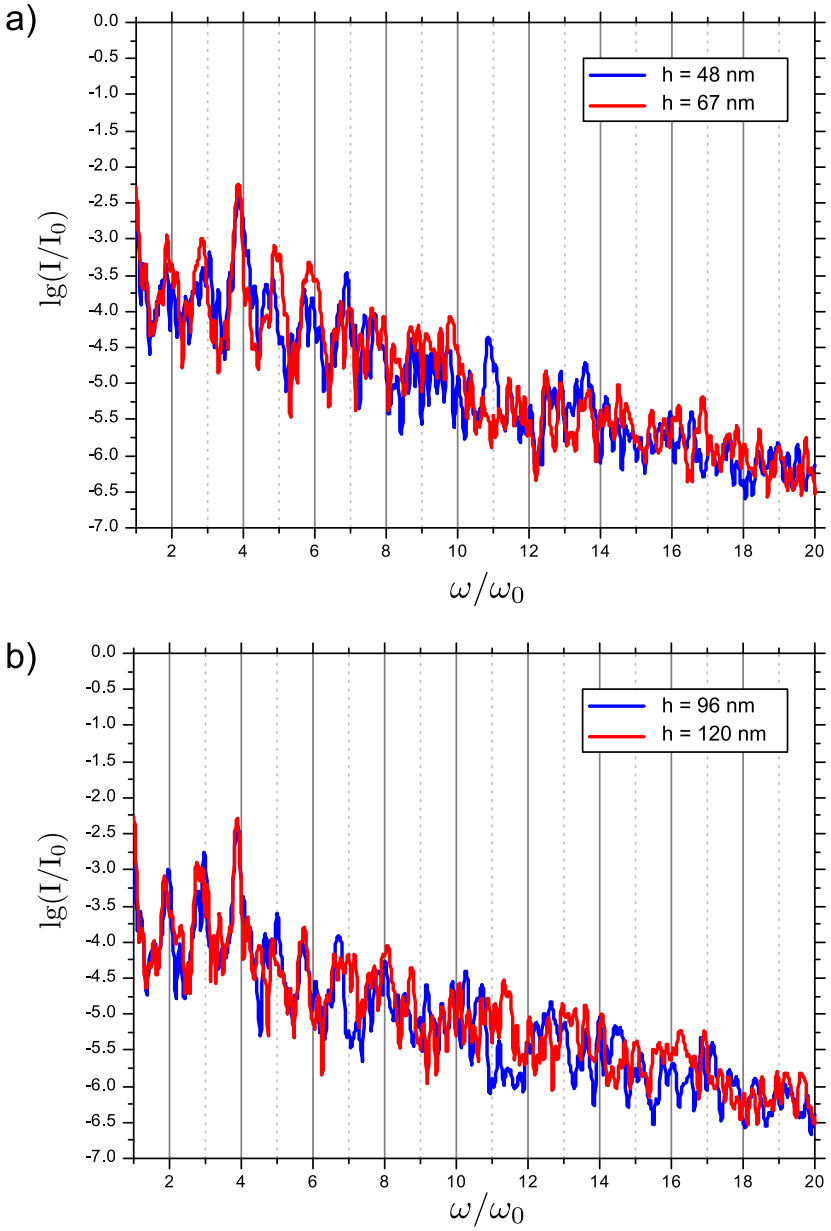

Figure 6.11: 2D EPOCH simulation results: Spectral distribution at $\alpha = 25^\circ$ for different heights of the protuberances h. The grating periodicity was 410 nm.

previously described. The harmonics are not resolved very well. By changing the incidence angle to 10°, several harmonic orders are emitted with higher efficiency than the rest (for example: 4^{th}, 5^{th}, 8^{th}–10^{th}, 12^{th}, 16^{th}, 17^{th}). At an incidence angle of 25°, the 5^{th}, 6^{th}, 8^{th}–13^{th} harmonic orders are efficiently generated (black spectrum).

The results for an observation angle which is close to the target surface (5°) are different, especially for the incidence angle of 3° (blue spectrum in figure 6.12 b)). Many harmonic orders are sharply resolved and also the higher orders (above order 35) are emitted with a rather high efficiency. The enhancement of the emission of only certain harmonics by applying other incidence angles (10° and 25°) is weaker close to the target surface than for the observation angle 90° with respect to the incoming laser beam.

Summarised, the simulation results for different incidence and the two observation angles indicate that the generation of very high-order harmonics along the target surface from corrugated targets is possible for incidence angles close to normal incidence. The incidence angle defines which harmonic orders are generated efficiently. By choosing a combination of incidence and observation angle, certain harmonics can be detected with higher or lower yield.

6.2.6 Summary: Low-order harmonics from corrugated targets

After investigating the harmonic generation from grating targets for different setups and over a broad parameter range, it becomes clear that the interplay between target geometry, laser wavefront curvature and interference properties of the grating lead to a rather complex spectral energy distribution. This effect is illustrated in figure 6.7. Even though the third harmonic was (at $\alpha = 25°$) obtained with a higher yield than the second order for the grating with $a = 480$ nm (figure 6.5 a)), it cannot be stated that the generation efficiency over the full angular distribution is higher. A tendency where which harmonic order can be found is defined by the interference formula.

Nevertheless, the actual spectral energy distribution crucially depends on the discussed interaction conditions, which are the focusing geometry of the laser, the preplasma scale length as well as the angle of incidence on the target. The stronger the denting effect during the interaction with the laser pulse is, the more deviations from the interference formula occur, as more incidence angles have to be taken into account. A very high laser intensity distributed on a small focal spot size with an intermediate contrast[2] leads to the

2 Preplasma scale length which exceeds the height of the protuberances.

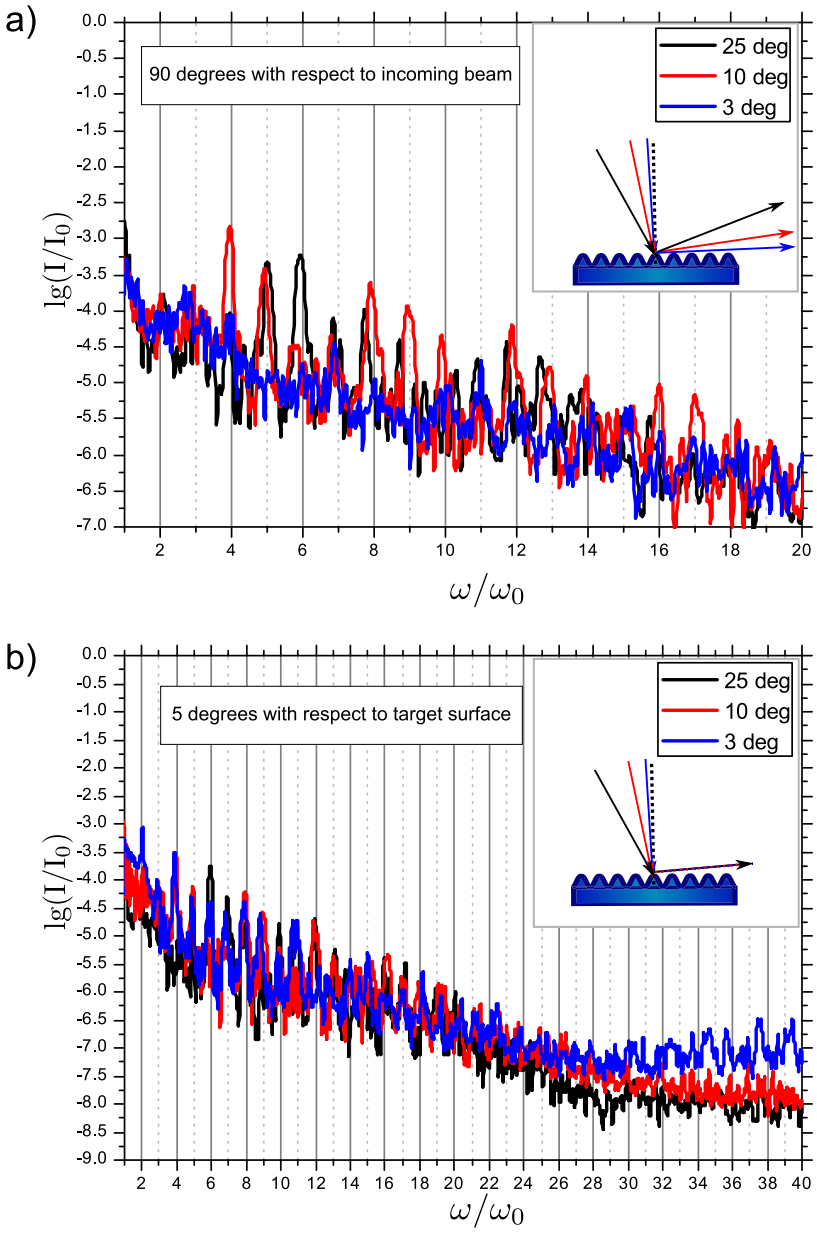

Figure 6.12: 2D EPOCH simulation results: Different angles of incidence on a grating with a periodicity of 250 nm.
a) Spectral distribution evaluated 90° with respect to the incoming laser (experimental condition).
b) Spectral distribution evaluated 5° with respect to the target surface.

destruction of the periodical structure of the target and thus to diminished interference properties of the gratings. It was found that the height of the protuberances does not change the spectral distribution (at $\alpha = 25°$) significantly, as long as the preplasma scale length is small. Nevertheless, for angles close to the target surface ($\alpha \leq 5°$), the emitted radiation is possibly blocked by the height of the protuberances.

By using grating targets, energy of certain harmonic orders is shifted apart from the specular direction of the laser and distributed over a larger angular range. The right choice of incidence angle, grating periodicity and laser contrast allows a selection of certain harmonic orders in particular emission directions. These properties make the usage of corrugated targets interesting for various applications. If blazed gratings are employed, the efficiency of steering a certain harmonic order into the first diffraction order of the grating can be increased [117].

6.3 Experimental results: XUV harmonics from corrugated targets

The second wavelength range which was investigated in the experiment, covered the range of 16–38 nm which corresponds to the harmonic orders 21–46. A flat-field XUV spectrometer was used to record the emitted radiation (see section 4.5.1). The spectrometer was mounted 5 ° with respect to the grating surface, which is 80 ° in relation to the specular direction of the laser. Three different kinds of targets were used in this experiment: two

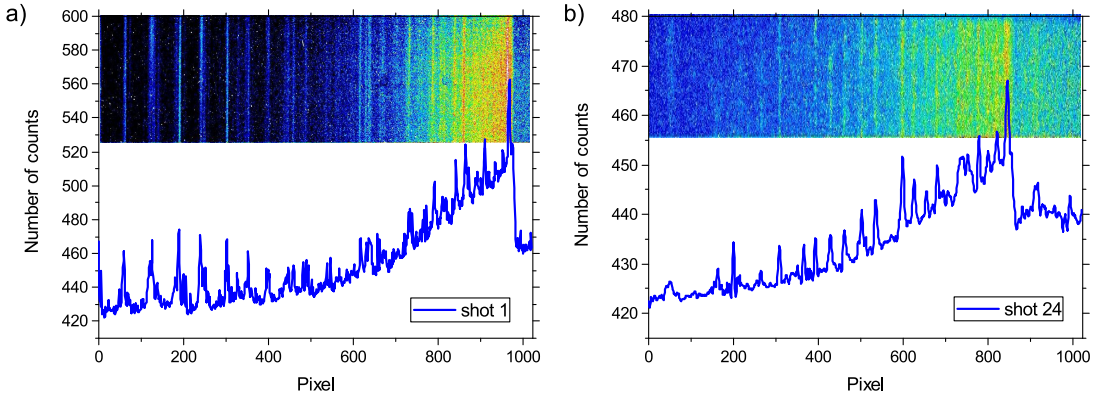

Figure 6.13: Raw spectra of the harmonics from grating targets recorded with the flat-field XUV spectrometer. The lineouts were integrated over the CCD chip.
a) Single shot spectrum obtained from grating G1 (a = 410 nm).
b) Single shot spectrum obtained from grating G2 (a = 250 nm).

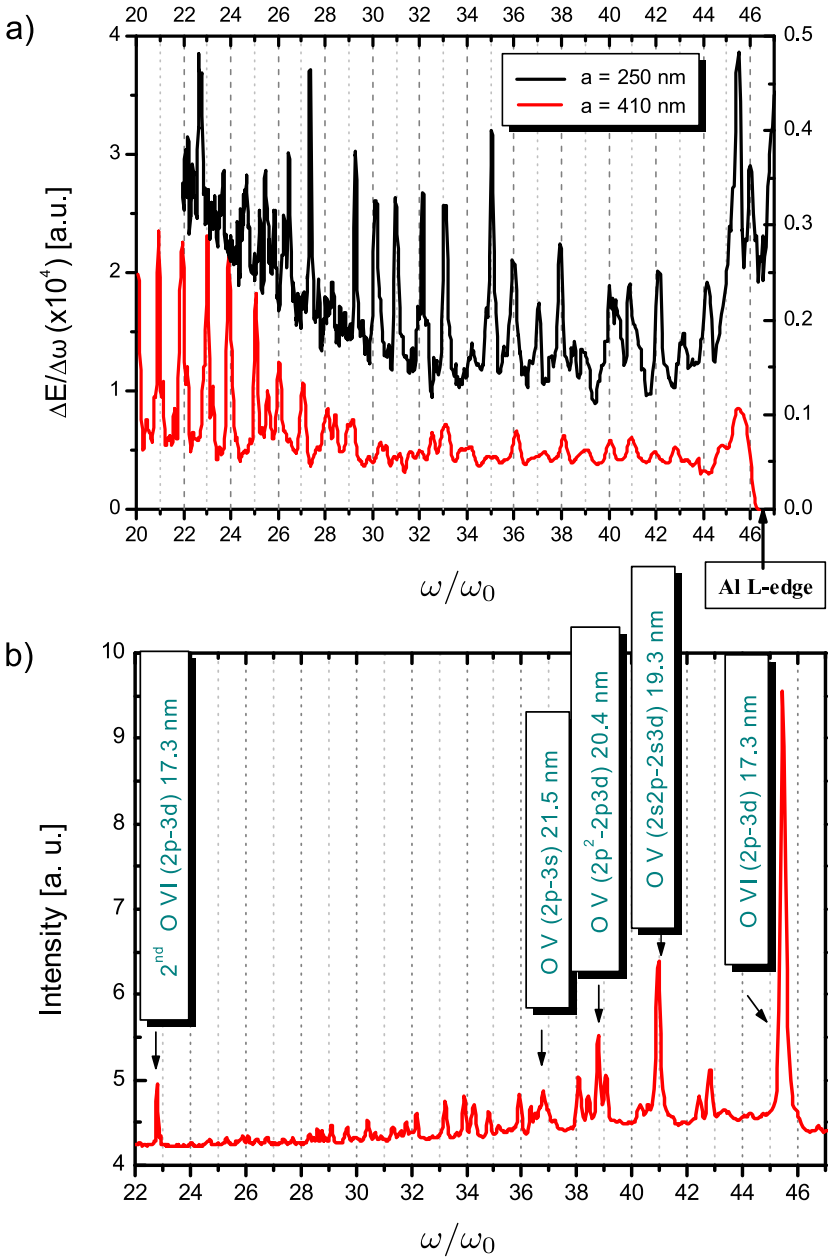

Figure 6.14: Spectra recorded with the XUV spectrometer. The spectra are corrected by including the spectral efficiency of the different components of the spectrometer and the quantum efficiency of the Andor CCD camera.
a) Harmonic spectra from two different gratings (G1 and G2) obtained under $\alpha = 5\,^\circ$ observation angle and $\theta = 5\,^\circ$ incidence angle.
b) Calibration spectrum with oxygen emission lines, obtained by slightly defocusing the laser.

	a	h	observation at 5°
G1	410 nm	70 nm	20^{th}- 25^{th} order harmonics
G2	250 nm	50 nm	29^{th}- 45^{th} order harmonics
flat	-	-	no harmonics (surface quality: $\lambda/20$)

Table 6.2: Targets used in the grating target experiment at 5° angle of incidence (XUV range) and overview of the obtained results at an observation angle of 5°.

gratings G1 and G2 and a flat target for comparison purposes (see table 6.2). The raw images which were recorded by the CCD camera, are shown in figure 6.13. The background level and the sharp aluminium L-edge can be seen.

The raw spectra were corrected by the spectral efficiency curve of the XUV spectrometer (figure 4.10 in section 4.5.1). The resulting spectra of the harmonics from grating G1 and G2 are depicted in figure 6.14 a). High-order harmonics are efficiently generated from G1 (with a periodicity of 410 nm) up to the order 25. The efficiency drops significantly for higher orders. Contrary to this, orders from 29 to 45 were detected with a higher yield for G2. It is remarkable that some harmonics are missing, as for example the 28^{th}, 34^{th} and 39^{th}.

No harmonics could be detected for wavelengths below the aluminium L-edge (17.1 nm), because a 200 nm thick aluminium filter was used to block any remaining light of the fundamental wavelength. Very close to the L-edge, a strong oxygen emission line (O VI - 17.3 nm) was identified. Calibration shots were taken with a defocused laser beam in order to record a plasma emission spectrum, which is shown in figure 6.14 b). In shots under the same conditions on flat targets with a surface quality of $\lambda/20$, no harmonics were observed at an angle of $\alpha = 5\,°$.

In agreement with the results of the MULTI-fs simulation (section 3.3.6), the structure of the grating surface still exists when the main pulse arrives at the target. By using the plasma mirror, the plasma scale length is $L \sim 30$ nm, which is smaller than the height of the protuberances. When changing the orientation of the grooves by 90 ° (perpendicular to the laser polarisation), no harmonics could be detected anymore. This is an indication that the interference properties contribute to the generation process. The experiment shows that high-order harmonics can be generated from grating targets, which do not necessarily need to have periodicities that are submultiples of the laser wavelength as reported in [15]. Each target type leads to a different composition of the generated harmonic spectrum.

6.4 Properties of the XUV grating harmonics from corrugated targets

According to the experimental results in the XUV range, a more complicated spectral distribution is obtained by the usage of corrugated targets compared to the high harmonic generation from flat targets. Several parameters influence the generation process in the XUV wavelength range which was also investigated by means of 2D PIC simulations. By employing the EPOCH simulation code, the effect of the grating periodicity in the setup configuration of the XUV experiment was studied. The simulation box was $19\lambda \times 24\lambda$ with a resolution of 250 cells/λ. The simulations in this subsection were done by Toma Toncian.

6.4.1 Influence of the grating periodicity

In figure 6.15, the results of the 2D PIC simulations are shown. The seven lines marked by circles in a) and c) are the interference orders n = 1–7 obtained from equation 2.55 ($\cos\alpha = \frac{n}{m}\frac{\lambda_0}{a} + \sin\theta$). Each circle stands for the prediction of a certain harmonic order emitted into a certain angular direction. By applying this simple formula, the harmonic spectrum of G2 (periodicity of a = 250 nm) close to the target surface ($\sim 85°$) should contain higher orders than the spectrum of G1 (a = 400 nm) at the same interference order. In the colour plots of a) and c), the intensity spectrogram for the harmonics over all possible observation angles (-5–95°) is depicted. The laser is incident at -5°, thus the specular direction is +5°. The observation axis of the experiment ($\alpha = 5°$) corresponds to an angle of 85° in these units.

The comparison of the spectrograms for G1 and G2 shows that for angles close to the target surface, higher harmonic orders are visible for the grating with $a = 250$ nm. For G1, the whole spectrum is shifted downwards towards the target normal (angle = 0°). This result is in agreement with the experimental observation where the higher order harmonics (> order 29) were only found close to the target surface for grating G2.

Part b) and d) of figure 6.15 illustrate the spectral distribution at 85 ° for both of the grating targets. The spectrum for G2 contains more gaps where the emission of certain harmonic orders is suppressed. The orders above 32 are not resolved due to the computational noise of the simulation. The visibility of higher orders is also diminished by the destruction (smoothing) of the grating target during the duration of the laser pulse. The smoothing of the target during the reflection of the laser pulse can be seen i. e. in figure 6.4 and 6.9.

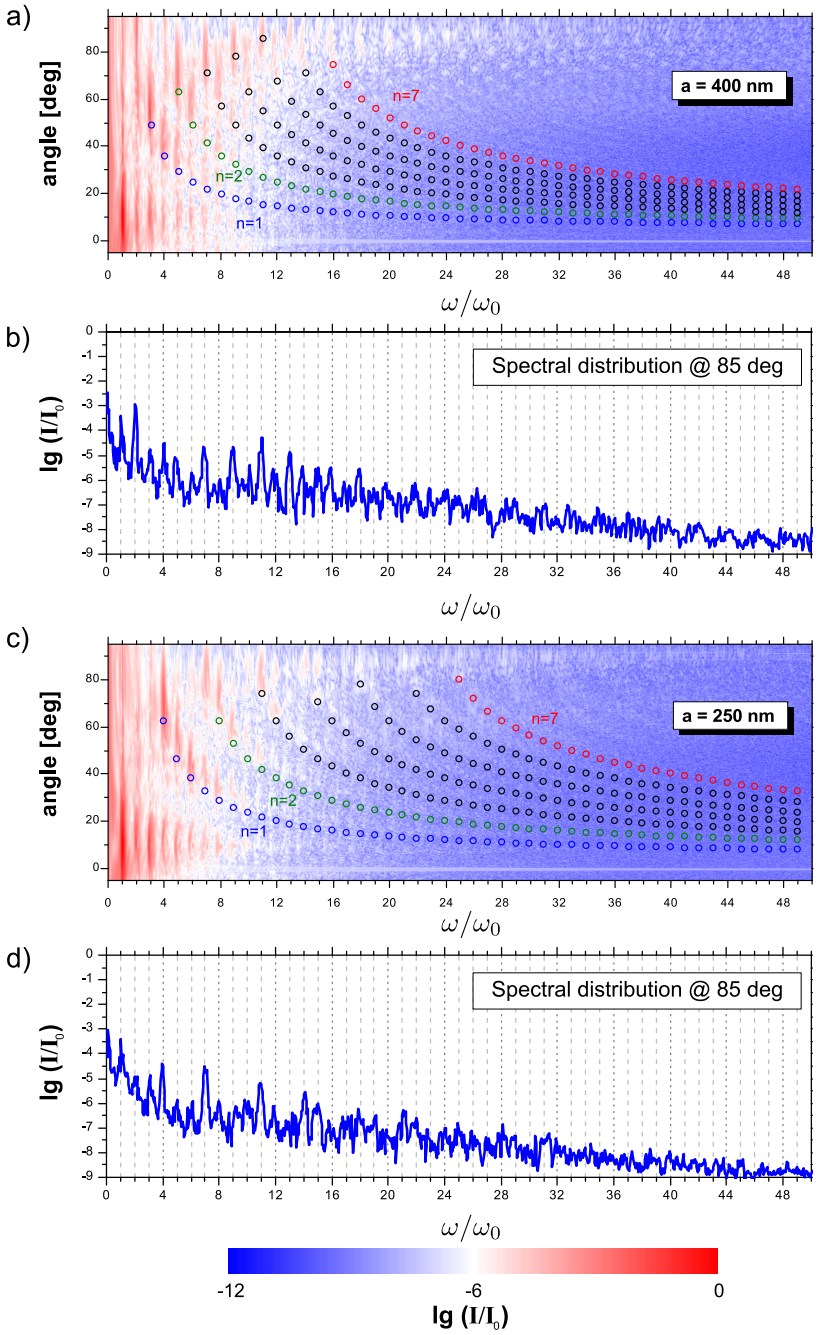

Figure 6.15: Results of the 2D PIC simulation: **a) + c)** Time-integrated spectra over an angular range of 100° for G1 and G2. The spectral relative intensity is shown as a function of harmonic order and emission angle. In the simulations, the incidence angle is at -5°, the specular axis is at +5° and the observation axis of the experiment corresponds to an angle of 85°. The emission angles of the harmonics given by equation 2.55 are marked by circles for seven consecutive orders.
b) + d) Harmonic spectra at 85° for G1 and G2.

6.4.2 Influence of the focusing angle

Two effects which are inherent in a tightly focused laser beam, influence the angular distribution of the spectra. Firstly, the surface is dented locally due to the light pressure of the high intensity laser pulse. The electrons are pushed into the target. In EPOCH simulations, the displacement Δx of the electron surface reached up to 400 nm. Secondly, not only one incidence angle can be defined for an intense focused laser beam because of the curvature of the wavefronts. This results in an angular broadening of the high harmonic emission, as many incidence angles contribute to the resulting spectrum.

Both effects are schematically shown in figure 6.16 a) and b). If the target is placed exactly in the focus, the curvature of the wavefronts is negligible (see figure 6.16 a)) and the angle β is zero. β varies around $\pm$ 5 °, as it is only possible to put the target in focus by the precision of $\pm$ the Rayleigh length in experiments, which is $z_R = 12.5\,\mu$m for the typically used short focal length f/2 off-axis parabolic mirrors.

In order to study the influence of the focusing angle of the laser beam on the high harmonic generation, 2D PIC simulations using the **P**lasma **S**imulation **C**ode (PSC) [172] were performed. The simulation box of 6 x 6 µm had a resolution of 240 cells/µm. The ionisation rates were computed by applying the ADK rates.

In these simulations, the laser pulses were focused onto the grating targets with a = 250 nm with different far field angles ($\beta = 0$–$13°$). The angle of incidence θ and the observation angle α both were 5°. For plane waves ($\beta = 0$), the spectrum contains many gaps and only a few harmonics are emitted. The effect of the wavefront curvature on the high harmonic spectra is illustrated in figure 6.17. The stronger the wavefront curvature is, the more harmonics appear on the observation axis ($\alpha = 5°$).

For $\beta = 4.5°$, the efficiency of the high harmonic radiation at the observation angle is

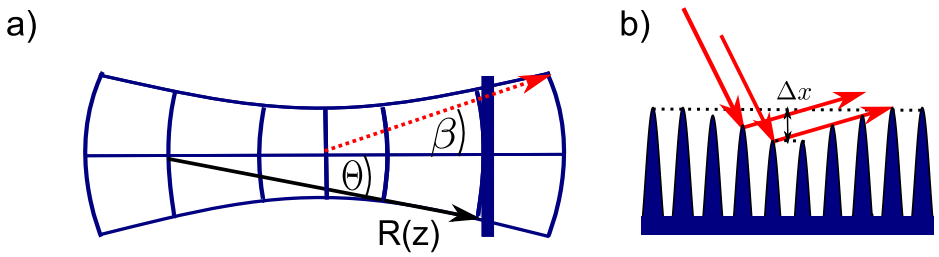

Figure 6.16: Effect of the interaction geometry of a focused laser beam
a) Wavefront curvature of a Gaussian beam.
b) Schematic representation of the surface denting due to the ponderomotive force.

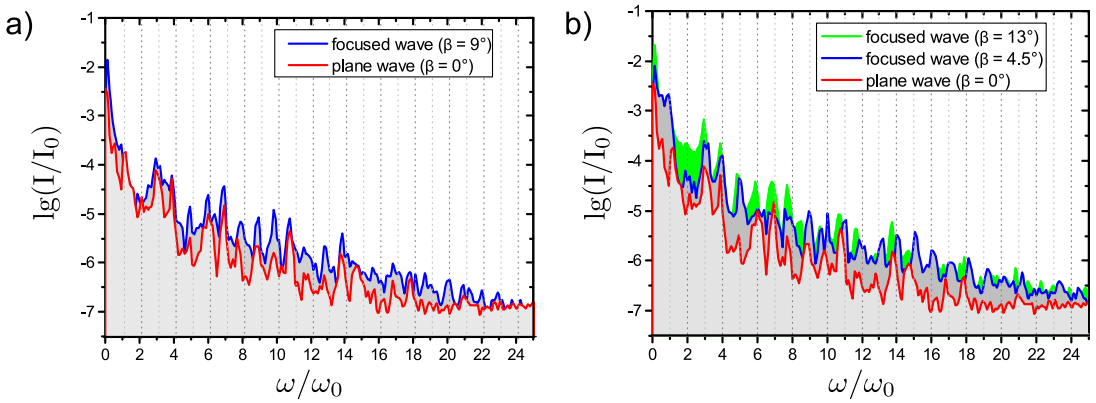

Figure 6.17: Effect of the interaction geometry of a focused laser beam. Simulation results of 2D PIC simulations obtained with PSC code: High harmonic spectra at the observation axis of $\alpha = 5°$ for plane wave in comparison with different focusing angles $\beta = 4.5°$, 9° and 13°.

higher than for the plane wave case. The strongest focusing with $\beta = 13°$ leads to an even more intense generation of harmonics in the observation direction.

The results demonstrate the possibility of controlling the composition of the high harmonic spectra by changing the grating periodicity. The spectrograms indicate that lower-order harmonics are emitted mainly close to the specular direction of the laser. Higher-order harmonics are predominantly found along the target surface (especially for G2), hence largely separated from the fundamental laser light which is beneficial for many kinds of applications.

6.5 Conclusions: Harmonics from grating targets

In this chapter, harmonic generation from different periodically modulated targets was studied over a broad wavelength range. Experimental observations were confirmed and sustained by 2D PIC simulations. The influence of the grating periodicity on the spectral distribution is supported by the simulation results. Effects like wavefront curvature and denting of the surface also play a crucial role.

The lower-order harmonics are emitted mainly in the specular direction of the laser light (for 5° incidence angle), whereas high-order harmonics are more present close to the target surface. Constructive interference through superposition of the generated waves leads to the occurrence of this effect.

The efficiency of the grating harmonics was compared to the conventional generation

method of high harmonics from targets at 45 °. Experiments investigating the generation of high harmonics from flat targets were conducted at the ARCTURUS laser facility previously. In these experiments, the high harmonic emission was recorded along the specular direction of the laser by using an XUV imaging spectrometer [10]. Harmonics were detected up to the 40^{th} order. In order to compare the high harmonic emission by the two methods (grating and flat targets), the spectral energy distribution (in J/Hz/sr) was deduced from the raw spectra. After correcting the experimental spectra for the spectrometers' efficiency, the CCD cameras' gain and the acceptance angle of the spectrometers, the spectral energy distribution of the flat target along the specular direction was determined to be 2–3 orders of magnitudes higher than in case of grating targets (at $\theta = 5°$ and $\alpha = 5°$).

These results are not surprising and can be understood by considering the particularities of the generation process on grating targets. Due to the interference properties of the grating, the harmonics are distributed over a larger angular range. Moreover, for grating targets with a sinusoidal profile as used in the experiment, the laser beam is incident under variable angles along the emitting protuberance surface and thereby reduces the efficiency of the process. In reference [15], it was also found that surface modulations with a $\sin^2$-profile lead to a lower efficiency of the harmonics compared to a grating structure with a rectangular profile. As different absorption processes contribute to the coupling of laser and target at angles close to normal incidence (chapter 2.3), the energy absorption is less efficient than for oblique incidence. It should be clearly stated that a direct comparison of the energy conversion efficiency for grating and flat targets requires a measurement of the divergence of the harmonic beam. Experimentally, the acceptance angle of the spectrometer was too small compared to the expected beam divergence and no angular distribution could be estimated from the spectra.

Although grating harmonics do not provide an enhancement in terms of efficiency, they offer the opportunity of usage for further applications without the need for strong filtering of the specular light due to their spread over a larger angular distribution.

The emission of lower-order harmonics for an incidence angle of 25° was studied in detail, and the relevant influences on the generation process were emphasised. Especially the focusing geometry determines the spectral energy distribution of the emitted radiation. Small focal spot sizes in combination with high laser intensities lead to strong deviations from the angular distribution predicted by the analytical model of interference. It was also demonstrated that without a small plasma scale length as obtained by using a plasma mirror, harmonics from grating targets would not be efficiently generated in directions apart from the specular direction. The results of both, simulation and experiment for the gratings G3 and G4, showed that the emission efficiency of certain low-order harmonics at a distinct

observation angle can be regulated by changing the periodicity of the grating target. These results can be adapted for different grating types insofar as for a certain harmonic order, a suitable generation setup with grating targets can be found.

Summarised, the studied effects indicate a possible control of the composition of the harmonic spectra by adjusting the focusing angle and modifying the grating target parameters.

7 Summary and conclusion

The interaction of ultrashort laser pulses with gaseous and solid targets was studied in two intensity regimes. A high temporal laser contrast as the connecting link between the two experiments is important to enable the analysis of the interaction processes without the strong influence of preplasma effects.

A plasma mirror system was designed, built and characterised in order to allow experiments with thin or structured targets with the ARCTURUS laser. By using the plasma mirror, experiments with ultra-high contrast (10^{-11} on 100 ps time scale) can be performed at the ARCTURUS laser facility. The plasma mirror system has a high energy throughput of 80 %. This allows to study interaction regimes with high-power relativistic ultrashort laser pulses. Since more facilities world-wide use laser systems reaching intensities of $\geq 10^{18}\,\mathrm{W/cm^2}$ in the focal spot, the knowledge of the temporal contrast is of great importance. By changing the reflectivity of the plasma mirror substrates, the temporal contrast of the laser pulse and thus the preplasma conditions can be adjusted to the experimental needs. Especially the high harmonic generation from solid surfaces benefits from these controllable contrast conditions. Also future experiments can make essential use of the installed plasma mirror system, as for example experiments with cluster targets or targets with small surfaces (i.e. nanowire targets), two beam experiments with incidence angles close to the target normal, Thomson backscattering from thin (several nanometer thick) foils or the relativistically flying mirror.

The investigation of the propagation dynamics of the laser pulse in three different noble gases showed that the neutral particle density crucially influences the spectral phase of the laser pulse. The results are relevant for understanding the laser pulse interaction dynamics during the generation process of high harmonics in gaseous targets. As the second-order dispersion varies during the propagation, the laser pulse changes its properties which can affect the harmonic generation process. The experiment revealed that in case of the helium gas jet, the second-order dispersion coefficient D_2 passes through negative values for lower neutral particle densities and becomes positive with rising gas pressure. The studies of the interaction between the laser pulse and the three examined noble gases (helium, neon and argon) demonstrated that the different ionisation thresholds significantly change the

spectral phase of the laser pulse. Since argon has the lowest ionisation potential out of the three gases, the interaction with the argon gas jet leads to the strongest changes of the spectral phase. An FDTD simulation showed that the behaviour of the D_2 coefficient is strongly intensity-dependent.

Furthermore, the influence of the ionisation process on the laser pulse was investigated by means of 2D PIC simulations. The numerical analysis of these interactions is very complex as in this intensity regime, many different effects occur. Especially the uncertainty of the input parameters (i.e. initial chirp of the laser pulse) complicates the simulation conditions. As different numerical models set their focus on different properties of the interaction, a full description of the influence of the gas pressure on the spectral phase of the laser pulse remains unresolved. Nevertheless, during the propagation of the laser pulse through the gas jet, pulse shortening was observed in the simulations. In order to make use of this effect in the experiment, a shorter gas jet would be necessary. By applying a suitable gas jet target, this plasma compression method would be useful for future high power laser systems.

In the second main experiment, harmonic emission from periodically modulated target surfaces was investigated in two wavelength regimes. Firstly, the emission of low-order harmonics (2^{nd} and 3^{rd}) from grating targets was detected under an angle of 25° with respect to the target surface for an angle of incidence of 25° (with respect to the target normal). At this observation angle, the third harmonic was recorded with a higher yield than the second order for one of the grating targets. Modifications of the focal spot size and thereby the illumination of more or less grating protuberances, lead to an enhancement of different orders. If more grooves are irradiated, more interference orders contribute to the resulting spectrum and the interference effect dominates the harmonic emission.

2D PIC simulations illustrated that the emission of the low-order harmonics can be controlled by parameters like grating periodicity, laser contrast and incidence angle. By using grating targets, certain low-order harmonics can be either emitted with a higher or lower yield. Hence, grating targets are perfectly suitable for achieving specific harmonic orders.

Moreover, the first demonstration of high harmonic generation from grating targets along the target surface was reported in this thesis. An incidence angle of 5° with respect to the target normal led to an emission of harmonics up to the 45^{th} order at an observation angle of 5° (with respect to the target surface). The properties of these grating harmonics were studied intensively with the help of 2D PIC simulations. It was found that certain harmonic orders can be emitted with higher efficiency by choosing the right combination of grating periodicity, laser contrast, focusing angle of the laser and observation angle. An estimation of the spectral distribution of the harmonics for larger spot sizes is given by the interference formula for a diffraction grating. According to this formula, only certain

harmonic orders can be expected to be emitted at a distinct observation angle and the harmonic spectrum contains large gaps. Nevertheless, by changing the focusing geometry of the laser or the preplasma scale length, also other harmonic orders are emitted more intensively. The strong curvature of the wavefronts caused by using an off-axis parabolic mirror with a short focal length (i. e. f/2), leads to many different incidence angles on the target and thus to deviations in the angular distribution of the generated harmonic spectra from the interference formula.

The setup of the grating harmonic experiments provides a source of high harmonics apart from the specular direction of the laser. Although the laser energy is never entirely absorbed by the target, this setup allows to omit strong filters for the fundamental wavelength, since the harmonic observation direction is largely separated from the specular direction. This new generation method makes an important step forward towards controlling the spectral distribution of the emitted harmonics which is of great interest for the feasibility of single attosecond pulses.

The two main experiments presented in this thesis demonstrated opportunities of further compression of short laser pulses by the propagation dynamics in gases or the frequency conversion during the interaction with grating targets. Both techniques are interesting for future highest-power laser systems reaching intensities in the ultra-relativistic regime (see i. e. the **E**xtreme **L**ight **I**nfrastructure (ELI) and the IZEST project [173]).

Bibliography

[1] A. L. Cavalieri, N. Müller, Th. Uphues, V. S. Yakovlev, A. Baltuska, B. Horvath, Schmidt, L. Blümel, R. Holzwarth, S. Hendel, M. Drescher, U. Kleineberg, P. M. Echenique, R. Kienberger, F. Krausz, and U. Heinzmann.
Attosecond spectroscopy in condensed matter.
nature, 449:1029–1032, 2007.

[2] A. Föhlisch, P. Feulner, F. Hennies, A. Fink, D. Menzel, D. Sanchez-Portal, P. M. Echenique, and W. Wurth.
Direct observation of electron dynamics in the attosecond domain.
nature, 436:373–376, 2005.

[3] M. Drescher, M. Hentschel, R. Kienberger, G. Tempea, C. Spielmann, G. A. Reider, P. B. Corkum, and F. Krausz.
X-ray pulses approaching the attosecond frontier.
Science, 291:1923–1927, 2001.

[4] P. M. Paul, E. S. Toma, P. Breger, G. Mullot, F. Auge, Ph. Balcou, H. G. Muller, and P. Agostini.
Observation of a train of attosecond pulses from high harmonic generation.
Science, 292:1689–1692, 2001.

[5] M. Hentschel, R. Kienberger, Ch. Spielmann, G. A. Reider, N. Milosevic, T. Brabec, P. Corkum, U. Heinzmann, M. Drescher, and F. Krausz.
Attosecond metrology.
nature, 414:509–513, 2001.

[6] C. Bostedt, E. Eremina, D. Rupp, M. Adolph, H. Thomas, M. Hoener, A. R. B. de Castro, J. Tiggesbäumker, K.-H. Meiwes-Broer, T. Laarmann, H. Wabnitz, E. Plönjes, R. Treusch, J. R. Schneider, and T. Möller.
Ultrafast x-ray scattering of xenon nanoparticles: Imaging transient states of matter.
Phys. Rev. Lett., 108:093401, Feb 2012.

[7] H. N. Chapman.
Femtosecond x-ray protein nanocrystallography.
Nature, 470:73–78, 2011.

[8] S. V. Bulanov, N. M. Naumova, and F. Pegoraro.

Interaction of an ultrashort, relativistically strong laser pulse with an overdense plasma.
Phys. Plasmas, 1,3:745–757, 1994.

[9] P. A. Norreys, M. Zepf, S. Moustaizis, A. P. Fews, J. Zhang, P. Lee, M. Bakarezos, C. N. Danson, A. Dyson, P. Gibbon, P. Loukakos, D. Neely, F. N. Walsh, J. S. Wark, and A. E. Dangor.
Efficient extreme uv harmonics generated from picosecond laser pulse interactions with solid targets.
Phys. Rev. Lett., 76:1832–1835, Mar 1996.

[10] M. Behmke, D. an der Brügge, C. Rödel, M. Cerchez, D. Hemmers, M. Heyer, O. Jäckel, M. Kübel, G. G. Paulus, G. Pretzler, A. Pukhov, M. Toncian, T. Toncian, and O. Willi.
Controlling the spacing of attosecond pulse trains from relativistic surface plasmas.
Phys. Rev. Lett., 106:185002, May 2011.

[11] C. Thaury and F. Quere.
High-order harmonic and attosecond pulse generation on plasma mirrors basic mechanisms.
Journal of Physics B, 43:213001, 2010.

[12] S. G. Rykovanov, M. Geissler, J. Meyer ter Vehn, and G. D. Tsakiris.
Intense single attosecond pulses from surface harmonics using the polarization gating technique.
New Journal of Physics, 10:025025, 2008.

[13] L. Poletto, F. Frassetto, and P. Villoresi.
Design of an extreme-ultraviolet attosecond compressor.
JOSA B, 25,7:133–136, 2008.

[14] A. Tarasevitch, J. Wieczorek, R. Kohn, U. Bovensiepen, and D. von der Linde.
Two-beam high-order harmonics from solids: Coupling mechanisms.
Phys. Rev. E, 82:056410, Nov 2010.

[15] X. Lavocat-Dubuis and J.-P. Matte.
Numerical simulation of harmonic generation by relativistic laser interaction with a grating.
PHYSICAL REVIEW E, 80:1–4, 2009.

[16] X. Lavocat-Dubuis and J.-P. Matte.
Numerical and theoretical study of the generation of extreme ultraviolet radiation by relativistic laser interaction with a grating.
Physics of Plasmas, 17:093105–1–093105–12, 2010.

[17] V.Kh. Liechtenstein, T.M. Ivkova, E.D. Olshanski, R. Golser, W. Kutschera, P. Steier, C. Vockenhuber, R. Repnow, R. von Hahn, M. Friedrich, and U. Kreissig.

Recent investigations and applications of thin diamond-like carbon (dlc) foils.
Nuclear Instruments and Methods in Physics Research A, 521:197–202, 2004.

[18] D. Kiefer, A. Henig, D. Jung, D.C. Gautier, K.A. Flippo, S.A. Gaillard, S. Letzring, R.P. Johnson, R.C. Shah, T. Shimada, J.C. Fernandez, V.Kh. Liechtenstein, J. Schreiber, B.M. Hegelich, , and D. Habs.
First observation of quasi-monoenergetic electron bunches driven out of ultra-thin diamond-like carbon (dlc) foils.
Eur. J. Phys., 55:427–432, 2009.

[19] Siegfried H. Glenzer and Ronald Redmer.
X-ray thomson scattering in high energy density plasmas.
Rev. Mod. Phys., 81:1625–1663, Dec 2009.

[20] M. Kando, Y. Fukuda, A. S. Pirozhkov, J. Ma, I. Daito, L.-M. Chen, T. Zh. Esirkepov, K. Ogura, T. Homma, Y. Hayashi, H. Kotaki, A. Sagisaka, M. Mori, J. K. Koga, H. Daido, S. V. Bulanov, T. Kimura, Y. Kato, and T. Tajima.
Demonstration of laser-frequency upshift by electron-density modulations in a plasma wakefield.
Phys. Rev. Lett., 99:135001, Sep 2007.

[21] M. Kando, A. S. Pirozhkov, K. Kawase, T. Zh. Esirkepov, Y. Fukuda, H. Kiriyama, H. Okada, I. Daito, T. Kameshima, Y. Hayashi, H. Kotaki, M. Mori, J. K. Koga, H. Daido, A. Ya. Faenov, T. Pikuz, J. Ma, L.-M. Chen, E. N. Ragozin, T. Kawachi, Y. Kato, T. Tajima, and S. V. Bulanov.
Enhancement of photon number reflected by the relativistic flying mirror.
Phys. Rev. Lett., 103:235003, Dec 2009.

[22] A. P. L. Robinson, M. Zepf, S. Kar, R. G. Evans, and C. Bellei.
Radiation pressure acceleration of thin foils with circularly polarized laser pulses.
New Journal of Physics, 10:013021, 2008.

[23] B. Qiao, M. Zepf, M. Borghesi, B. Dromey, M. Geissler, A. Karmakar, and P. Gibbon.
Radiation-pressure acceleration of ion beams from nanofoil targets: The leaky light-sail regime.
Phys. Rev. Lett., 105:155002, Oct 2010.

[24] R. Prasad, A. A. Andreev, S. Ter-Avetisyan, D. Doria, K. E. Quinn, L. Romagnani, C. M. Brenner, D. C. Carroll, N. P. Dover, D. Neely, P. S. Foster, P. Gallegos, J. S. Green, P. McKenna, Z. Najmudin, C. A. J. Palmer, J. Schreiber, M. J. V. Streeter, O. Tresca, M. Zepf, and M. Borghesi.
Fast ion acceleration from thin foils irradiated by ultra-high intensity, ultrahigh contrast laser pulses.
Appl. Phys. Lett., 99:121504, 2011.

[25] M. Göppert-Mayer.

Elementary processes with two-quantum transitions.
Annalen der Physik, 9:273, 1931.

[26] W. Kaiser and C. G. B. Garrett.
Two-photon excitation in CaF^2Eu^{2+}.
Phys. Rev. Lett., 7:229–231, Sep 1961.

[27] P. Agostini, G. Barjot, J. Bonnal, G. Mainfray, C. Manus, and J. Morellec.
Multiphoton ionization of hydrogen and rare gases.
Quantum Electronics, IEEE Journal of, 4(10):667 – 669, oct 1968.

[28] J. H. Eberly and J. Javanainen.
Above-threshold ionisation.
Eur. J. Phys., 9:265–275, 1988.

[29] L. V. Keldysh.
Ionisation in the field of a strong electromagnetic wave.
JETP, 20:1307, 1965.

[30] E. Mevel, P. Breger, R. Trainham, G. Petite, P. Agostini, A. Migus, J.-P. Chambaret, and A. Antonetti.
Atoms in strong optical fields: Evolution from multiphoton to tunnel ionization.
Phys. Rev. Lett., 70:406–409, Jan 1993.

[31] S. Augst, D. D. Meyerhofer, D. Strickland, and S. L. Chint.
Laser ionization of noble gases by coulomb-barrier suppression.
JOSA B, 8:858–867, 1991.

[32] D. Bauer and P. Mulser.
Exact field ionization rates in the barrier-suppression regime from numerical time-dependent schrödinger-equation calculations.
Physical Review A, 59:569–577, 1999.

[33] P. Gibbon.
Short-pulse Laser interaction with matter.
Imperial College Press, 2005.

[34] M. V. Ammosov, N.B. Delone, and V. P. Krainov.
Tunnel ionization of complex atoms and of atomic ions in an alternating electromagnetic field.
Sov. Phys. JETP, 64:1191, 1986.

[35] S. Augst, D. Strickland, D. D. Meyerhofer, S. L. Chin, and J. H.Eberly.
Tunneling ionization of noble gases in a high-intensity laser field.
Phys. Rev. Lett., 63:2212–2215, Nov 1989.

[36] S. F. J. Larochelle, A. Talebpour, and S. L. Chin.
Coulomb effect in multiphoton ionization of rare-gas atoms.
Journal of Physics B, 31:1215–1224, 1997.

[37] F. A. Ilkov, J. E. Decker, and S. L. Chin.
Ionization of atoms in the tunnelling regime with experimental evidence using hg atoms.
Journal of Physics B, 25:4005, 1992.

[38] M. Uiberacker, Th. Uphues, M. Schultze, A. J. Verhoef, V. Yakovlev, M. F. Kling, J. Rauschenberger, N. M. Kabachnik, H. Schröder, M. Lezius, K. L. Kompa, H.-G. Muller, M. J. J. Vrakking, S. Hendel, U. Kleineberg, U. Heinzmann, M. Drescher, and F. Krausz.
Attosecond real-time observation of electron tunnelling in atoms.
Nature, 446:627–632, 2007.

[39] A. M. Perelomov, V. S. Popov, and M. V. Terent'ev.
Ionization of atoms in an alternating electric field.
JETP, 23:924, 1966.

[40] M. Chen, E. Esarey, C. B. Schroeder, C. G. R. Geddes, and W. P. Leemans.
Theory of ionization-induced trapping in laser-plasma accelerators.
Physics of Plasmas, 19:033101, 2012.

[41] E. S. Efimenko, A. V. Kim, and M. Quiroga-Teixeiro.
Ionization-induced small-scaled plasma structures in tightly focused ultrashort laser pulses.
Phys. Rev. Lett., 102:015002, Jan 2009.

[42] A. A. Andreev, K. Y. Platonov, and J.C. Gauthier.
Skin effect in strongly inhomogeneous laser plasmas with weakly anisotropic temperature distribution.
Physical Review E, 58,2:2424–2430, 1998.

[43] T. Nakamura, S. Kato, and T. Kato.
Anomalous skin effect for linearly and circularly polarized intense laser light.
Laser and Particle Beams, 20:101–107, 2002.

[44] T. Y. B. Yang, William L. Kruer, A. B. Langdon, and T. W. Johnston.
Mechanisms for collisionless absorption of light waves obliquely incident on overdense plasmas with steep density gradients.
Physics of Plasmas, 3,7:2702–2709, 1996.

[45] W. L. Kruer.
The physics of laser plasma interactions.
Westview Press, 2003.

[46] S. Eliezer.
The interaction of high-power lasers with plasmas.
Institute of Physics, 2002.

[47] C. Garban-Labaune, E. Fabre, C. E. Max, R. Fabbro, F. Amiranoff, J. Virmont, M. We-

infeld, and A. Michard.
Effect of laser wavelength and pulse duration on laser-light absorption and back reflection.
Phys. Rev. Lett., 48:1018–1021, Apr 1982.

[48] T.-Y. Brian Yang, William L. Kruer, Richard M. More, and A. Bruce Langdon.
Absorption of laser light in overdense plasmas by sheath inverse bremsstrahlung.
Phys. Plasmas, 2:3146, 1995.

[49] P. J. Catto and R. M. More.
Sheath inverse bremsstrahlung in laser produced plasmas.
Phys. Fluids, 20:704–705, 1977.

[50] L. M. Chen, J. Zhang, Q. L. Dong, H. Teng, T. J. Liang, L. Z. Zhao, and Z. Y. Wei.
Hot electron generation via vacuum heating process in femtosecond laser solid interactions.
Phys. Plasmas, 8:2925–2929, 2001.

[51] J. M. Bennett.
Handbook of optics Volume I.
McGraw-Hill, INC, 1995.

[52] W. Rozmus and V. T. Tikhonchuk.
Skin effect and interaction of short laser pulses with dense plasmas.
Phys. Rev. A, 42:7401–7412, Dec 1990.

[53] D. W. Forslund, J. M. Kindel, Kenneth Lee, E. L. Lindman, and R. L. Morse.
Theory and simulation of resonant absorption in a hot plasma.
Phys. Rev. A, 11:679–683, Feb 1975.

[54] G. J. Pert.
The analytic theory of linear resonant absorption.
Plasma Phys., 20:175–188, 1978.

[55] P. Gibbon.
Short-pulse laser plasma interactions.
Plasma Phys. Control. Fusion, 38:769–793, 1996.

[56] F. Brunel.
Not so resonant, resonant absorption.
Physical Review Letters, 59,1:52–55, 1987.

[57] P. Gibbon.
Collisionless absorption in sharp-edged plasmas.
Physical Review Letters, 68,10:1535–1539, 1992.

[58] Y. Ping, R. Shepherd, B. F. Lasinski, M. Tabak, H. Chen, H. K. Chung, K. B. Fournier, S. B. Hansen, A. Kemp, D. A. Liedahl, K. Widmann, S. C. Wilks, W. Rozmus, and M. Sherlock.

Absorption of short laser pulses on solid targets in the ultrarelativistic regime.
Phys. Rev. Lett., 100:085004, Feb 2008.

[59] Y. Ping, A. J. Kemp, L. Divol, M. H. Key, P. K. Patel, K. U. Akli, F. N. Beg, S. Chawla, C. D. Chen, R. R. Freeman, D. Hey, D. P. Higginson, L. C. Jarrott, G. E. Kemp, A. Link, H. S. McLean, H. Sawada, R. B. Stephens, D. Turnbull, B. Westover, and S. C. Wilks.
Dynamics of relativistic laser-plasma interaction on solid targets.
Phys. Rev. Lett., 109:145006, Oct 2012.

[60] W. L. Kruer and K. Estabrook.
Jxb heating by very intense laser light.
Phys. Fluids, 28:430–432, 1985.

[61] H. Cai, W. Yu, S. Zhu, and C. Zheng.
Short-pulse laser absorption via jxb heating in ultrahigh intensity laser plasma interaction.
Phys. Plasmas, 13:113105, 2006.

[62] Frank Träger, editor.
Springer Handbook of Lasers and Optics.
Springer, 2007.

[63] W. R. Boyd.
Nonlinear Optics.
Academic Press, 2003.

[64] C. Brée, A. Demircan, and G. Steinmeyer.
Saturation of the all-optical kerr effect.
Phys. Rev. Lett., 106:183902, May 2011.

[65] G. P. Agrawal.
Nonlinear Fiber Optics.
Academic Press Limited, 2001.

[66] C. E Max, J. Arons, and A. B. Langdon.
Self-modulation and self-focusing of electromagnetic waves in plasmas.
Phys. Rev. Lett., 33:209–212, Jul 1974.

[67] C. E. Max.
Strong self focusing due to the ponderomotive force in plasmas.
19,1:74–77, 1976.

[68] G. Zheng Sun, E. Ott, Y. C. Lee, and P. Guzdar.
Selffocusing of short intense pulses in plasmas.
Phys. Fluids, 30:526, 1987.

[69] I. Watts, M. Zepf, E. L. Clark, M. Tatarakis, K. Krushelnick, A. E. Dangor, R. Allott, R. J. Clarke, D. Neely, and P. A. Norreys.

Measurements of relativistic self-phase-modulation in plasma.
Phys. Rev. E, 66:036409, Sep 2002.

[70] T. Auguste, P. Monot, L.-A. Lompre, G. Mainfray, and C. Manus.
Defocusing effects of a picosecond terawatt laser pulse in an underdense plasma.
Optics Communications, 89(2,4):145 – 148, 1992.

[71] S. C. Rae.
Spectral blueshifting and spatial defocusing of intense laser pulses.
Optics Communications, 104:330–335, 1994.

[72] S. C. Rae.
Ionization-induced defocusing of intense laser pulses in high-pressure gases.
Optics Communications, 97:25–28, 1993.

[73] W. P. Leemans, C. E. Clayton, W. B. Mori, K. A. Marsh, P. K. Kaw, A. Dyson, C. Joshi, and J. M. Wallace.
Experiments and simulations of tunnel-ionized plasmas.
Phys. Rev. A, 46:1091–1105, Jul 1992.

[74] J. R. Marques R. Bonadio V. Malka, E. De Wispelaere, F. Amiranoff, F. Blasco, C. Stenz, Ph. Mounaix, G. Grillon, and E. Nibbering.
Stimulated raman backscattering instability in short pulse laser interaction with helium gas.
Phys. Plasmas, 3, 5:1682–1688, 1996.

[75] J. H. Marburger.
Self-focusing: Theory.
Prog. Quant. Electr., 4:35–110, 1975.

[76] F. DeMartini, C. H. Townes, T. K. Gustafson, and P. L. Kelley.
Self-steepening of light pulses.
Phys. Rev., 164:312–323, Dec 1967.

[77] S. C. Rae, K. Burnett, and J. Cooper.
Generation and propagation of high-order harmonics in a rapidly ionizing medium.
Phys. Rev. A, 50:3438–3446, Oct 1994.

[78] S. P. Le Blanc, R. Sauerbrey, S. C. Rae, and K. Burnett.
Spectral blue shifting of a femtosecond laser pulse propagating through a high-pressure gas.
J. Opt. Soc. Am. B, 10(10):1801–1809, Oct 1993.

[79] S. P. Le Blanc and R. Sauerbrey.
Spectral, temporal, and spatial characteristics of plasma-induced spectral blue shifting and its application to femtosecond pulse measurement.
J. Opt. Soc. Am. B, 13(1):72–88, Jan 1996.

[80] S. C. Rae and K. Burnett.

Detailed simulations of plasma-induced spectral blueshifting.
Phys. Rev. A, 46:1084–1090, 1992.

[81] T. Auguste, P. Monot, L. A. Lompre, G. Mainfray, and C. Manus.
Multiply charged ions produced in noble gases by a 1 ps laser pulse at lambda =1053 nm.
Journal of Physics B, 25:4181–4194, 1992.

[82] C.P. Hauri, W. Kornelis, F.W. Helbing, A. Heinrich, A. Couairon, A. Mysyrowicz, J. Biegert, and U. Keller.
Generation of intense, carrier-envelope phase-locked few-cycle laser pulses through filamentation.
Applied Physics B, 79:673–677, 2004.

[83] O. Shorokhov, A. Pukhov, and I. Kostyukov.
Self-compression of laser pulses in plasma.
Phys. Rev. Lett., 91:265002, 2003.

[84] M. Nisoli, S. De Silvestri, and O. Svelto.
Generation of high energy 10 fs pulses by a new pulse compression technique.
Appl. Phys. Lett., 68, 20:2793–2795, 1996.

[85] S. A. Skobelev, A. V. Kim, and O. Willi.
Generation of high-energy few-cycle laser pulses by using the ionization-induced self-compression effect.
Phys. Rev. Lett., 108:123904, 2012.

[86] G. Stibenz, N. Zhavoronkov, and G. Steinmeyer.
Self-compression of millijoule pulses to 7.8 fs duration in a white-light filament.
Optics Letters, 31,2:274–276, 2006.

[87] E. Schulz, T. Binhammer amd D. S. Steingrube, S. Rausch, M. Kovacev, and U Morgner.
Intense few-cycle laser pulses from self-compression in a self-guiding filament.
Applied Physics B, 95, 5:269–272, 2009.

[88] M. Mlejnek, E. M. Wright, and J. V. Moloney.
Dynamic spatial replenishment of femtosecond pulses propagating in air.
Optics Letters, 23, 5:382–384, 1998.

[89] S. Skupin, G. Stibenz, L. Bergé, F. Lederer, T. Sokollik, M. Schnürer, N. Zhavoronkov, and G. Steinmeyer.
Self-compression by femtosecond pulse filamentation: Experiments versus numerical simulations.
Phys. Rev. E, 74:056604, 2006.

[90] P.B. Corkum and F. Krausz.
Attosecond science.

Nature physics, 3:381–387, 2007.

[91] E. Goulielmakis, H. Lo, A. Wirth, R. Santra, and N. Rohringer.
Real-time observation of valence electron motion.
Nature, 466:739–743, 2010.

[92] S. Boutet, L. Lomb, G. J. Williams, T. R. M. Barends, A. Aquila, R. B. Doak, U. Weierstall, D.P. DePonte, J. Steinbrener, R. L. Shoeman, M. Messerschmidt, A. Barty, T. A. White, S. Kassemeyer, R. A. Kirian, M. M. Seibert, P. A. Montanez, C. Kenney, R. Herbst, P. Hart, J. Pines, G. Haller, S. M. Gruner, H. T. Philipp, M. W. Tate, M. Hromalik, L. J. Koerner, N. van Bakel, J. Morse, W. Ghonsalves, D. Arnlund, M. J. Bogan, C. Caleman, R. Fromme, C. Y. Hampton, M. S. Hunter, L. C. Johansson, G. Katona, C. Kupitz, M. Liang, A. V. Martin, K. Nass, L. Redecke, F. Stellato, N. Timneanu, D. Wang, N. A. Zatsepin, D. Schafer, J. Defever, R. Neutze, P. Fromme, J. C. H. Spencer, H. N. Chapman, and I. Schlichting.
High-resolution protein structure determination by serial femtosecond crystallography.
Science, 337, 6092:362–364, 2012.

[93] P. Emma, R. Akre, J. Arthur, R. Bionta, C. Bostedt, J. Bozek, A. Brachmann, P. Bucksbaum, R. Coffee, F.-J. Decker, Y. Ding, D. Dowell, S. Edstrom, A. Fisher, J. Frisch, S. Gilevich, J. Hastings, G. Hays, Ph. Hering, Z. Huang, R. Iverson, H. Loos, M. Messerschmidt, A. Miahnahri, S. Moeller, H.-D. Nuhn, G. Pile, D. Ratner, J. Rzepiela, D. Schultz, T. Smith, P. Stefan, H. Tompkins, J. Turner, J. Welch, W. White, J. Wu, G. Yock, and J. Galayda.
First lasing and operation of an angstrom-wavelength free-electron laser.
nature photonics, 4:641–647, 2010.

[94] M. Lewenstein, Ph. Balcou, M. Yu. Ivanov, Anne L'Huillier, and P. B. Corkum.
Theory of high-harmonic generation by low-frequency laser fields.
Phys. Rev. A, 49:2117–2132, Mar 1994.

[95] P. B. Corkum.
Plasma perspective on strong field multiphoton ionization.
Phys. Rev. Lett., 71:1994–1997, Sep 1993.

[96] P. Colosimo, G. Doumy, C. I. Blaga, J. Wheeler, C. Hauri, F. Catoire, J. Tate, R. Chirla, A. M. March, G. G. Paulus, H. G. Muller, P. Agostini, and L. F. DiMauro.
Scaling strong-field interactions towards the classical limit.
nature physics, 4:386–389, 2008.

[97] S. Gordienko, A. Pukhov, O. Shorokhov, and T. Baeva.
Relativistic doppler effect: Universal spectra and zeptosecond pulses.
Phys. Rev. Lett., 93(11):115002, Sep 2004.

[98] B. Dromey, M. Zepf, A. Gopahl, K. Lancester, M. S. Wei, K. Krushelnick, M. Tatakis,

N. Vakakis, S. Moustaizis, R. Kodama, M. Tampo, C. Stoeckl, R. Clarke, H. Habara, D. Neely, S. Karsch, and P. Norreys.
High harmonic generation in the relativistic limit.
nature physics, 2:456–459, 2006.

[99] B. Dromey, D. Adams, R. Hörlein, Y. Nomura, S. G. Rykovanov, D. C. Carroll, P. S. Foster, S. Kar, K. Markey, P. McKenna, D. Neely, M. Geissler, G. D. Tsakiris, and M. Zepf.
Diffraction-limited performance and focusing of high harmonics from relativistic plasmas.
nature physics, 5:146–152, 2009.

[100] R. Hörlein, S. Y. Nomura, J. Osterhoff, Z. Major, S. Karsch, F. Krausz, and G. D. Tsakiris.
High harmonics from solid surfaces as a source of ultra-bright xuv radiation for experiments.
Plasma Phys. Control. Fusion, 50:1–13, 2008.

[101] B. Dromey, S. Rykovanov, M. Yeung, R. Hörlein, D. Jung, D. C. Gautier, T. Dzelzainis, D. Kiefer, S. Palaniyppan, R. Shah, J. Schreiber, H. Ruhl, J. C. Fernandez, C. L. S. Lewis, M. Zepf, and B. M. Hegelich.
Coherent synchrotron emission from electron nanobunches formed in relativistic laser plasma interactions.
nature physics, 2439:10.1038, 2012.

[102] F. Quere, C. Thaury, P. Monot, S. Dobosz, Ph. Martin, J.-P. Geindre, and P. Audebert.
Coherent wake emission of high-order harmonics from overdense plasmas.
Physical Review Letters, 96,125004:1–4, 2006.

[103] F. Quéré, C. Thaury, J-P. Geindre, G. Bonnaud, P. Monot, and Ph. Martin.
Phase properties of laser high-order harmonics generated on plasma mirrors.
Phys. Rev. Lett., 100:095004, Mar 2008.

[104] Y. Nomura, R. Hörlein, P. Tzallas, B. Dromey, S. Rykovanov, Zs. Major, J. Osterhoff, S. Karsch, L. Veisz, M. Zepf, D. Charalambidis, F. Krausz, and G. D. Tsakiris.
Attosecond phase locking of harmonics emitted from laser-produced plasmas.
nature physics, 5:124–128, 2009.

[105] G. D. Tsakiris, Eidmann, J. Meyer ter Vehn, and F. Krausz.
Route to intense single attosecond pulses.
New Journal of Physics, 9:1–20, 2006.

[106] R. Lichters, J. Meyer ter Vehn, and A. Pukhov.
Short-pulse laser harmonics from oscillating plasma surfaces driven at relativistic intensity.
Phys. Plasmas, 3:3425–3437, 1996.

[107] B. Dromey, S. Kar, C. Bellei, D. C. Carroll, R. J. Clarke, J. S. Green, S. Kneip, K. Markey, S. R. Nagel, P. T. Simpson, L. Willingale, P. McKenna, D. Neely, Z. Najmudin, K. Krushelnick, P. A. Norreys, and M. Zepf.
Bright multi-kev harmonic generation from relativistically oscillating plasma surfaces.
Phys. Rev. Lett., 99:085001, Aug 2007.

[108] T. Baeva, S. Gordienko, and A. Pukhov.
Theory of high-order harmonic generation in relativistic laser interaction with overdense plasma.
Phys. Rev. E, 74:046404, Oct 2006.

[109] D. an der Brügge and A. Pukhov.
Enhanced relativistic harmonics by electron nanobunching.
Phys. Plasmas, 17,3:033110, 2010.

[110] S.C. Wilks, W.L. Kruer, and W.B. Mori.
Odd harmonic generation of ultra-intense laser pulses reflected from an overdense plasma.
IEEE Transactions on Plasma Science, 21,1:120–124, 1993.

[111] T. Baeva, S. Gordienko, and A. Pukhov.
Relativistic plasma control for single attosecond x-ray burst generation.
Phys. Rev. E, 74:065401, Dec 2006.

[112] D. an der Brügge and A. Pukhov.
Propagation of relativistic surface harmonics radiation in free space.
Physics of Plasmas, 14:093104, 2007.

[113] J. Bierbach, C. Rödel, M. Yeung, B. Dromey, T. Hahn, A. Galestian Pour, S. Fuchs, A. E. Paz, S. Herzer, S Kuschel, O. Jäckel, M. C. Kaluza, G. Pretzler, M. Zepf, and G. G. Paulus.
Generation of 10 μW relativistic surface high-harmonic radiation at a repetition rate of 10 hz.
New Journal of Physics, 14:065005, 2012.

[114] S. C. Wilks, W. L. Kruer, M. Tabak, and A. B. Langdon.
Absorption of ultra-intense laser pulses.
Phys. Rev. Lett., 69:1383–1386, Aug 1992.

[115] U. Teubner, K. Eidmann, U. Wagner, U. Andiel, F. Pisani, G. D. Tsakiris, K. Witte, J. Meyer-ter Vehn, T. Schlegel, and E. Förster.
Harmonic emission from the rear side of thin overdense foils irradiated with intense ultrashort laser pulses.
Phys. Rev. Lett., 92:185001, May 2004.

[116] K. Eidmann, T. Kawachi, A. Marcinkevicius, R. Bartlome, G. D. Tsakiris, K. Witte, and

U. Teubner.
Fundamental and harmonic emission from the rear side of a thin overdense foil irradiated by an intense ultrashort laser pulse.
Physical Review E, 72(3):036413, 2005.

[117] M. Yeung, M. Zepf, M. Geissler, and B. Dromey.
Angularly separated harmonic generation from intense laser interaction with blazed diffraction gratings.
Optics Letters, 36,12:2333–2335, 2011.

[118] M. Raynauda, J. Kupersztych, C. Riconda, J. C. Adam, and A. Heron.
Strongly enhanced laser absorption and electron acceleration via resonant excitation of surface plasma waves.
Physics of Plasmas, 14:092702–1–092702–9, 2007.

[119] L. Cao, Y. Gu, Z. Zhao, L. Cao, and W. Huang.
Enhanced absorption of intense short-pulse laser light by subwavelength nanolayered target.
Phys. Plasmas, 17:043103, 2010.

[120] A. A. Andreev, N. Kumar, K. Platonov, and A. Pukhov.
Efficient generation of fast ions from surface modulated nanostructure targets irradiated by high intensity short-pulse lasers.
Phys. Plasmas, 18:103103, 2011.

[121] W.-M. Wang, Z.-M. Sheng, and J. Zhang.
A model for the efficient coupling between intense lasers and subwavelength grating targets.
Physics of Plasmas, 15:030702, 2008.

[122] P. Albers, E. Stark, and G. Huber.
Continuous-wave laser operation and quantum efficiency of titanium-doped sapphire.
J. Opt. Soc. Am. B, 3,1:134, 1986.

[123] A. Jullien, O. Albert, F. Burgy, G. Hamoniaux, L. P. Rousseau, J.P. Chambaret, F. Auge-Rochereau, G. Cheriaux, J. Etchepare, N. Minkovski, and S. M. Saltiel.
10(-10) temporal contrast for femtosecond ultraintense lasers by cross-polarized wave generation.
OPTICS LETTERS, 30(8):920–922, APR 15 2005.

[124] A. Jullien, C. G. Durfee, A. Trisorio, L. Canova, J-P. Rousseau, B. Mercier, L. Antonucci, G. Cheriaux, O. Albert, and R. Lopez-Martens.
Nonlinear spectral cleaning of few-cycle pulses via cross-polarized wave (xpw) generation.
APPLIED PHYSICS B-LASERS AND OPTICS, 96:293–299, 2009.

[125] H. C. Kapteyn, M. M. Murnane, A. Szoke, and R. W. Falcone.
Prepulse energy suppression for high-energy ultrashort pulses using self-induced plasma shuttering.
OPTICS LETTERS, 16 (7):490–492, 1991.

[126] G. Doumy, F. Quéré, O. Gobert, M. Perdrix, Ph. Martin, P. Audebert, J. C. Gauthier, J.-P. Geindre, and T. Wittmann.
Complete characterization of a plasma mirror for the production of high-contrast ultraintense laser pulses.
Phys. Rev. E, 69:026402, Feb 2004.

[127] F. Quere, C. Thaury, H. George, J. P. Geindre, E. Lefebvre, G. Bonnaud, P. Monot, and P. Martin.
High-order harmonic generation using plasma mirrors.
Plasma Phys. Control. Fusion, 50:1–7, 2008.

[128] J. Collier, C. Hernandez-Gomez, R. Allott, C. Danson, and A. Hall.
A single-shot third-order autocorrelator for pulse contrast and pulse shape measurements.
Laser and Particle Beams, 19:231–235, 2001.

[129] J.-C. Diels and W. Rudolph.
Ultrashort Laser Pulse Phenomena.
Academic Press, 2006.

[130] D. M. Gold.
Direct measurement of prepulse suppression by use of plasma shutter.
Optics Letters, 19:2006–2008, 1994.

[131] C. Ziener, P. S. Foster, E. J. Divall, C. J. Hooker, M. H. R. Hutchinson, A. J. Langley, and D. Neely.
The dependence of the specular reflectivity of plasma mirrors on laser intensity, pulse duration and angle of incidence.
Journal of Applied Physics, 93:768–770, 2003.

[132] B. Dromey, S. Kar, M. Zepf, and P. Foster.
The plasma mirror - a subpicosecond optical switch for ultrahigh power lasers.
REVIEW OF SCIENTIFIC INSTRUMENTS, 75,3:645–649, 2004.

[133] C. Rödel, M. Heyer, M. Behmke, M. Kübel, O. Jäckel, Ockel, W. Ziegler, D. Ehrt, M. Kaluza, and G. Paulus.
High repetition rate plasma mirror for temporal contrast enhancement of terawatt femtosecond laser pulses by three orders of magnitude.
Applied Physics B: Lasers and Optics, 103:295–302, 2010.
10.1007/s00340-010-4329-7.

[134] C. Thaury, F. Quere, H. George, J. P. Geindre, P. Monot, and P. Martin.

High-order harmonic generation from plasma mirrors.
The European Physical Journal - Special Topics, 175:43–48, 2009.

[135] C. Thaury, F. Quere, J.-P. Geindre, A. Levy, T. Cecotti, P. Monot, M. Bougeard, P. D'Oliveira F. Reau, P. Audebert, R. Marjoribanks, and P. Martin.
Plasma mirrors for ultrahigh intensity optics.
nature physics, 3:424–429, 2007.

[136] B. C. Stuart, M. D. Feit, S. Herman, A. M. Rubenchik, B. W. Shore, and M. D. Perry.
Nanosecond-to-femtosecond laser-induced breakdown in dielectrics.
Phys. Rev. B, 53:1749–1761, Jan 1996.

[137] C. Schaffer, A. Brodeur, and E. Mazur.
Laser-induced breakdown and damage in bulk transparent materials induced by tightly focused femtosecond laser pulses.
MEASUREMENT SCIENCE AND TECHNOLOGY, 12:1784–1794, 2001.

[138] S. Backus, H. C. Kapteyn, M. M. Murnane, D. M. Gold, H. Nathel, and W-White.
Prepulse suppression for high-energy ultrashort pulses using self-induced plasma shuttering from a fluid target.
Optics Letters, 18:134–136, 1993.

[139] D. Panasenko, A. J. Shu, A. Gonsalves, K. Nakamura, N. H. Matlis, C. Toth, and W. P. Leemans.
Demonstration of a plasma mirror based on a laminar flow water film.
Journal of Applied Physics, 108:044913–1, 2010.

[140] A. Levy, T. Ceccotti, P. D Oliveira, F. Reau, M. Perdrix, F. Quere, P. Monot, M. Bougeard, H. Lagadec, and Philippe Martin.
Double plasma mirror for ultrahigh temporal contrast ultraintense laser pulses.
Optics Letters, 32:310–312, 2007.

[141] T. Wittmann, J. P. Geindre, P. Audebert, R. S. Marjoribanks, J. P. Rousseau, F. Burgy, D. Douillet, T. Lefrou, K. Ta Phuoc, and J. P. Chambaret.
Towards ultrahigh contrast ultraintense laser pulses complete characterization of a double plasma mirror pulse cleaner.
Review of Scientific Instruments, 77:083109, 2006.

[142] I. J. Kim, I. Choi, S. Lee, K. Janulewicz, J. Sung, T. Yu, H. Kim, H. Yun, T. Jeong, and J. Lee.
Spatio-temporal characterization of double plasma mirror for ultrahigh contrast and stable laser pulse.
Applied Physics B: Lasers and Optics, 104:81–86, 2011.

[143] D. Neely, P. Foster, A. Robinson, F. Lindau, O. Lundh, A. Persson, C.-G. Wahlström, and P. McKenna.
Enhanced proton beams from ultrathin targets driven by high contrast laser pulses.

Applied Physics Letters, 89:021502, 2006.

[144] R. Hörlein, B. Dromey, D. Adams, Y. Nomura, S. Kar, K. Markey, P. Foster, D. Neely, F. Krausz, G. D. Tsakiris, and M. Zepf.
High contrast plasma mirror: spatial filtering and second harmonic generation at 10 19 w cm-2.
New Journal of Physics, 10(8):083002, 2008.

[145] S. Spickermann.
Entwicklung eines Multischuss-Target und Detektorensystems für laserbeschleunigte Protonen.
Master's thesis, Heinrich-Heine-Universität Düsseldorf, 2011.

[146] K. Eidmann, J. Meyer ter Vehn, and T. Schlegel.
Hydrodynamic simulation of subpicosecond laser interaction with solid-density matter.
Physical Review E, 62,1:1202–1214, 2000.

[147] R. Ramis, R. Schmalz, and J. Meyer ter Vehn.
Multi - a computer code for one-dimensional multigroup radiation hydrodynamics.
Computer Physics Communications, 49:475–505, 1988.

[148] J. Osterholz, F. Brandl, T. Fischer, D. Hemmers, M. Cerchez, G. Pretzler, O. Willi, and S. J. Rose.
Production of dense plasmas with sub-10-fs laser pulses.
Phys. Rev. Lett., 96:085002, Feb 2006.

[149] J. Osterholz, F. Brandl, M. Cerchez, T. Fischer, D. Hemmers, B. Hidding, A. Pipahl, G. Pretzler, S. J. Rose, and O. Willi.
Extreme ultraviolet emission from dense plasmas generated with sub-10-fs laser pulses.
Physics of Plasmas, 15:103301, 2008.

[150] M. Cerchez, R. Jung, J. Osterholz, T. Toncian, O. Willi, P. Mulser, and H. Ruhl.
Absorption of ultrashort laser pulses in strongly overdense targets.
Phys. Rev. Lett., 100:245001, Jun 2008.

[151] C. Iaconis and I. A. Walmsley.
Spectral phase interferometry for direct electric-field reconstruction of ultrashort optical pulses.
Optics Letters, 23, 10:792–794, 1998.

[152] C. Iaconis and I. A. Walmsley.
Self-referencing spectral interferometry for measuring ultrashort optical pulses.
IEEE Journal of Quantum Electronics, 35, 24:501–509, 1999.

[153] R. Trebino and D. J. Kane.
Using phase retrieval to measure the intensity and phase of ultrashort pulses:

frequency-resolved optical gating.
JOSA A, 10,5:1101–1111, 1993.

[154] O. Willi R. Jung, J. Osterholz and S. Kar C. A. Cecchetti M. Borghesi S. Kar C. A. Cecchetti M. Galimberti, L. A. Gizzi M. Borghesi.
Optimization and characterization of supersonic gas jet target for laser-plasma interaction studies.
Technical report, Central Laser Facility Annual Report 2004/2005, 2005.

[155] R. Jung.
Laser-plasma interaction with ultra-short laser pulses.
PhD thesis, Heinrich-Heine-Universität Düsseldorf, 2007.

[156] V. Malka, C. Coulaud, J. P. Geindre, V. Lopez, Z. Najmudin, D. Neely, and F. Amiranoff.
Characterization of neutral density profile in a wide range of pressure of cylindrical pulsed gas jets.
REVIEW OF SCIENTIFIC INSTRUMENTS, 71,6:2329–2333, 2000.

[157] M. Hipp, J. Woisetschläger, P. Reiterer, and T. Neger.
Digital evaluation of interferograms.
Elsevier, 36:53–66, 2004.

[158] A. Pipahl.
Simultane Untersuchung von ultrakurzen Laserpulsen und laserbeschleunigten Elektronen.
PhD thesis, Heinrich-Heine-Univerisität Düsseldorf, 2010.

[159] P. Kirkpatrick and A. V. Baez.
Formation of optical images by x-rays.
Journal of the Optical Society of America, 38,9:766–773, 1948.

[160] T. Kita, T. Harada, N. Nakano, and H. Kuroda.
Mechanically ruled aberration-corrected concave gratings for a flat-field grazing-incidence spectrograph.
Applied Optics, 22,4:512–513, 1983.

[161] T. Fischer.
SPIDER als Instrument zur Untersuchung der Laser-Plasma-Wechselwirkung an Gasjet-Targets im sub-10-fs Regime.
PhD thesis, Heinrich-Heine-Univeristät Düsseldorf, 2007.

[162] R. Fedosejevs, X. F. Wang, and G. D. Tsakiris.
Onset of relativistic self-focusing in high density gas jet targets.
Phys. Rev. E, 56:4615–4639, Oct 1997.

[163] T. Auguste, O. Gobert, C. Fourcade Dutin, A. Dubrouil, E. Mevel, S. Petit, E. Constant, and D. Descamps.
Application of optical-field-ionization-induced spectral broadening in helium gas to

the postcompression of high-energy femtosecond laser pulses.
Journal Opt. Soc. Am. B, 29:1277–1286, 2012.

[164] A. Baltuska, Th. Udem, M. Uiberacker, M. Hentschel, E. Goulielmakis, Ch. Gohle, R. Holzwarth, V. S. Yakovlev, A. Scrinzi, T. W. Hänsch, and F. Krausz.
Attosecond control of electronic processes by intense light fields.
Nature, 421:611–615, 2003.

[165] V. V. Strelkov, E. Mevel, and E. Constant.
Generation of isolated attosecond pulses by spatial shaping of a femtosecond laser beam.
New Journal of Physics, 10:083040, 2008.

[166] F. Tavella, A. Marcinkevicius, and F. Krausz.
90 mj parametric chirped pulse amplification of 10 fs pulses.
Opt. Express, 14:12822–12827, 2006.

[167] P. Wnuk, Y. Stepanenko, and C. Radzewicz.
Multi-terawatt chirped pulse optical parametric amplifier with a time-shear power amplification stage.
Opt. Express, 17, 17:15264–15273, 2009.

[168] M. Mlejnek, E. M. Wright, and J. V. Moloney.
Femtosecond pulse propagation in argon: A pressure dependence study.
Phys. Rev. E, 58:4903–4910, Oct 1998.

[169] K. Yee.
Numerical solution of initial boundary value problems involving maxwell's equations in isotropic media.
IEEE Transactions on Antennas and Propagation, 14,3:302–307, 1966.

[170] A.F. Oskooi, D. Roundy, M. Ibanescu, P. Bermel, J.D. Joannopoulos, and S. G. Johnson.
Meep: A flexible free-software package for electromagnetic simulations by the fdtd method.
Computer Physics Communications, 181(3):687 – 702, 2010.

[171] C. S. Brady and T. D. Arber.
An ion acceleration mechanism in laser illuminated targets with internal electron density structure.
PLASMA PHYSICS AND CONTROLLED FUSION, 53:015001, 2011.

[172] H. Ruhl.
Introduction to Computational Methods in Many Particle Body Physics.
Rinton, 2006.

[173] *Provisional Design and Contributions from the First Workshop- International Center for Zettawatt-Exawatt Science and Technology IZEST http://www.izest.polytechnique.edu*, 2012.

List of Figures

List of Tables

A Ionisation thresholds

Ionisation thresholds predicted by the BSI theory [81, 155]:

Ionisation process	Ionisation potential [eV]	Threshold intensity [W/cm^2]
$He \rightarrow He^{+}$	24.6	1.5×10^{15}
$He^{+} \rightarrow He^{2+}$	54.4	8.5×10^{15}
$Ne \rightarrow Ne^{+}$	21.6	8.7×10^{14}
$Ne^{+} \rightarrow Ne^{2+}$	41.0	2.8×10^{15}
$Ne^{2+} \rightarrow Ne^{3+}$	63.5	7.2×10^{15}
$Ne^{3+} \rightarrow Ne^{4+}$	97.1	2.2×10^{16}
$Ne^{4+} \rightarrow Ne^{5+}$	126.2	4.1×10^{16}
$Ne^{5+} \rightarrow Ne^{6+}$	157.9	6.9×10^{16}
$Ar \rightarrow Ar^{+}$	15.8	2.5×10^{14}
$Ar^{+} \rightarrow Ar^{2+}$	27.6	5.8×10^{14}
$Ar^{2}+ \rightarrow Ar^{3+}$	40.7	1.2×10^{15}
$Ar^{3+} \rightarrow Ar^{4+}$	59.8	3.2×10^{15}
$Ar^{4+} \rightarrow Ar^{5+}$	75.0	5.1×10^{15}
$Ar^{5+} \rightarrow Ar^{6+}$	91.0	7.6×10^{15}
$Ar^{6+} \rightarrow Ar^{7+}$	124.3	1.9×10^{16}
$Ar^{7+} \rightarrow Ar^{8+}$	143.5	2.6×10^{16}

Table A.1

List of publications

Published and submitted papers:

- M. Cerchez, A. L. Giesecke, C. Peth, M. Toncian, B. Albertazzi, J. Fuchs, O. Willi, and T. Toncian. Generation of laser-driven higher harmonics from grating targets. *Physical Review Letters*, 110, 065003, Feb. 2013.
- H. Ahmed, M. E. Dieckmann, L. Romagnani, D. Doria, G. Sarri, M. Cerchez, E. Ianni, I. Kourakis, A. L. Giesecke, M. Notley, R. Prasad, K. Quinn, O. Willi, M. Borghesi. Time-resolved characterization of the formation of a collisionless shock: accepted for publication in *Physical Review Letters*, 2013.

Acknowledgement

First of all, I would like to thank my supervisor Prof. Dr. Oswald Willi for offering me the opportunity to work in this interesting field of research and write my PhD thesis at this high power laser facility. Secondly, thanks to Prof. Dr. Alexander Pukhov for being the second referee.

I would like to acknowledge the never-ending support of Dr. Mirela Cerchez in the lab and in general.

Thanks a lot to my colleagues who shared time with me in the bunker and/or laser room and contributed to the results of the experiments: Dr. Christian Peth, Dr. Toma Toncian, Marco Swantusch, Jürgen Böker, Tobias Thiele, Sven Spickermann, Dr. Ariane Pipahl and also my master student Kunaree Wongrach.

Many thanks to the team operating the ARCTURUS laser: Monika Toncian, Dr. Toma Toncian and Farzan Hamzehei.

I'm thankful to Christian Stelzmann for the support during the experiments in the U1 lab.

My special thanks go to Dr. Götz Lehmann for trouble-shooting of PIC simulations and the generous amount of computational time on the Jülich Supercomputer Cluster. Additionally, many thanks to Prof. Dr. Arkady Kim and Evgeny Efimenko for the cooperation for the FDTD simulation.

Furthermore, I would like to address many thanks to the secretary team and especially Katherina Lanzer and Claudia Dingle.

I also want to thank the team of the mechanical and electrical workshop for their solutions for motors, mirror holders and vacuum chambers.

Thanks to the Research Training Group GRK 1203 for the funding.

Last but not least, I would like to thank my family, especially my husband Marius Giesecke and Sieglinde, Heinz and Rosemarie Lindemann for their constant support, understanding and encouragement over the years.

Eidesstattliche Versicherung

Ich versichere an Eides Statt, dass die Dissertation von mir selbstständig und ohne unzulässige fremde Hilfe unter Beachtung der "Grundsätze zur Sicherung guter wissenschaftlicher Praxis an der Heinrich-Heine-Universität Düsseldorf" erstellt worden ist.

Die vorliegende Dissertation wurde in der vorgelegten oder in ähnlicher Form noch bei keiner anderen Institution eingereicht. Ich habe bisher keine erfolglosen Promotionsversuche unternommen.

Düsseldorf, Januar 2013 Anna Lena Giesecke